Université catholique de Louvain
Institute of Condensed Matter and Nanosciences

Inorganic Cathode Materials for Rechargeable Batteries from Lithium to Sodium Storage

Xuelian Liu
Supervisor: Prof. Alexandru Vlad

Thesis submitted in fulfilment of
the degree of Doctor in Sciences

October, 2021

Université catholique de Louvain
Institute of Condensed Matter and Nanosciences

Inorganic Cathode Materials for Rechargeable Batteries from Lithium to Sodium Storage

Xuelian Liu

Jury members:

Prof. Alexandru Vlad (UCLouvain, Belgium), supervisor
Prof. Yann Garcia (UCLouvain, Belgium), president
Prof. Sophie Hermans (UCLouvain, Belgium)
Prof. Jean-François Gohy (UCLouvain, Belgium)
Prof. Bao-Lian Su (Université de Namur, Belgium)
Prof. Jun Chen (Nankai University, China)
Prof. Jilei Liu (Hunan University, China)

Thesis submitted in fulfilment of
the degree of Doctor in Sciences

October, 2021

Abstract of the Thesis

Lithium-ion battery (LIB) as one rechargeable and powerful energy storage system is used to power many things from mobile phones to electric vehicles. The harvested green but intermittent solar and wind energy can also be stored in LIBs. While LIBs dominate the market, battery research on post-Li chemistries such as Na(K)-ion and Mg(Ca)-ion systems is booming, for it is expected to reduce the tension of scarcity and uneven distribution of Li on earth and also explore new possibilities. Sodium-ion batteries (SIBs) as immediate and low-cost alternatives to LIBs have caught much researchers' attention. However, reversible and efficient insertion of Na ions in conventional host electrode materials can face difficulties due to its larger radius than that of Li ion.

In this thesis, the widely investigated vanadium oxides were firstly selected to systematically study the impacts of phase structures, carbon matrices and morphologies on electrochemical properties of cathode materials for Li and Na storage. As a result, the accommodation of Na ions in those materials was found to be sluggish in comparison to that of Li ions.

Polyanionic compounds are considered to have open structure favourable to Na storage. Inspired by the knowledge on $NaFePO_4$, Na_2FePO_4F and $NaFeF_3$ chemistries, as well as the recently reported $Na_{0.6}Fe_{1.2}PO_4$ we developed a series of new cathode materials, $Na_{0.6+x}Fe_{1.2}PO_4F_x$ (with analysed values of x = 0, 0.2, 0.4, 0.6, 0.8 and 1). The $Na_{1.2}Fe_{1.2}PO_4F_{0.6}$ (x=0.6) composition was found to display the best performance with energy density of nearly 400 Wh kg^{-1} attained at the material level, although others were also found electrochemically active. Then, the $Na_{1.2}Fe_{1.2}PO_4F_{0.6}$ is considered as the main investigation target. We managed to synthesize amorphous, crystalline metastable and stable

materials with the x=0.6 composition, motivating us for extended analyses and comparison. The metastable $Na_{1.2}Fe_{1.2}PO_4F_{0.6}$ material was found to show great potential as cathode material candidate for SIBs.

In addition, further investigation has also been conducted for the iron-rich $Na_{0.6}Fe_{1.2}PO_4$ (x=0) phase as it has been surprisingly found to show a gradual increase in capacity along with a pair of 3.8 V (vs. Na^+/Na) redox plateaus appearing in potential profiles and gradually becoming noticeable upon charge-discharge cycling. The activated electrodes show excellent long-term cycling performance and rate capability and more than 350 Wh kg^{-1} energy density can be attained at the material level. Through in-depth analyses, new insights in this cathode material are offered. Overall, the space of Fe-PO_4-F low-cost, sustainable and high-performance cathode materials has been unblocked and remains for further exploration.

Preface

Energy, how fantastic it is, not only makes you feel alive and dynamic, but also the world beautiful and wonderful. An even better world can be built if it is green and clean. Utilization of renewable energy, collected from natural resources such as wind and solar, plays a significant role in realizing that. Meanwhile, energy storage systems should also be developed to store the renewable but intermittent energy, so that electricity can be supplied to communities continuously.

I started to work on electrode materials for batteries seven years ago. During my master study for three years, the main subject was silicon- and silica-based anode materials for Li-ion batteries. Then, I had the opportunity to study and work in Prof. Alexandru Vlad's NRJ group for PhD and continue acquiring knowledge in this field and to do research on cathode materials.

During the longer than four years of work, I can always receive help and support whenever need it. I would like to express my gratitude from the bottom of my heart.

First and foremost, I am deeply grateful to my supervisor, Prof. Alexandru Vlad, for his invaluable advice, unwavering support, and patience during my PhD study. All those discussions and brainstorms with him, his guidance and insightful comments have been motivating me to solve puzzles and make progress. I really appreciate the opportunity to work in his lab where broad research topics in battery field, talented researchers and students are involved.

I would like to extend my sincere thanks to my supervisory committee and jury members for taking the time to advice, guide and participate. I would also like to express the gratitude to co-authors. This work could not have been completed without their assistance and contribution.

I would like to say big thank you for all my colleagues for their understanding and help throughout my study and work. The excellent research team can be found on our NRJ Group website.

I would like to thank my friends and my family who have been wonderfully supportive. Especially, to my parents for their love and encouragement. Also, to my husband, as soulmate and teammate in life and at work.

Finally, I would like to offer my special thanks to my son, my angel, Bowen whose coming during this period is a gift and a challenge. His smiling, crying, happiness and curiosity make me feel the world full of wonders and energy.

Author Contributions

The author and her supervisor Prof. Alexandru Vlad designed this work. The author executed most of the experimental work, including the synthesis, characterization and electrochemical tests and wrote the thesis.

The contributions from colleagues and in collaboration are as follows:

Dr. Sébastien Depaifve synthesised all VO_x@rGO samples and gathered SEM and TEM images for the samples. Prof. Sophie Hermans also supervised the research work of Chapter 2.

Jiande Wang, Mengyuan Du et al. helped with experiments and studies.

Dr. Koen Robeyns, Prof. Yaroslav Filinchuk, Dr. Cristian Morari and Dr. Gheorghe Borodi contributed with XRD indexing and structure solution. Dr. Varun Kumar and Prof. Yann Garcia worked on Mössbauer spectroscopy analysis.

TABLE OF CONTENTS

Abstract of the Thesis I

Preface III

Author Contributions V

Glossary IX

Acronyms XI

Chapter 1 – Introduction 1

1.1 Na-ion versus Li-ion batteries **2**
1.1.1 Basics of Li-ion batteries 2
1.1.2 Cathode materials for Li-ion batteries 4
1.1.3 Development of Na-ion batteries 6
1.1.4 Cathode materials for Na-ion batteries 8

1.2 From Li-ion to Na-ion batteries: challenges and perspectives **13**

1.3 Design and engineering for inorganic cathode materials **18**
1.3.1 Transition metals used in cathode materials 19
1.3.2 Polymorphism in cathode materials 21
1.3.3 Metastability in cathode materials 24
1.3.4 Off-Stoichiometry in cathode materials 31
1.3.5 Rich chemistries in VO_x as cathode materials 33
1.3.6 Fluorine substitution in polyanionic cathode materials 36

1.4 Scope of this thesis **38**

CHAPTER 2 – Versatile Synthesis of Vanadium (III, IV, V) Oxides@rGO Nanocomposites and Evaluation of Their Li and Na Storage Performances 41

Abstract **41**

2.1 Introduction **43**

2.2 Results and discussion **48**
2.2.1 Synthesis methods 48
2.2.2 Characterizations 51
2.2.3 Electrochemical properties 58
2.2.4 Further discussion 73

2.3 Conclusions and significance of this work **76**

2.4 Experimental section **78**
2.4.1 Impregnation synthesis of V_2O_5@rGO 78
2.4.2 Hydrothermal synthesis of VO_2(B)@rGO 78
2.4.3 Hydrothermal synthesis of VO_2(AM)@rGO and V_2O_3@rGO 79
2.4.4 Materials characterizations 79
2.4.5 Electrochemical cell assembly and measurements 80
2.4.6 Ex-situ XRD measurement 81

CHAPTER 3 – Exploring the Chemical Space of Metastable Fe-PO_4-F Cathode Materials for High Performance Sodium Storage 83

Abstract **83**

3.1 Introduction **84**

3.2 Results and discussion **87**
3.2.1 Synthesis strategy of the metastable materials in the $Na_{0.6+x}Fe_{1.2}PO_4F_x$ chemical space 87
3.2.2 The chemical space of $Na_{0.6+x}Fe_{1.2}PO_4F_x$ compositions and materials 95
3.2.3 Comparative analysis of $Na_{1.2}Fe_{1.2}PO_4F_{0.6}$_S, _M and _AM 101
3.2.4 Comparative analysis of charge storage performances of $Na_{1.2}Fe_{1.2}PO_4F_{0.6}$_M, _S, S/C and _AM materials 111
3.2.5 Tracking the reversible electrochemistry of $Na_{1.2}Fe_{1.2}PO_4F_{0.6}$_M 118

3.3 Outlook and significance of this work 122

3.4 Experimental section 124
3.4.1 Sample preparation 124
3.4.2 Physicochemical characterizations 124
3.4.3 Electrochemical cell assembly and measurements 127

CHAPTER 4 – Unlocking the Electrochemistry and Activation Mechanism in Iron-rich $Na_{0.6}Fe_{1.2}PO_4$ Phase 129

Abstract 129

4.1 Introduction 130

4.2 Results and discussion 133
4.2.1 Characterizations 133
4.2.2 Electrochemical properties 136

4.3 Conclusions 145

4.4 Experimental section 146
4.4.1 Sample preparation 146
4.4.2 Characterizations 146
4.4.3 Electrochemical cell assembly and measurements 147

CHAPTER 5 – Final Conclusion and Perspectives 149

Bibliography 155

Associated publications 171

Glossary

Battery - a device constructed by one or many electrochemical cells for powering electrical devices, in which chemical energy is converted into power.

Cell - one unit of a battery, commonly consisting of an anode, a cathode, an electrolyte, separator, and two current collectors, capable of either generating electrical energy from chemical reactions or using electrical energy to cause chemical reactions.

Anode - (negative electrode) - This electrode donates electrons to the external circuit during cell discharge (electrochemical oxidation reaction).

Cathode - (positive electrode) - This electrode accepts electrons during cell discharge (electrochemical reduction reaction).

Theoretical capacity - Calculated by Faraday's law:

$$Q_{theoretical} = (n*F) / (3.6*MW) \text{ mAh } g^{-1}$$

Where n is the number of charge carrier, F is the Faraday constant and MW is the molecular weight of the active material used in the electrode.

Specific capacity - The amount of charge stored, often expressed as mAh g-1 at material level.

Energy density - Energy per unit volume or weight of a material or a device, respectively, often expressed as Wh L^{-1} or Wh kg^{-1}. Energy is a product of the cell voltage and capacity per unit volume or weight.

C-rate - The rate at which a battery is discharged relative to its maximum capacity. An 1C rate means that the discharge current will discharge the entire battery in 1 hour. A C/10 rate means that the discharge current will discharge the entire battery in 10 hours.

Power rate capability - A cell with good rate capability is able to deliver a considerable amount of power with little voltage loss even at high current loads.

Coulombic efficiency - The ratio of the total charge capacity to the total discharge capacity over a full cycle. It describes the charge efficiency of electrons transferred in cells.

Acronyms

LIBs	Li-ion batteries
TMs	transition metals
3D	three-dimensional
SIBs	Na-ion batteries
NASICON	Na Super Ionic CONductor
PBAs	prussian blue analogues
VO_x	vanadium oxides
C_{th}	theoretical capacity
rGO	reduced graphene oxide
XRD	X-ray diffraction
PXRD	powder X-ray diffraction
SEM	scanning electron microscopy
TEM	transmission electron microscopy
TGA	thermogravimetric analysis
CE	coulombic efficiency
PVDF	polyvinylidene difluoride
PTFE	polytetrafluoroethylene
FT-IR	Fourier transform infrared spectroscopy
ICP	inductively coupled plasma
CCCV	constant current, constant voltage
DSC	differential scanning calorimetry
MS	mass spectrometry
BET	Brunauer-Emmett-Teller technique
GITT	galvanostatic intermittent titration technique
O_h	octahedral coordination
EC	ethylene carbonate

DEC	diethyl carbonate
FEC	fluoroethylene carbonate
PC	propylene carbonate

Chapter 1 – Introduction

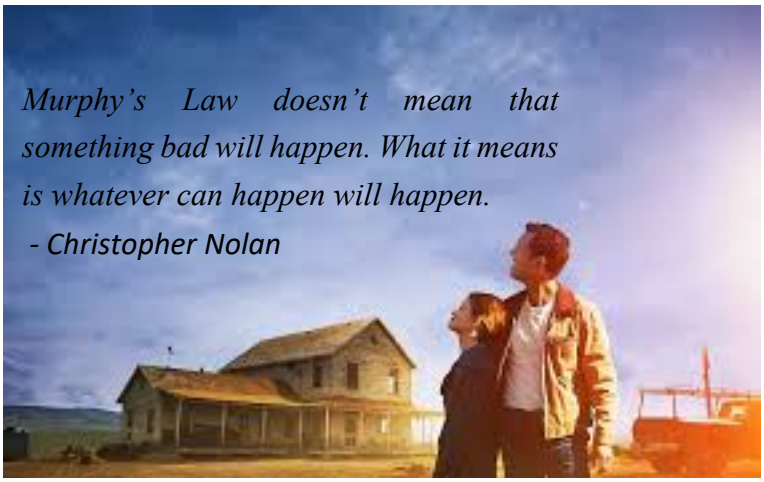

1.1 Na-ion versus Li-ion batteries

1.1.1 Basics of Li-ion batteries

Li-ion batteries (LIBs) are rechargeable batteries, constructed by basic electrochemical cells in various configurations. Typically, a basic Li-ion cell consists of a cathode (positive electrode) and an anode (negative electrode) which are isolated from each other by a separator immersed in an electrolyte. The electrolyte contains Li ions and the separator allows the exchange of Li ions between the two electrodes but not electrons. The basic operating principle of a typical Li-ion cell is depicted in **Figure 1.1**.[1] Basically, it involves reversible insertion / extraction of Li ions into / from electrode materials. Under an external electrical supply, electrons are released at the cathode and pass through the external circuit to the anode and simultaneously the Li ions move across the separator from cathode to anode in the electrolyte. This is how the external energy is electrochemically stored in the battery, namely charge process. During discharge, the process is reversed. Li ions move back to the cathode via electrolyte, while the electrons spontaneously flow to the cathode through the external load to do the work. The Li ions shuttle between the anode and cathode through the electrolyte upon charge and discharge cycling, so it is also known as "Li rocking-chair cell".[2]

In the electrochemical cell, redox reactions occur on the two electrodes when chemical energy is converted to electric energy, or vice versa. A typical example is $LiCoO_2$/graphite cell:

Positive electrode (charge): $LiCoO_2 \rightarrow Li_{1-x}CoO_2 + x\ Li^+ + x\ e^-$

Negative electrode (charge): $C_6 + x\ Li^+ + x\ e^- \rightarrow LiC_6$

Positive electrode (discharge): $Li_{1-x}CoO_2 + x\ Li^+ + x\ e^- \rightarrow LiCoO_2$

Negative electrode (discharge): $LiC_6 \rightarrow C_6 + x\ Li^+ + x\ e^-$

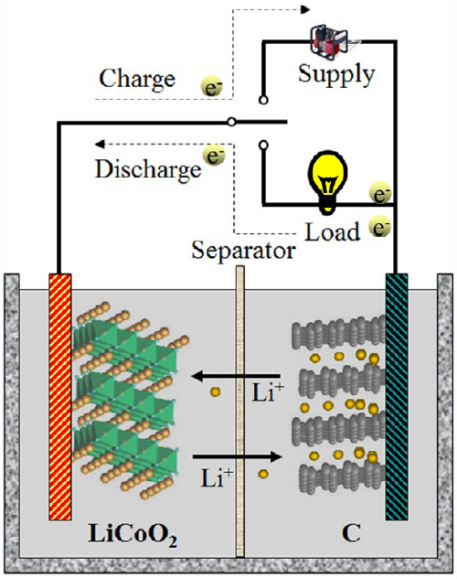

Figure 1.1 Basic components and operation principle of a Li-ion cell.[1]

The Li ions reversibly intercalate into the electrodes and combine with the electrons, balanced by the redox reactions on the two electrodes. The electrochemical reactions determine the stored chemical energy. The theoretical specific capacity (mAh g^{-1}) and cell voltage (V) can be estimated based on the reactions and charges transferred. Practical specific capacity is determined by the amount of charge reversibly stored per unit mass. Specific gravimetric energy (Wh kg^{-1}) measures the amount of energy that can be stored or released per unit mass, which can be calculated by multiplying the specific capacity with operating voltage. Other important parameters to evaluate the performance of LIBs include cyclability, power rate capability, volumetric energy, storage efficiency, safety and cost of fabrication. Active research is advancing in all aspects of batteries, from electrode, separator, electrolyte to safety, packaging, cell construction, battery management and recycling. The electrode materials generally determine some essential parameters mentioned above. For

instance, the rate of Li transfer between electrodes depends mainly on the dimensional stability of the host material during insertion and extraction of Li ions and on the kinetics of the Li ions and electron transport in the host. In addition, the cycle life strongly depends on the structural stability of electrode active materials during the charge-discharge process. Therefore, developing electrode materials and understanding their properties and characteristics are critical to achieve high-performance batteries. Classic electrode materials are listed in **Figure 1.2**. Efforts are making to develop high-performance cathode and anode materials, but the focus of this thesis is on the cathode materials.

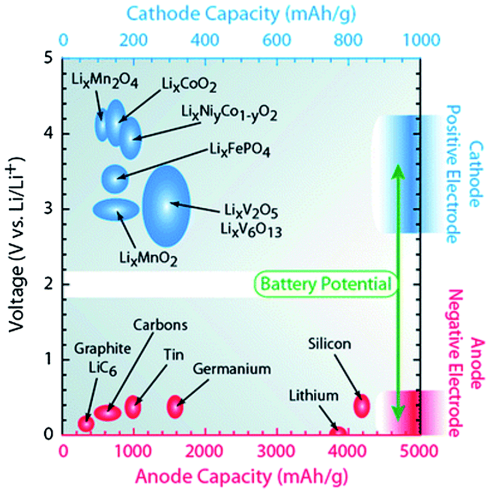

Figure 1.2 Diagram illustrating the specific capacity and electrochemical reduction potentials with respect to Li metal for a range of cathode and anode materials.[3]

1.1.2 Cathode materials for Li-ion batteries

Materials exhibiting high redox potentials are suitable for use as cathode materials and a great number of candidates have been employed as cathode materials for LIBs. The conventional cathode materials are often categorized into three types based on their crystalline structures: layered

oxides ($LiTMO_2$ (TM = Co, Ni, Mn)), spinel structure ($LiMn_2O_4$), and olivine structure ($LiFePO_4$) and a series of variants have also been explored.[4, 5] Typical examples are shown in **Figure 1.3**. The redox couples of those host are commonly transition-metal 3d energies and thus transition metals (TMs) play a fundamental role in this class of cathode materials.

The three categories of cathodes show their advantages and drawbacks in Li storage performance. Their capacity and electrochemical reduction potentials (vs. Li^+/Li) can be found in **Figure 1.2**. The materials with layered structure can deliver high capacities but undergo structural and/or chemical instabilities upon charge-discharge cycling.[6] The three-dimensional (3D) spinel $LiMn_2O_4$ with 3D Li ion diffusion shows good rate capability and structural stability. However, the practical capacities delivered are inferior because it faces Mn dissolution in the electrolyte.[7, 8] The olivine $LiFePO_4$ with 3D structure but only 1D Li ion diffusion can offer outstanding cycling stability and safety, whereas it suffers from limited capacity and poor electronic and Li ion conductivity.[6]

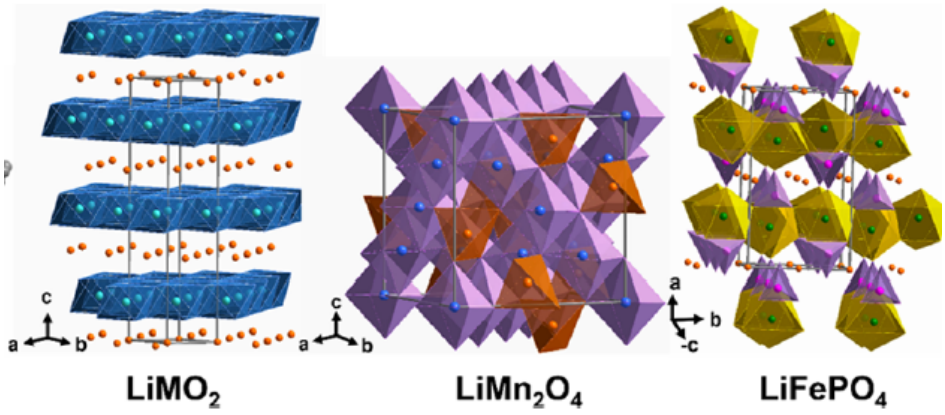

Figure 1.3 Crystal structures of layered $LiMO_2$ (M = Mn, Co, and Ni), spinel $LiMn_2O_4$, and olivine $LiFePO_4$.[6]

Many strategies have been proposed to improve the performance of these typical cathode materials, from partial cationic or anionic substitution and preparation of composite materials to morphology structural and surface modifications.[7, 9, 10] Some examples are provided as follows. Combination of Ni, Mn and Co ions in composition, layered $LiNi_{1/3}Mn_{1/3}Co_{1/3}O_2$ has been found to realize improved performance in terms of energy density and cycling stability, compared to $LiCoO_2$. A strategy to restrain the Mn dissolution and improve the electrochemical performance of $LiMn_2O_4$ is encapsulation of it in various salts such as Al_2O_3, ZnO and Li_3PO_4. Furthermore, carbon coating is another choice of surface modification. A thin conductive carbon coating at the surface of $LiFePO_4$ nanoparticles has been employed to enhance electronic conductivity of the cathode, so that good rate capability can be attained.

Varieties of derivatives of these conventional cathode materials have been widely investigated and evaluated to show improved electrochemical properties. A lot of research work has also been carried out on other cathode materials, such as various vanadium-based oxides, polyanionic compounds and so on. Researchers continue searching for novel and advanced cathode materials.

1.1.3 Development of Na-ion batteries

The components and working mechanisms of Na-ion batteries (SIBs) are basically similar to the LIBs, with the shuttle of Na ions between cathode and anode.[11] The early stage studies of Na storage are in the same period of beginning of LIB investigation. Recently, SIBs have been reconsidered for energy storage as cost-effective and sustainable alternative to LIB technology. The primary aims of using abundant and low-cost Na as a substitute for Li are to address issues related to the sources

and geographical distribution of Li and some other components in LIBs and to meet ever-growing demand for energy storage applications, especially for large-scale electrochemical energy storage applications, as shown in **Figure 1.4**.[12-15] SIBs are also attractive in view of environmental aspects since Na is eco-friendly and naturally recycled.[16]

Challenges exist in the transition from LIBs to SIBs. The Na ion (radius=1.06 Å) is larger than the Li ion (radius=0.76 Å), so the accommodation of Na ions in the electrode materials could be more difficult than that of Li ions.[17] In addition, Na is heavier than Li (23 g mol^{-1} compared with 6.9 g mol^{-1}) and is 0.3 V less electropositive, leading to lower energy density.[17] Researchers have been seeking for suitable electrode materials for Na ion insertion / extraction and many of them are either inspired or even identical to those already employed in LIBs. Nevertheless, their electrochemical properties are often inferior to those for Li accommodation and the choices of high-performance electrodes for Na storage are awaiting to be enriched.

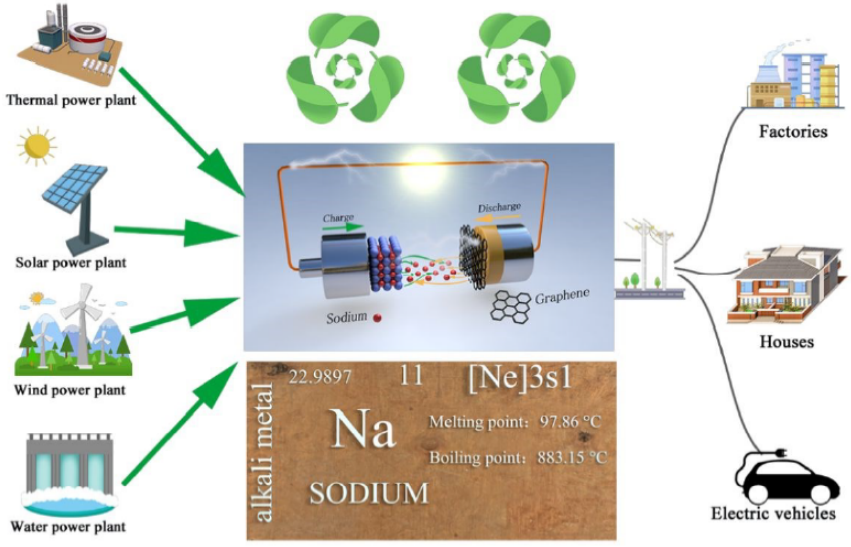

Figure 1.4 The mode of energy storage and energy output for SIBs.[15]

To further enhance the performance of SIBs, exploration and development of electrode materials with improved properties are essential. Particularly, cathode materials play a critical role in the improvement of energy density, lifespan and safety of SIBs.

1.1.4 Cathode materials for Na-ion batteries

The criteria in assessment of good cathode materials for SIBs are almost identical to those for LIBs.[18] The materials are capable of accommodating Na ions reversibly at a reasonably high potential. The volume change of the host structure during Na ion insertion / extraction should be as low as possible, which is important for long-term charge-discharge cycling. It is favourable for the materials to show good ionic conductivity, considering the large size and mass of the Na ion compared to the Li ion. Meanwhile, some other discrepancies in the intercalation chemistries between Na and Li should not be neglected and each cathode material could possess distinct properties.[19, 20] For instance, Na prefers 6-coordination to tetrahedral coordination in inorganic materials, due to the differences in the ion radius and the chemical properties, which limits the types of structures available for cathode materials for Na storage. In the case of alkali cobalt oxides, although Na ion has larger radius than Li ion, Na ion diffusion in layered $NaCoO_2$ is calculated to be easier as compared to Li ion diffusion in $LiCoO_2$.

Typical types of cathode materials for SIBs and their energy density values are listed in **Figure 1.5**. Layered structure Na transition metal oxides (NaTMOs), such as $NaCoO_2$, are one main type of cathode materials for reversible insertion of Na ions.[21] Those Na-based layered oxides can be mainly classified as O3-type and P2-type, in which O and P represent the Na ion occupy the octahedron sites and the centre of prism sites,

respectively (**Figure 1.6**).[15, 19, 22] The first studied O-type layered oxide Na insertion material was Na_xCoO_2, dating back to 1980s.[23] $NaNi_{0.5}Mn_{0.5}O_2$ and $NaFe_{0.5}Mn_{0.5}O_2$ are the two widely studied binary O3-type phase cathode materials.[24] $Na_{2/3}[Fe_{1/2}Mn_{1/2}]O_2$ cathode with P2-type phase structure has been found to deliver energy density higher than 500 Wh kg^{-1}.[25] Fe and Mn based oxides become more appealing when sustainability of battery fabrication starts to be taken into account. The main issue for those layered structure NaTMOs cathodes is unsatisfactory stability of host structure, resulting in capacity decay and limited reversible capacities. Substituting some TM ions, doping and composite-morphology design are often employed to improve the performance.[19, 21]

Polyanionic compounds are another dominant type of cathode materials. With open and stable structure frameworks, the cathodes can exhibit superior cycle life and safety. Furthermore, their enhanced redox potentials benefit from the inductive effect engendered by the polyanion. Inductive effect has been used to explain the positions of redox potential: the strong covalent bonding in the polyanionic group XO_4 with high electronegativity can induce a polarization of the M–O bond, which stabilizes the transition metal redox couple and thus raises the redox potential.[26, 27]

The great success of olivine $LiFePO_4$ cathode in LIBs has motivated researchers to study the electrochemistry of $NaFePO_4$ for Na storage. However, it has been found that maricite $NaFePO_4$ is thermodynamically stable by comparison with the olivine phase and considered lack of electrochemical activity.[28, 29] Although decent capacities (around 150 mAh g^{-1}) have been attained by nano-sized maricite $NaFePO_4$ and the

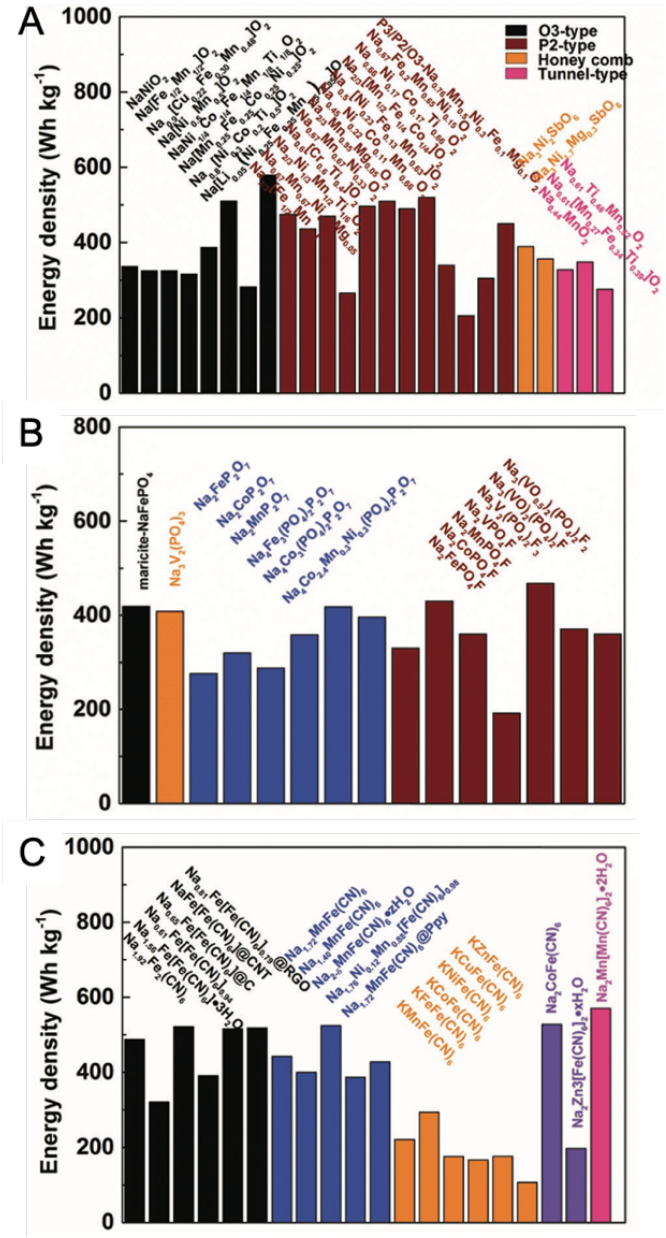

Figure 1.5 (A) Na_xMO_2, (B) phosphates and (C) Prussian blue types of cathode materials for SIBs and their energy density values.[30]

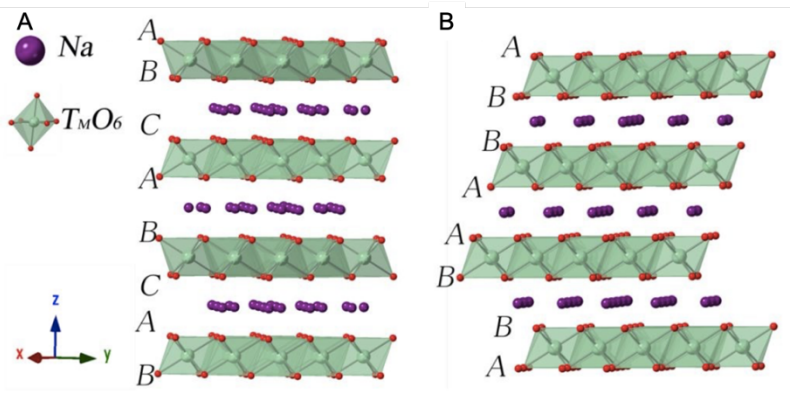

Figure 1.6 Crystal structure of (A) O3-phase and (B) P2-phase layered oxides.[15]

olivine phase can be prepared through complex ion exchange processes from olivine $LiFePO_4$, their rate capability is unsatisfactory, attributed to low electrical conductivity and sluggish diffusion of larger Na ions in the host materials.[31-33]

Na Super Ionic CONductor (NASICON) type polyanionic compounds have been utilized as cathode materials and some of them show very good Na storage performance.[34] $Na_3V_2(PO_4)_3$ is considered as a promising cathode material for SIBs, with high cycling stability and working voltage. Research has also been performed on many other polyanionic compounds as cathodes varying from different polyanions ($(PO_4)^{3-}$, $(P_2O_7)^{4-}$, $(SO_4)^{2-}$ and $(SiO_4)^{4-}$) to the mixture of them.[35] However, the poor electronic conductivity limits the electrochemical properties of this type of cathodes to some extent. For instance, the electronic conductivity of $LiFePO_4$ was calculated to be about 10^{-9} S cm^{-1} greatly lower than that of $LiCoO_2$ (2×10^{-1} S cm^{-1}).[36, 37] As a result, $LiFePO_4$ as cathode material often shows unsatisfactory power rate capability. Reducing the size of particles and

carbon coating have been studied as effective ways to improve the kinetic performance.[19]

Over recent years, other types of cathodes have also been extensively explored for SIBs. Prussian blue analogues (PBAs) have attracted much attention as a large family of transition-metal hexacyanoferrate cathode materials. The formula of PBAs for SIBs could be represented as $Na_{2-x}M[Fe(CN)_6]_{1-y}\square_y \cdot nH_2O$, in which x = 0–2, M are usually single or multi-transition metals (such as Fe, Mn, Co, Ni, etc), □ signify the vacancies occupied with coordinated water.[38] Typical crystal structures of PBA frameworks are displayed in **Figure 1.7**.[39] There are not only large ionic channels and interstices in the lattice for efficient Na ion diffusion, but also abundant redox-active sites with two redox centres ($M^{2+/3+}$ and $Fe^{2+/3+}$) to provide decent capacity.[39, 40] However, the water and vacancies can impede electrochemical performance and they suffer from poor rate performance and deteriorated long-term cycling stability.

Additionally, organic electrodes have been explored as alternatives to conventional inorganic cathodes, for their sustainability and universal availability in natural systems.[41] Unfortunately, the dissolution of organic electrodes in the electrolyte needs to be tackled to enhance electrochemical performance.

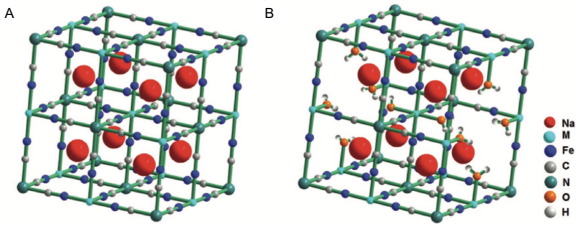

Figure 1.7 Crystal structures of PBA frameworks: (A) an intact $Na_2M^{II}[Fe^{II}(CN)_6]$ framework without structural defects and (B) a defective $NaM^{II}[Fe^{II}(CN)_6]_{0.75}\cdot\square_{0.25}$ framework with 25% $Fe(CN)_6$ vacancies existing in each unit cell.[39]

1.2 From Li-ion to Na-ion batteries: challenges and perspectives

While LIB technology is still at the forefront of the development, SIBs are considered as low-cost and sustainable alternatives to relieve severe pressure on resources and supply chains. Na and Li characteristics are compared in **Table 1.1**, with some of those also discussed in previous section. Despite the advantages in SIBs, the differences from LIBs and challenges in practice should be taken into serious account. Continuous research is required to understand how the redox behaviour of electrode materials and electrochemical performances would be affected when replacing Li by Na.

Table 1.1 Na and Li characteristics[42]

Sodium	Lithium	Category
1.06	0.76	Cation radius, Å
23 g mol^{-1}	6.9 g mol^{-1}	Atomic weight
−2.7 V	−3.04 V	E° (*vs.* SHE)
97.7 °C	180.5 °C	Melting point
$150 per ton	$5000 per ton	Cost, carbonates
Al $2000–2500 per ton	Cu $7000–8500 per ton	Cost, current collectors at the anode
1165	3829	Capacity (mA h g^{-1}), metal
Octahedral and prismatic	Octahedral and tetrahedral	A–O coordination preference

The available capacity of SIBs is intrinsically lower than that of LIBs when the same chemistry (redox species and host crystal structures) is used, due to heavier molar mass of Na. Many of the polyanionic cathode materials have been found to show inferior energy density for Na storage

as compared to their Li counterparts, as show in **Figure 1.8**.[11] In addition, larger cation radius can bring about more complex behaviours of Na ion insertion into / extraction from host materials. For instance, $LiCoO_2$ and $NaCoO_2$ have same frameworks in the structure but their redox potential profiles vary significantly, suggesting different phase evolutions during charge-discharge process (**Figure 1.9A**).[22] **Figure 1.9B** compares charge-discharge curves of $LiNi_{0.5}Mn_{0.5}O_2$ and $NaNi_{0.5}Mn_{0.5}O_2$ cathode materials synthesised via same method.[11, 43] The Na compound not only delivers less capacity but also exhibits sloping and lower operating voltage. Those facts suggest the different Na storage chemistry needs to be further studied and the low energy density for SIBs to be improved. Meanwhile, SIBs face the same issues as Li system, for example, electrolyte decomposition at high voltage and capacity fading upon cycling.[42]

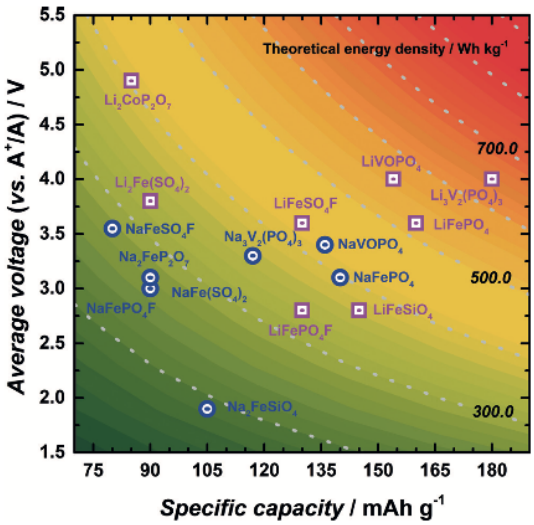

Figure 1.8 Comparison of average potential and discharge capacity for lithium ($LiFePO_4$, $LiFePO_4F$, $Li_2Fe(SO_4)_2$, $LiFeSO_4F$, $LiFeSiO_4$, $Li_2CoP_2O_7$, $LiVOPO_4$, $Li_3V_2(PO_4)_3$) and sodium compounds ($NaFePO_4$, $NaFePO_4F$, $NaFe(SO_4)_2$, $NaFeSO_4F$, Na_2FeSiO_4, $NaFeP_2O_7$, $NaVOPO_4$, $Na_3V_2(PO_4)_3$). The contour indicates the theoretical energy density obtainable (assuming a Li or Na metal as counter electrode).[11]

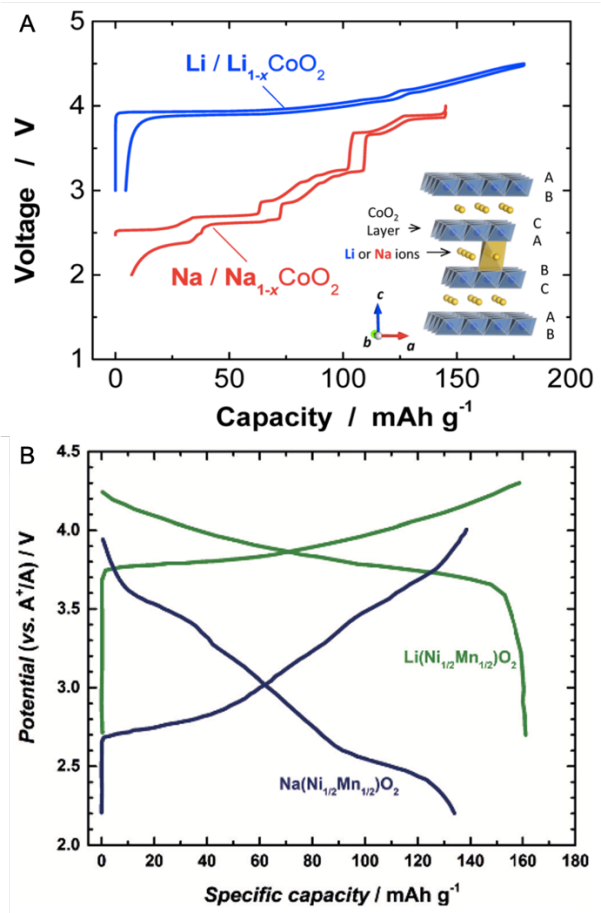

Figure 1.9 (A) Comparison of charge/discharge curves of $Li/LiCoO_2$ and $Na/NaCoO_2$ cells. Schematic illustration of $Li(Na)CoO_2$ is also shown.[22] (B) Voltage profiles (2nd cycle) of $LiNi_{0.5}Mn_{0.5}O_2$ and $NaNi_{0.5}Mn_{0.5}O_2$.[11]

Cathode material as one of the most important components in a battery largely determines the energy density and power rate capability of the batteries. Besides exploiting the same chemistries in LIBs, development of new cathode materials especially those based on abundant elements can bring along large opportunities to achieve low-cost, sustainable and high-performance SIBs. **Scheme 1.1** summarizes the emerging cathode

materials commonly applied in SIBs and their advantages as well to offer inspiration for the development of high-performance cathode materials for Na storage.[44] Layered metal oxides and polyanionic compounds which are typical cathode materials for LIBs, have been extensively investigated for SIBs. Moreover, while PBAs have become another main research subject as cathode materials for SIBs, organic cathode materials have attracted increasing attention.

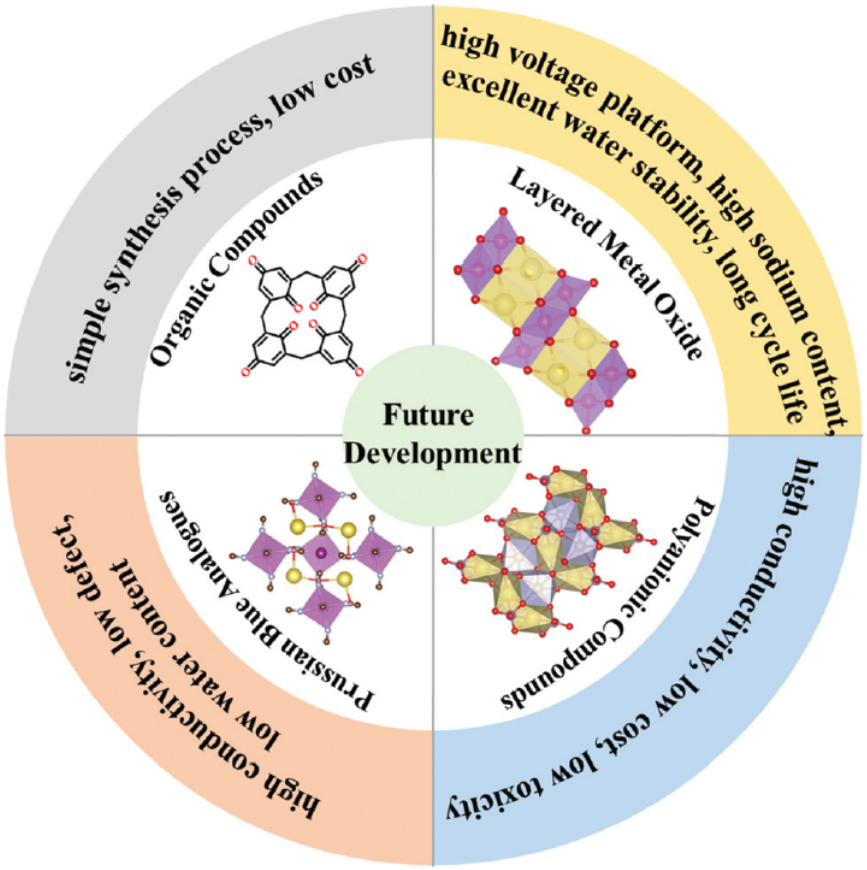

Scheme 1.1 Future development of the cathode materials for SIBs.[44]

With theories, principles and experimental and practical methods for research and development of SIBs established and understood, as well as consideration of both similarity and differentia to LIBs, we can foresee SIBs as sustainable, cost-effective alternatives to LIBs for applications such as short-range electric vehicles and large-scale energy storage. While development of all components for SIBs is highly required, we believe that new finding and understanding in cathode materials can positively affect acceleration of further developments of SIBs.

1.3 Design and engineering for inorganic cathode materials

In previous sections, typical categories of cathode materials for LIBs and SIBs have been introduced, by which new cathode material design can be inspired. **Scheme 1.2** summarizes main and combined strategies and concepts employed for selection of cathode materials as research object and for design of new ones in the thesis. Most of those were conceived based on developed cathode materials in literature and thus the relevant contents will be summarized in this section.

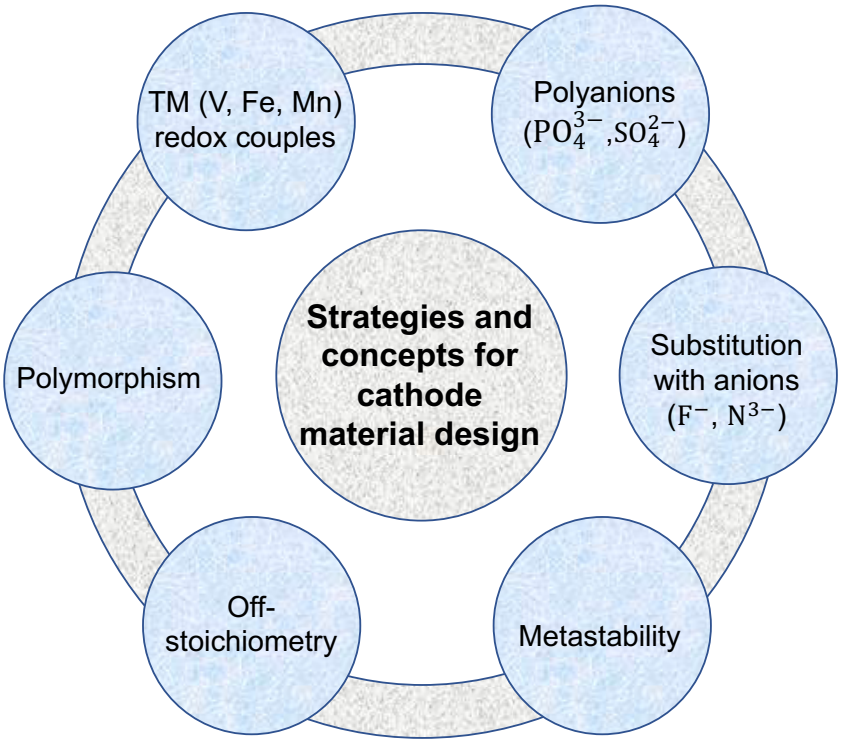

Scheme 1.2 Strategies and concepts for cathode material design in the thesis.

1.3.1 Transition metals used in cathode materials

With an overview of today's cathode materials, one can find that transition metals (TMs) play a dominant role in battery cathode materials.[7, 45-47] These 3d TMs (Ti, V, Cr, Mn, Fe, Co, Ni and Cu) are commonly used and often as redox couples in the cathode host, determining some key charge storage properties of the batteries (e.g. energy density). The abundance and cost of the elements vary significantly (**Figure 1.10A**), and the highly abundant, low-cost and environmentally friendly ones (**Figure 1.10B**) are favourable to sustainable development of battery technologies.[16, 48]

Among the TM-based cathode materials, vanadium oxides (VO_x) have very rich chemistries due not only to multiple oxidation states (II–V) but also various crystalline structures. VO_x, especially V_2O_5, have been heavily investigated as cathode materials for LIBs and the first studies can date back to 1979.[49] Furthermore, the electrochemical behaviours of V_2O_5 have also been explored for SIBs and other alkali and alkali-earth ion batteries.[50] Although V is more abundant than cobalt in Earth's crust, it is not a very cost-effective and eco-friendly choice in comparison to the other TMs in **Figure 1.10**.

Fe is the cheapest transition TM and extremely widely distributed in the Earth's crust (the most representative element within the marked circle in **Figure 1.10A**). Moreover, it is nontoxic and naturally recycled, an eco-friendly element. Although conventional Fe-based cathode materials face the shortcoming of low energy density, it can be enhanced by material design techniques such as element doping or substitution, and exploration of new materials.[48] Therefore, considering the remarkable advantages of high abundance, low cost and sustainability, Fe-based cathode materials can be considered as encouraging candidates for SIBs.

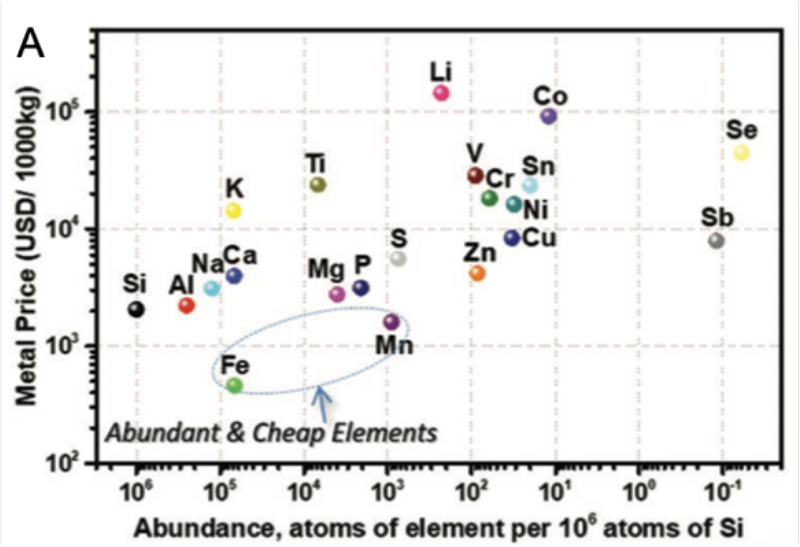

Figure 1.10 (A) Relationship between the elements' abundance in the Earth's crust (continental) and metal prices.[48] (B) Mismatch between the TM elements constituting biomass and the main constituents of our present LIBs. Biomass (that is, naturally recycled) elements are shown in green (minor in light green, traces in pale green). Present LIBs main elements are circled in red. The arrow indicates the evolution the battery-constituting elements should follow to better match sustainability issues.[16]

1.3.2 Polymorphism in cathode materials

In materials science, polymorphism describes the ability of a solid material to exist as more than one crystalline phases that have different unit cell configurations but are otherwise identical in terms of chemical content.[51, 52] It is a common phenomenon of crystalline materials and many crystalline materials can form various polymorphs with different physicochemical properties. Therefore, polymorphism broadens the possibilities of cathode materials and offers an aspect of discovery of new cathode materials.

Many cathode materials have been found to exhibit polymorphic forms. VO_2 is one typical example and has a number of polymorphs, including VO_2(B), VO_2(A), VO_2(M) and VO_2(R).[53, 54] Their crystal structures are displayed in **Figure 1.11**.[55] Among those, the metastable VO_2(B) with an open low-symmetry monoclinic structure shows the most attractive electrochemical performance.[56, 57]

Two polymorphs of $LiFeSO_4F$, tavorite and triplite, have been reported as cathode materials to show different potentials, 3.64 and 3.90 V (vs. Li^+/Li), respectively.[58] Interestingly, Mn substitution for Fe in $Li(Fe_{1-\delta}Mn_\delta)SO_4F$ was found by Tarascon's group to trigger a transformation from the tavorite to the triplite structure, with a resulting increase of 300 mV in the Fe^{2+}/Fe^{3+} redox potential (**Figure 1.12**).[59] The triplite phase $Li(Fe_{0.9}Mn_{0.1})SO_4F$ exhibits reversible capacities of around 125 mAh g^{-1} at 3.90 V (vs. Li^+/Li), compared with similar capacities at nearly 3.6 V for its tavorite counterpart.

Very recently, higher experimental Na-ion diffusion coefficient has been found in a new monoclinic α-polymorph of Na_2FePO_4F than orthorhombic β-polymorph.[60] Polymorphs also exist in some other polyanionic cathode materials, such as $NaVP_2O_7$, $Na_2CoP_2O_7$, $VOPO_4$ and

Li_2FeSiO_4.[27, 61, 62] Exploration and comparison of polymorphs in cathode materials can support the understanding of their different electrochemical behaviours and assist researchers in looking for those with superior charge storage properties.

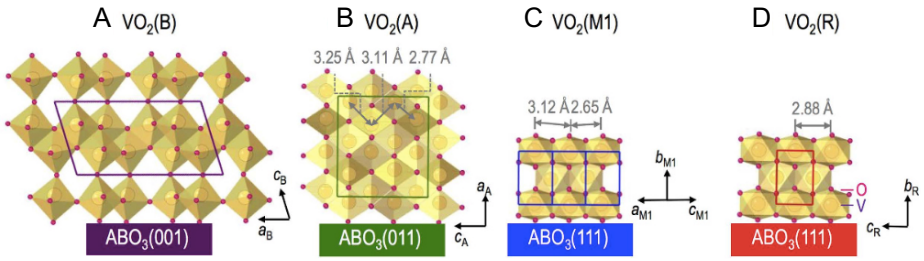

Figure 1.11 Schematics of (a) VO_2(B), (b) VO_2(A), (c) VO_2(M1) and (d) VO_2(R) phases grown on various perovskite substrates with different crystallographic orientations, i.e., ABO_3(001), ABO_3(011) and ABO_3(111), respectively.[55]

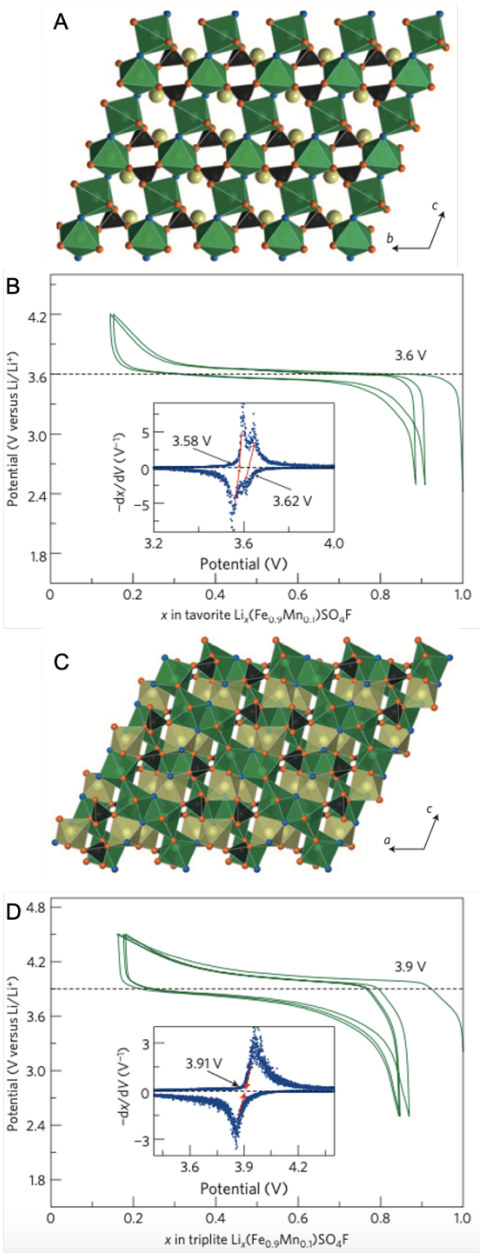

Figure 1.12 Crystal structure of (A) tavorite and (C) triplite phase for $Li(Fe_{0.9}Mn_{0.1})SO_4F$. Charge and discharge curves for the (B) tavorite and (D) triplite phase at a C/20 rate. The derived curves are plotted as a function of V.

1.3.3 Metastability in cathode materials

In materials science, metastability is a valuable concept utilized to design and discover new materials. Metastable phases are those under metastable state in a free energy system, and a metastable state occupies a local minimum in free energy, rather than the absolute minimum corresponding to the stable state, as schematically shown in **Figure 1.13**.[63, 64] They tend to transform to lower-energy phases by driving the state of the material over a neighbouring energy maximum, namely an unstable state. Several possible metastable conditions can exist for a system and they are selected by kinetics.

Typical metastable materials include those in amorphous state often prepared by melt-quenching method or mechanochemical processes, and metastable crystalline phases synthesized via optimised heat treatment of particular precursors or crystallization of glasses. $NaFePO_4$ composition system is one example, in which the amorphous, metastable olivine and stable maricite phases have been investigated as cathode materials for SIBs (**Figure 1.14**). The amorphous and olivine $NaFePO_4$ cathodes are electrochemically active, whereas the stable maricite analogue lacks activity because of its blocked Na ion diffusion pathway in the structure.

Synthetic methods and processes are important for the formation of the metastable materials, especially for the metastable crystalline phases which could be kinetically trapped. Various techniques to synthesize this type of cathode materials are first summarized in this section. We then present recent progress of amorphous and metastable crystalline compounds as cathode materials for LIBs or SIBs, with focus on some typical examples for comparison and discussion. Moreover, challenges and new perspectives are highlighted.

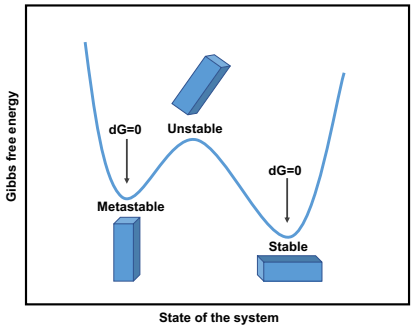

Figure 1.13 Schematic behaviour of free energy of a thermodynamic system with simple model illustration of possible metastable, unstable and stable states.

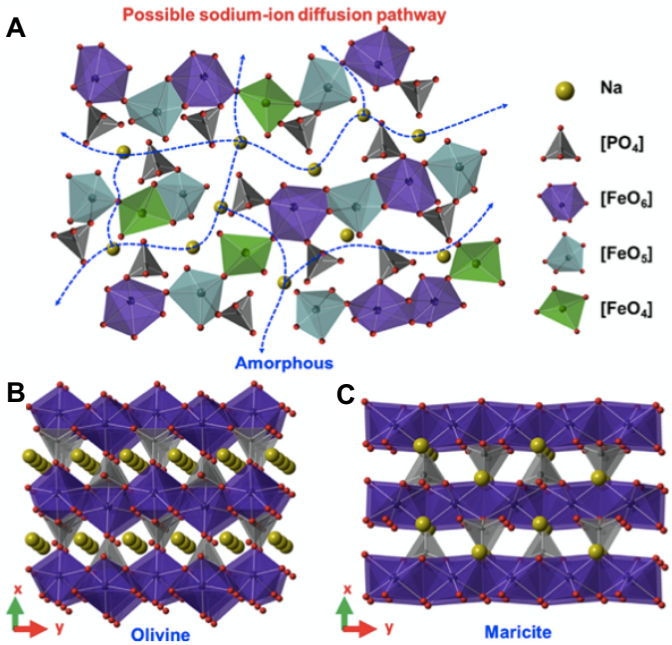

Figure 1.14 (A) Possible Na-ion diffusive pathways and atomistic structure for amorphous $NaFePO_4$. Structural sketching diagrams of (B) olivine-type $NaFePO_4$ and (C) maricite-type $NaFePO_4$.[65]

1.3.3.1 Synthesis of metastable cathode materials

Unlike many stable cathode materials which can be produced feasibly by traditional solid-state reactions, some kinetic trapped metastable cathode materials could face challenges in their synthesis. That could be one reason of their inadequacy of researchers' attention and number in comparison to the wide variety of stable counterparts. As the development of material design and modelling, and advancement in synthesis techniques as well, more and more this type of cathode materials has been discovered and investigated to show promising charge storage performance. The synthesis methods are summarized in **Scheme 1.3**.

Amorphous materials are one kind of metastable materials and characterized by long-range atomic disorder. Note that glasses which show a distinct glass transition temperature, can be considered as a subset of amorphous compounds and glass cathode materials will also be presented herein. Various approaches can be applied to amorphize or vitrify materials. Melt-quenching is a typical method to prepare glasses, while other techniques such as sol-gel synthesis and vapour deposition can also be employed.[66] Moreover, via solution routes and by the destruction of crystalline structures (e.g. mechanical milling) can amorphous materials also be made.[67, 68]

A variety of methods have been used for the synthesis of amorphous cathode materials. For instance, melt quenching made the formation of glass cathode materials in $xFeO–(100\text{-}x)NaPO_3$ ($x \leq 45$), vanadate–phosphate ($V_2O_5–P_2O_5$) and $A_xB_yCu(\frac{1}{2}PO_3 \bullet \frac{1}{2}VO_3)_{2+x+y}$ (A&B are alkali cations) systems.[69-71] Ball milling is a feasible way to produce amorphous cathode materials and ball milled amorphous $xLiF–FeSO_4$ and $xNaF–FeSO_4$ ($x<1.5$) systems are two examples.[72, 73] Dehydrate was found to induce amorphization of several cathode materials, including

Na_2MoS_4, $FePO_4$ and FeF_3.[74-76] In addition, amorphous thin films (e.g. $Li_xM_yPO_z$ (M = Ni, Cu, Co, Mn, Au, Ag, Pd), $LiMn_2O_4$) can be obtained via sputtering deposition and utilized as cathode in all-solid-state batteries.[77, 78] The amorphous $FeVO_4$ nanoparticles have been prepared by a new and facile electrostatic spray assisted coprecipitation method, followed by a low-temperature thermal treatment.[79] Those approaches enable easy access to various amorphous cathode materials.

In contrast, the synthesis of metastable crystalline materials can be complex and the formation of this class of materials can be understood through some reaction driving parameters.[80] Among these, the exploitation of lowering the activation energy is well-known. Note that a large number of metastable phases are synthetically inaccessible by conventional high-temperature solid-state reaction synthesis, because large energetic barriers to diffusion in bulk solids require elevated synthesis temperature to overcome and the most stable phase or mixture of phases tend to form during solid–solid reactions under the influence of thermodynamic product selection.[80, 81] Therefore, methods that can reduce the diffusion length and lower the barriers to diffusion are favourable to the production of metastable phases.

Solid-state synthesis is a conventional method for production of cathode materials. It often requires high temperature for precursors of starting materials to form desired products which are usually thermodynamically stable. Some impurity residuals often form during the process and the purity of the products depends on precursors mixture and sintering conditions. Large particle size and agglomeration morphology of the products with small surface area is another drawback of this method. Mechanochemical activation of the precursors, such as high-energy ball milling, has been adopted to overcome that.[82] The ball milling enables intimate mixing of starting materials and some reactions could possibly

occur during the process, significantly reducing the diffusion length and the barriers to diffusion for subsequent sintering. Therefore, the influence of thermodynamic product selection could be avoided and presumably, new metastable phases could be more likely to form at low or moderate temperature for certain compounds.[83] Additionally, it is also an effective way to achieve homogeneity and small particle size, preparation of composites with carbon and doped samples, which has been extensively employed for the synthesis of common cathode materials.[82]

Ion exchange is considered as an effective way to prepare metastable phases as cathode materials. For instance, olivine $NaFePO_4$ cathodes have been prepared via ion exchange from olivine $LiFePO_4$ by electrochemical method.[31] Moreover, there are also some newly established or combined routes to obtaining cathode materials in crystalline metastable state, which includes microwave-assisted hydrothermal synthesis, topotactic molten salt reaction at low temperature (≤100 ˚C), ionothermal synthesis and so on.[84-86]

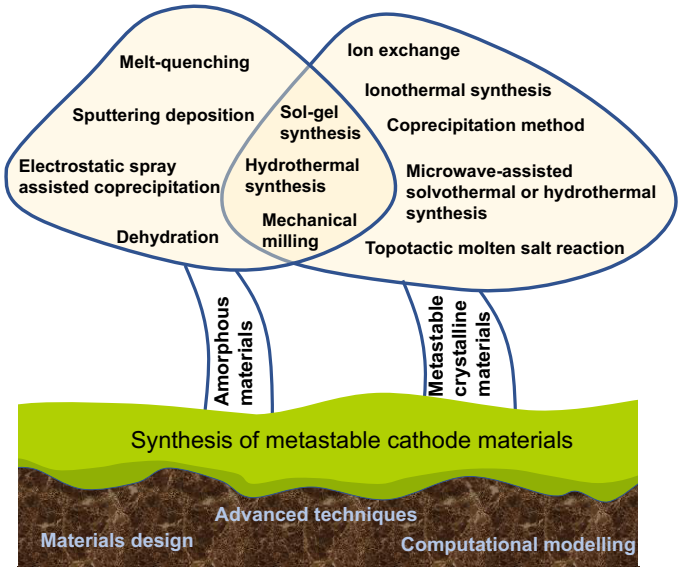

Scheme 1.3 Synthesis methods of metastable cathode materials.

1.3.3.2 Amorphous cathode materials

Amorphous cathode materials have caught much attention for lithium and sodium storage, because their short-range structural ordering offers free volume for cation accommodation, so that improved specific capacities and stable charge-discharge cycling could be achieved. Moreover, the compositions for certain compounds can be tailored flexibly and properly to attain a variety of amorphous cathode candidates.

As a distinctive type of amorphous compounds, glasses have witnessed electrochemical activity in some systems. The electrochemical activity of Na_2O-FeO-P_2O_5 glasses has been examined as cathode by Honma's group, suggesting that this type of glasses with open structure and Na ion diffusion channels could be promising for Na storage.[69] Du et al. found that vanadate-phosphate glass as cathode for LIBs delivered a high capacity of 243 mAh g^{-1} and excellent rate capability and long-term cyclic performance were attained.[70] A series of mixed polyanion glasses systematically reported by Kercher can undergo both intercalation and glass-state conversion (GSC) reactions and thus deliver high capacities (200–500 mAh g^{-1}).[71, 87-89]

Among other amorphous solids as cathode materials, iron-based type is one of the most popular ones and has been summarized in a recent review paper.[90] More recently, amorphous $FePO_4$ cathode materials were reported to show excellent rate capacity and cycling stability for both Li and Na storage, by constructing composites with carbon and morphology design.[91, 92] In addition, impressive potassium, zinc and magnesium ions insertion and extraction for amorphous $FePO_4$ host have been surveyed by Kim and co-workers, suggesting this class of cathode materials are also advantageous for larger cation storage.[75]

Amorphous vanadium oxides have also been explored as cathode materials. Improved Na storage performance of amorphous V_2O_5 has been discussed in literature.[90, 93] Another report shows that amorphous VO_2 and V_2O_5 thin films can deliver higher capacity than their crystalline counterparts.[94]

1.3.3.3 Crystalline metastable cathode materials

Another category of metastable materials are those intermediate crystalline phases under metastable state. The metastable phases are considered to have large molar volumes and high symmetric crystalline structures, favourable for ion conduction and thus have been investigated as solid electrolytes.[95] Nevertheless, a limited number of reports have explored the electrochemistry of metastable phases as cathode materials, compared to the stable ones.

A metastable phase could be one of polymorphs for a compound composition. VO_2(B) is a well-known metastable phase widely studied as cathode material, whereas its stable VO_2(M) counterpart barely exhibits electrochemical activity.[96, 97] That can be explained by the open layered structure of VO_2(B) beneficial to efficient metal ion accommodation, compared with the dense layout of [VO_6] octahedrons in the crystal structure of VO_2(M1) as shown in **Figure 1.11**.

Similarly, due to the blocked Na ion diffusion pathway in the crystal structure of stable maricite $NaFePO_4$ (**Figure 1.14**), it lacks electrochemical activity. In contrast, metastable olivine $NaFePO_4$ and $Na(Fe_{0.5}Mn_{0.5})PO_4$ exhibit reversible electrochemical de/intercalation of Na ion, which benefits from the open diffusion channels for Na ion transport. [85, 98]

Partially dehydrated sodium birnessite ($Na_{0.27}MnO_2 \cdot 0.09H_2O$) characterized as a metastable spinel-like phase, has witnessed an unprecedented reversible phase transformation between layered and spinel-like structure during reduction/oxidation of a layered-structure oxide, as illustrated in **Figure 1.15**.[99] The formation of the metastable spinel-like phase containing small amount of crystal water during ion extraction enables this unusual reversibility, resulting in improved charge / discharge cycling stability and power rate capability for Na storage. Some other metastable cathode materials (e.g. $Na_3V_2O_2(PO_4)_2F$ and $LiFe_{1-x}(VO)_xPO_4$ ($0 \leq x \leq 0.25$)) have also been explored to show promising energy storage performance.[84, 100] Those findings enriched the metastable phases as cathode materials for next-generation rechargeable batteries and should capture our interest for more investigation of metastable cathode materials.

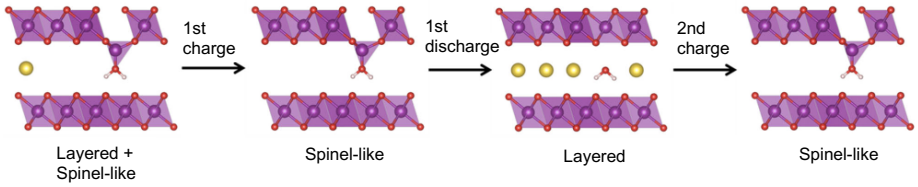

Figure 1.15 Schematic illustration for the reversible structural changes of partially dehydrated sodium birnessite during Na ion insertion/extraction.[99] The red balls represent O atoms, the purple balls represent Mn atoms, the light pink balls represent H atoms and yellow balls represent Na atoms.

1.3.4 Off-Stoichiometry in cathode materials

Non-stoichiometric compounds are chemical compounds with an elemental composition that cannot be represented by a ratio of well-defined natural numbers, in contrary to stochiometric compounds. For example, the actual stoichiometry of wüstite (ferrous oxide) is closer to $Fe_{0.95}O$ rather

than the ideal (stoichiometric) formula FeO. The formula for wüstite is written as $Fe_{1-x}O$, where x is a small number, representing the deviation from the "ideal" formula.[101] It is also termed off-stoichiometry in literature.

Nonintegral element ratio in the compositions makes this class of materials more flexible in tuning the compositions and thus the properties. Off-stoichiometry has been applied in cathode materials design, so as to obtain novel cathode material candidates with improved energy storage performance.[27] There are a number of off-stoichiometric materials investigated as cathode materials. Yamada and co-workers surveyed the Na_2SO_4-$FeSO_4$ binary system and found stable off-stoichiometric phases in $Na_{2+2x}Fe_{2-x}(SO_4)_3$, inspiring further improvement of the alluaudite-type Na metal sulfates for advanced SIBs. [102] In a Li-Mn-spinel system, Mn ions are partly replaced by Co^{3+}, Y^{3+}, and Ga^{3+} ions used as co-dopants, while F^- partly substitutes for O^{2-}, resulting in the non-stoichiometric spinels $Li_{1.02}M_xMn_{1.95}O_{4-y}F_y$ with better cycling performance than $LiMn_2O_4$. Besides, an off-stoichiometric phase manganic pyrophosphate $Na_{3.12}Mn_{2.44}(P_2O_7)_2$/C has been investigated for Na storage to achieve an impressive reversible capacity of 114 mAh g^{-1} and a high energy density of 376 Wh kg^{-1}. A variety of phosphate-based off-stoichiometric cathode materials have also been studied, including $Na_{3.42}Fe_{2.44}(P_2O_7)_{2.05}$, $Na_{3+3x}V_{2-x}(PO_4)_3$ and $Li_{2.7}Ti_2(PO_4)_3$.[103-105] Those examples broaden the range of possible cathode material candidates.

Off-stoichiometry can be employed not only for phase engineering of known cathode materials but also as a concept to design new cathode materials. $Na_{0.71}Fe_{1.07}PO_4$ and $Na_{0.6}Fe_{1.2}PO_4$ are two examples of novel off-stoichiometric materials with great potential as low-cost cathode material candidates for SIBs.[106, 107] However, those new off-stoichiometric phases often bring about the challenges for researchers to solve their crystal

structures and further understand their electrochemical behaviours. How the off-stoichiometry affects the phase structure and electrochemical performance requires further investigation, so that this concept can be better utilized for discovery of high-performance electrode materials.

1.3.5 Rich chemistries in VO_x as cathode materials

Vanadium is a common transition metal and has four oxidation states of V^{2+}, V^{3+}, V^{4+}, and V^{5+} which can form oxides of VO, V_2O_3, VO_2, and V_2O_5, respectively. Additionally, there are also combined oxidation states of vanadium in oxides such as V_6O_{13}, V_6O_{11} and so on. With their structural flexibility and interesting chemical and physical properties, VO_x have been widely utilized in many fields such as catalysis,[108] chemical sensors[109] and energy storage.[96] Besides, vanadium is more abundant than cobalt and therefore V-based chemistries could be interesting and lower-cost alternatives over the conventional cobalt-based chemistries, which makes them further attractive for researchers in the energy storage community.[97, 110]

When applied as electrode materials for LIBs, VO_x have been found to exhibit rich electrochemistry due to the availability of different valence states and phase structures.[7, 111-115] The structures of typical VO_x are shown in **Figure 1.16** and their lattice parameters and electrochemical properties are compared in **Table 1.2**. The structures of these four VO_x are formed by different arrangements of atoms in [VO_6] octahedral layers. Vanadium is located at the centre site of the polyhedron and the octahedrons [VO_6] are connected by corner-sharing or edge sharing geometries, attributed to the different compositions.[116] The various compositions and structures have a direct impact on their electrochemical behaviours.

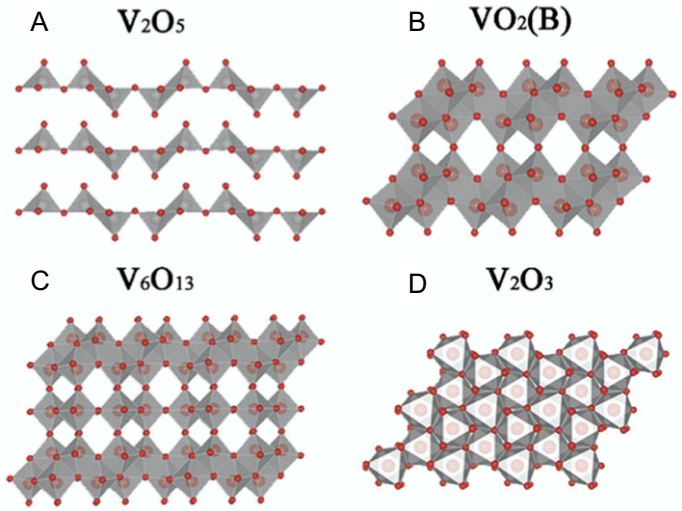

Figure 1.16 Crystal structures of various VO_x, the smaller red balls represent oxygen atoms and the big ones represent vanadium atoms.[115, 116]

Table 1.2 Structure and electrochemical properties comparison of four VO_x.[115]

VO_x	Lattice parameter	Theoretical capacity (mAh g^{-1})	Voltage plateaus	Li^+ diffusion coefficient (cm^2 s^{-1})	Electronic conductivity (S cm^{-1})
V_2O_5	Orthorhombic a = 11.517 Å b = 3.568 Å c = 4.375 Å α = 90°	147 ~ 1Li^+ 294 ~ 2Li^+ 441 ~ 3Li^+	~3.4 V ~3.2 V ~2.3 V ~2.0 V	6.5×10^{-13}	10^{-2} ~ 10^{-3}
VO_2(B)	Monoclinic a = 12.03 Å b = 3.693 Å c = 6.42 Å β = 106.6°	160 ~ 0.5Li^+ 322 ~ 1Li^+	~2.5 V	10^{-10}	7.2×10^{-7}
V_6O_{13}	Monoclinic a = 11.92 Å b = 3.68 Å c = 10.14 Å β = 100.9°	420 ~ 8Li^+	~2.3 V ~2.8 V	3×10^{-9} ~ 8×10^{-10}	10^{-2}
V_2O_3	Rhombohedral a = 4.828 Å c = 14.146 Å α= 120°	356 ~ 2Li^+ 1070 ~ 6Li^+	~0.55 V ~1.79 V	NA	10^3

The unique layered structure of V_2O_5 can provide space for not only Li but also Na ion diffusion. There are multiple phases formed with the progress of lithiation in V_2O_5. The phase transformation steps and electrochemical reactions are listed in **Table 1.3**. The theoretical specific capacity of one Li ion intercalation is 147 mA h g^{-1}, which can be attained in a narrow charge-discharge potential window ($\approx$ 2.5–4 V vs. Li^+/Li). Although more Li ion inserted, higher the capacity, the formation of ω-$Li_xV_2O_5$ (x>2) is often irreversible, which can cause rapid capacity loss. Therefore, it is important to adjust the potential window to avoid the irreversible phase and keep the decent and stable capacity upon charge-discharge cycling.

VO_2(B) has also attracted much research attention as cathode materials for LIBs and SIBs. Its crystal structure consists of [VO_6] octahedron bilayers with abundant tunnels for fast Li ion diffusion and insertion/extraction. However, it also suffers from capacity fading during deep lithiation and thus wise choice of potential range has been found to improve charge-discharge cycling stability.[96]

Table 1.3 Five phases of the lithiated vanadium oxide ($Li_xV_2O_5$) and the electrochemical reactions of phase transformations.[117]

$Li_xV_2O_5$ phase name	*x* value range	Li-ion intercalation reaction	Equilibrium potential (V vs Li/Li^+) of Li^+ intercalation reaction (discharging)
α (alpha)	$0 < x < 0.01$		
$\alpha \leftrightarrow \varepsilon$		$\alpha\text{-}V_2O_5 + 0.5Li^+ + 0.5e^- \leftrightarrow \varepsilon\text{-}Li_{0.5}V_2O_5$	≈3.3
ε (epsilon)	$0.35 < x < 0.7$		
$\varepsilon \leftrightarrow \delta$		$\varepsilon\text{-}Li_{0.5}V_2O_5 + 0.5Li^+ + 0.5e^- \leftrightarrow \delta\text{-}LiV_2O_5$	≈3.1
δ (delta)	$0.7 < x < 1$		
$\delta \leftrightarrow \gamma$		$\delta\text{-}LiV_2O_5 + 1Li^+ + 1e^- \leftrightarrow \gamma\text{-}Li_2V_2O_5$	≈2.2
γ (gamma)	$1 < x < 2$		
$\gamma \leftrightarrow \omega$		$\gamma\text{-}Li_2V_2O_5 + 1Li^+ + 1e^- \leftrightarrow \omega\text{-}Li_3V_2O_5$	≈1.9
ω (omega)	$2 < x < 3$		

V_6O_{13} is one of the most representative mixed-valence VO_x and regarded as a promising cathode material for LIBs. In its crystal structure, there are alternating single and double [VO_6] octahedron layers with mixed-valence vanadium of V^{5+}/V^{4+}. Theoretically, it can deliver the capacity of 420 mAh g^{-1} given all vanadium ions reduced to V^{3+}. Furthermore, it has been found to show a metallic property at room temperature, namely good electronic conductivity.[116]

The typical crystal structure of V_2O_3 is rhombohedral corundum-type, with [VO_6] octahedrons and 3D V–V chains. There are abundant tunnels for the intercalation/deintercalation of Li ions, which provides theoretical capacity of 356 mAh g^{-1} (2 Li intercalation). Its intrinsic metallic behavior makes them exhibit high electronic conductivity.[96] Although V_2O_3 has been investigated as both cathode and anode materials for LIBs, it can deliver higher capacity as anode materials since more Li ions can participate in the redox process at low potential.

1.3.6 Fluorine substitution in polyanionic cathode materials

Among the cathodes, polyanion type cathodes are one of the most significant categories, especially with respect to stability and safety. Nevertheless, they have heavy molecular weight and thus face the disadvantage of low specific capacity. Introducing fluorine (F) ions into the polyanionic compounds is often employed for promotion of the energy density of the electrodes.

The high electronegativity (simply put as electron attracting ability) of fluorine can induce higher ionicity of the M-F bond and thus increased potential of the $Mn^{n+}/Mn^{(n-1)+}$ redox couple. Na_2FePO_4F, $Na_3V_2(PO_4)_2F_3$ and $Na_3(VOPO_4)_2F$ have been widely investigated for Na storage, with

higher redox potential than their phosphate analogues.[118, 119] Additionally, improved theoretical specific capacity can benefit from the lightweight fluorine.

1.4 Scope of this thesis

With an overview and comparison of cathode materials for LIBs and SIBs, and some relevant chemistries in Chapter 1, we can find that the ways to attain superior charge storage performance of cathode materials mainly go into two directions. One is to have in-depth mechanistic understanding of developed materials, tackle shortcomings and thus improve the performance. Another follows design and discovery of new materials to show great potential as advanced cathode materials, which then flows into the first direction stream. The aim of this work was not only to offer new insights in the known cathode materials, but also explore innovative cathode materials.

Our first objective was to do comparative study in charge storage mechanism of cathode materials for both LIBs and SIBs. VO_x have been extensively investigated over the past years as promising cathode materials for alkali ion batteries owing to their rich and interesting electrochemical properties. Further improvements on VO_x active materials have been possible by going at nanoscale as well by realising hierarchical composites with various carbon allotropes. Herein, a library of VO_x@rGO composites were controllably synthesised via facile methods and characterized with different vanadium oxidation states, morphologies and phases. Their electrochemical behaviours for Li and Na storage were systematically analysed and compared. We found that the Na storage performance of all the studied materials is inferior to the Li storage.

Although VO_x are very important cathode materials for development of emerging metal-ion batteries, the relatively high price of vanadium, toxicity of some oxides, sluggish Na storage performance make them not highly promising for sustainable SIBs. Then, low-cost, environmentally

benign and stable Fe-based polyanionic cathode materials were targeted to develop new cathode materials for SIBs in following work.

Inspired by the knowledge on reported $NaFePO_4$, Na_2FePO_4F, $NaFeF_3$ and $Na_{0.6}Fe_{1.2}PO_4$ cathode materials, as well as the chemistries introduced in this chapter, we synthesised a series of linear combinations of these with the empirical formula of $Na_{0.6+x}Fe_{1.2}PO_4F_x$ (with analysed values of x = 0, 0.2, 0.4, 0.6, 0.8 and 1). Moreover, amorphous, metastable and stable materials were discovered in the $Na_{1.2}Fe_{1.2}PO_4F_{0.6}$ (x=0.6) composition through the focused analyses. All the studied materials exhibit electrochemical activity for Na storage and the metastable $Na_{1.2}Fe_{1.2}PO_4F_{0.6}$ shows excellent performance, unlocking the great potential of Fe-PO_4-F cathode material space.

Finally, $Na_{0.6}Fe_{1.2}PO_4$ was found to show bizarre cycling activation behaviours which is contradictory to the origin and only publication.[107] Thus, it attracted our attention for further investigation. In our work, the material was reproduced with the same phase by similar method and improved electrochemical performance was attained by electrolyte formula optimization. Surprisingly, it shows an increase in capacity upon charge-discharge cycling and capacities higher than theoretical value (C_{th}=91 mA g^{-1}) can be attained. Characterizations combined with electrochemical analyses were performed to understand the activation mechanisms.

This work is not only alive with new insights in electrochemical behaviours of the previously reported cathode materials but also with plentiful material design concepts adopted and combined to explore new cathode material. The findings reveal the significance of critically comparative study of different electrode materials and charge storage systems so that appropriate ones can be selected as potential candidates wisely. Moreover, new discoveries of materials with high all-round

performance can bring great opportunities to make breakthroughs in innovation of advanced energy storage systems.

CHAPTER 2 – Versatile Synthesis of Vanadium (III, IV, V) Oxides@rGO Nanocomposites and Evaluation of Their Li and Na Storage Performances

Abstract

VO_x have been extensively investigated over the past years as promising electrode materials for alkali ion batteries owing to their rich and interesting electrochemical properties. Further improvements on electrochemistry of VO_x materials have been possible by going at nanoscale as well by realising hierarchical composites with various carbon allotropes. However, the nanocomposites synthesis methods are not always efficient, nor green, requiring either expensive precursors, extended synthesis time or harmful reagents. Herein, we report on rapid and environmentally friendly synthesis methods of a library of VO_x@rGO composites via impregnation and hydrothermal protocols using cheap and commercially available V_2O_5 precursors. Different oxidation states, crystalline phases and nanoscale morphologies can be reproducibly accessed and their physicochemical properties have been characterized. The electrochemical properties (Li and Na ion storage) of the synthesized VO_x@rGO nanocomposites and phases have been critically compared but also as compared to commercial (CM) VO_x - based electrodes. Whereas

nanostructuring is found to impact the power-rate performances, the amount of stored charge and the cycling stability are sensitively dependent on the cycling potential window, while being minorly affected by the morphology and synthesis method. The composites are also found to exhibit different electrochemistry for Na storage, with more sloping potential profiles. Peculiarly, the synthesized V_2O_3@rGO composite shows no signs of electrochemical activity pointing towards the electrochemical inertness of this particular V_2O_3 composite and phase. This work could serve as reference for future developments on this class of important battery materials as it is one of the few studies describing a comprehensive and comparative study of several different influence parameters on the electrochemical behaviour of VO_x in different oxidation states, crystalline phases and morphologies.

2.1 Introduction

When analysing the progress in the field of VO_x battery materials, a series of main aspects appear as the most important to understand but also enable efficient energy storage with VO_x as electrode material, namely:

- (i) nanostructuring, with the addition of carbon composites has a crucial effect on electrochemical performance and in particular on power-rate capability.
- (ii) phase structure and composition affect the electrochemical properties, and in particular the potential profile and the attained charge storage capacities; despite, the redox potential cycling window seemingly affects the first cycle efficiency but also the overall capacity retention upon cycling, an aspect that still remains poorly explored thus far.
- (iii) whereas many V_2O_3 phases are reported to be electrochemically active, herein we find one particular phase and nanoscale morphology that shows no electrochemical activity, requiring further in-depth studies to understand the origin of this peculiar behaviour. Additionally, the lowest attained valence for electrochemical lithiation of vanadium oxide - based compounds found in literature is around III.
- (iv) finally, most of the reports to date deal with the electrochemical performance enhancement using methods in (i) and (ii), yet limited to only one (and rarely few) vanadium oxide composition (valence state), nanoscale morphology or phase in a one single study. A clear comparison of the impact of these is difficult since also different procedures for cell assembly and testing are used. Altogether, these points require a comparative analysis of VO_x electrochemistry in order to select the most performing candidates.

While further detailing the criterion (i) - VO_x have intrinsic poor electrical conductivity and slow cation de/insertion kinetics.[110, 111, 120]

Consequently, two main strategies have been extensively applied to overcome these drawbacks and attain full material utilisation at also high current densities. Nanostructuring has been regarded as one of the most effective strategies to improve electrochemical performance of electrode materials. The nanostructured morphology not only shortens Li-ion and electron transport distances in electrodes, but also enables active materials and composite electrodes to sustain volume changes and stresses during cycling, resulting in improved power-rate capability and stability of the active material as well as of the electrode construct.[121] Second strategy relates to hybridizing carbon allotropes with nanoscale VO_x. In particular, graphene as a novel carbon material has been extensively used for producing composite electrode materials with improved Li storage performance, benefiting from the well-defined nanostructure, high specific surface area and high electrical conductivity.[122, 123] For example, graphene nanoribbon-V_2O_5,[124] VO_2(B)/rGO composite[56] and V_2O_3/rGO composite[125] have been shown to considerably improve the electrochemical properties, compared to equivalent material morphology and composition materials yet without conductive graphene support. However, the large discrepancies still present in graphene materials composition, morphology and physicochemical properties leads to composites being synthesized and tested under different conditions, making difficult the comparison and discrimination of the electrochemical performance metrics of the respective phases.

Concerning the criterion (ii) - V_2O_5, being the most stable phase among all VO_x, remains the most studied for electrochemical applications, with complex mechanisms associated with Li ion de/intercalation still remaining to elucidate. Various phase transitions have been revealed in the discharge profile through defined potential steps at around 3.4, 3.2 and 2.3 V (*vs.* Li^+/Li) corresponding to the α/ε, ε/δ, and δ/γ two-phase regions,

respectively.[110, 126] The theoretical capacity is of 294 mAh g^{-1} (accounting also for the inserted Li cations), for a two Li^+ - two electron reaction per formula unit (corresponding to $Li_2V_2O_5$). It has been reported that further intercalation of Li into V_2O_5 would lead to irreversible formation of ω-$Li_xV_2O_5$ ($2<x<3$).[127, 128]

Chan *et al.* reported chemical lithiation of V_2O_5 nanoribbons with subsequent delithiation of ω-$Li_3V_2O_5$ back to the pristine V_2O_5 nanoribbon, attributed to its ability of facile strain relaxation and phase transformation at nanoscale.[129] Concurrent to this, it has been reported recently that the deep lithiated ω-$Li_3V_2O_5$ phase can be reversibly transformed into disordered β-$Li_{0.3}V_2O_5$ phase via a two-phase reaction.[130] Both disordered structures show good stability, indicating the potential of disordered phases as electrode materials. Recently, electrochemical performance of amorphous V_2O_5 thin films (prepared by atomic layer deposition method) has been also investigated and compared to that of their crystalline counterparts.[94, 131] The amorphous V_2O_5 electrode was found to have cyclic voltammogram profiles without sharply defined peaks displayed by crystalline V_2O_5. Despite, the work detailed only on Li-cation insertion with also the working potential window not being optimized leading to major irreversible first cycle losses, with further cycling not being representative of pristine crystalline or amorphous phases.

When looking at VO_x in lower oxidation states, VO_2 is known to exist in several polymorphs, among which the metastable VO_2(B) with a monoclinic structure being the most studied for charge storage applications.[132-135] VO_2(B) displays redox potential plateaus at 2.5−2.6 V (*vs.* Li^+/Li), high specific capacity and good stability as cathode material.[54, 136-138] The electrochemical properties of amorphous VO_2 were also reported recently and the authors found it to store more charge and at higher current densities than VO_2(B).[94] However, the attained

capacities of the amorphous electrode were already higher than expected, pointing towards other than faradaic processes at play, presumably originating from particular micro-electrode design with high surface area or possible phase impurities.

Going further down, V_2O_3 has been also extensively studied, yet the discrepancies here are even more pronounced between different studies as well as compared to theoretical predictions. For instance, Hong *et al.* studied the Li uptake into, and extraction from various metal oxides, including VO_x. The calculated capacity of V_2O_3 was 1073 mAh g^{-1}. However, the full Li uptake and reduction of V_2O_3 to metallic V^0 was not realized or seemed to be difficult to attain.[139] After a detailed analysis performed by us, we found that the reported capacity values of V_2O_3 electrode (most of the time cycled to low potentials) differ significantly, depending on structure, morphology and modification with carbon calling for better understanding of the electrochemistry of this material. Additionally, analysis of literature of V_2O_5 and VO_2 also points to the fact that electrochemical reduction of V^{3+} is hard to realize when in an oxide matrix.

And finally, regarding the criterion (iv), clearly VO_x have attracted and continue to attract interest as electrode materials not only for Li but also recently for Na, K and divalent cation storage.[50, 140, 141] High storage capacity, suitable working potential as well as power performances make VO_x potential candidates for energy storage. Yet, it is scarce that more than one VO_x (phase, valence) - carbon composites are prepared under similar conditions and their electrochemical properties are measured, compared and discussed systematically in a single publication. This makes a critical comparison and choice of the best material difficult.

In this part of work, we controllably synthesize a library of VO_x@rGO composites with different vanadium oxidation states, morphologies and

phases via similar methods and with similar carbon content and morphology. Stable and cheap V_2O_5 was selected as vanadium source, exploiting its solubility and reduction ability in acidic aqueous solutions, rendering this process easily available to others. Moreover, commercial rGO was employed as structural and electrical conduction framework.

The simple synthetic strategy allows us to conduct a systematic comparison study of the electrochemical properties for different vanadium oxide phases. Li and Na cells have been built and tested using similar cell configuration, electrolyte and mass loadings. The potential profile characteristics during the insertion/extraction of Li^+/Na^+ as well as first cycle efficiency and cycling stability were evaluated in various potential windows, and their power-rate capabilities are also reported.

2.2 Results and discussion

2.2.1 Synthesis methods

Many methods have been proposed to synthesize nano-structured VO_x including sol-gel, electrochemical deposition and solvo/hydrothermal synthesis.[142] Among them, hydrothermal synthesis is considered the easiest and most effective way to achieve nanostructured VO_x deposits on the surface of nano-carbons. However, it is still challenging to achieve a facile, cost-effective and environmentally friendly synthesis to produce VO_x/C materials with well-defined structures, pure and crystalline phases.

In this work, we used cost-effective V_2O_5 as starting material under hydrothermal and/or thermal treatment without addition of surfactant or other additives, in order to synthesize different VO_x phases supported on rGO. Only environmentally friendly acids (oxalic and citric acids) were used as reducing and capping agents.

In practice, commercial grade of V_2O_5 was initially reduced into vanadyl ions (VO^{2+}) by dissolution in aqueous medium with citric or oxalic acid. The mixture was slightly heated (~ 60 – 70 °C) to speed up the process. The complete dissolution and reduction of starting V_2O_5 is easily observed by the colour change of the solution from yellow to deep blueish. The acidic conditions obtained with citric or oxalic acid generates a V^{+IV} precursor solution, as confirmed with the Pourbaix diagram (**Figure 2.1**). Following the dissolution, rGO powder was added to the mixture or drop-impregnated by the solution to anchor the VO_X precursor on its surface. It has to be noted that the highly hydrophobic character of the rGO material makes it very difficult to be dispersed in an aqueous medium. Therefore, we added a few drops of methanol in the solution to allow a better dispersion. Finally, the precursors undergo a direct thermal treatment

(V_2O_5@rGO synthesis) or hydrothermal treatment (VO_2(B)@rGO and VO_2(AM)@rGO syntheses) followed by a mild thermal treatment (VO_2(M/B)@rGO and V_2O_3@rGO syntheses).

The mild acids (citric or oxalic) play a dual role in these syntheses. The dissolution and the reduction of commercial V_2O_5 into vanadyl ions (VO^{2+}) is obtained thanks to the acidic conditions. During the growth process of the different VO_X, the chelating effect of the acids will act as a capping/directing effect, similarly to commonly employed surfactants (CTAB, PVP, etc.). This effect allows the structuration of the VO_x into nanoparticles. More interestingly, depending on the amount of citric acid used, we were able to go from VO_x micro-rods to VO_x nanoparticles. It seems that incomplete chelation of VO_x precursors leads to rods formation while an excess of citric acid (> 3 eq. in mol) allows nanostructures formation (**Figure 2.2**). As described above, the same hydrothermal conditions produce distinct materials using citric or oxalic acid. Oxalic acid allows a rapid synthesis of VO_2(B)@rGO nanocomposite while citric acid

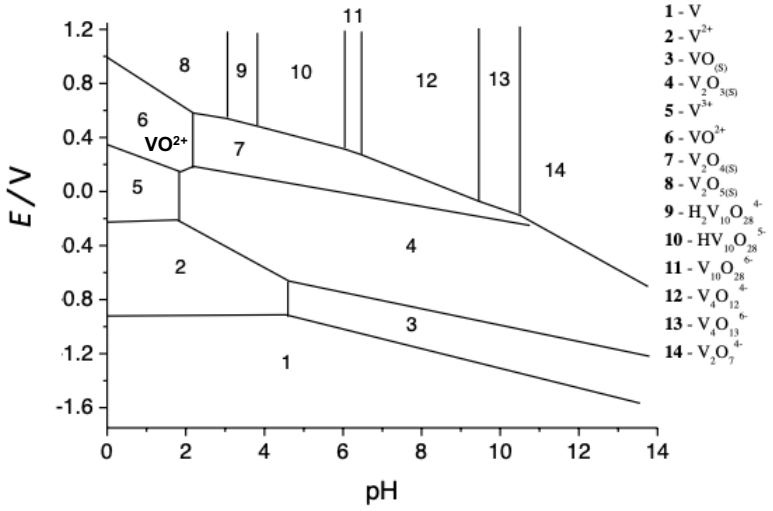

Figure 2.1 Pourbaix diagram of vanadium species in aqueous environment.[143]

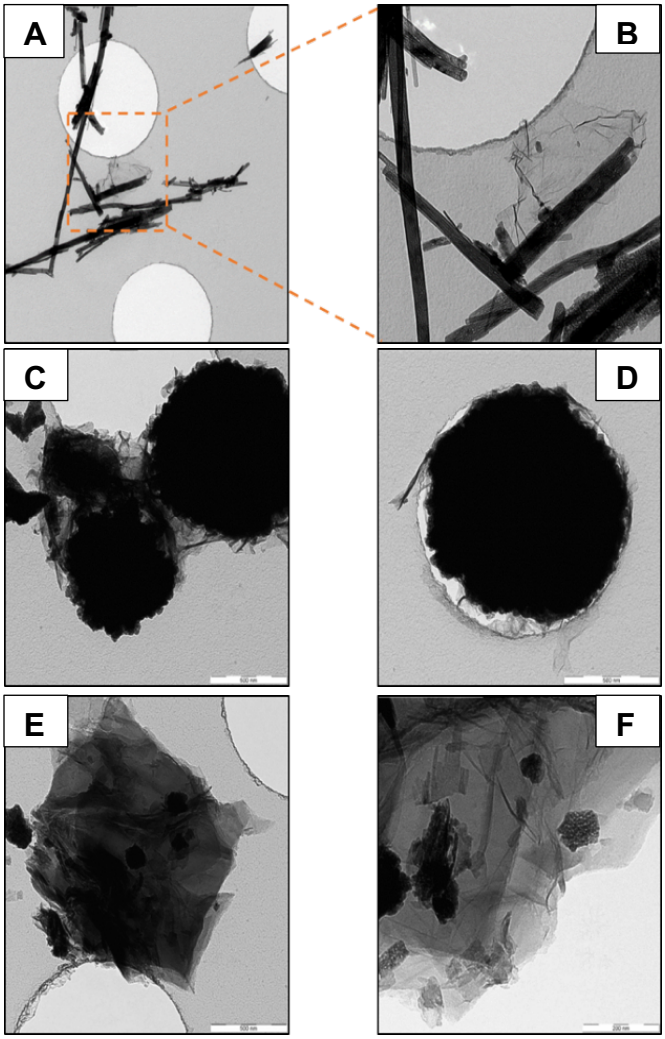

Figure 2.2 TEM images of VO_x@rGO nanostructures. From top to bottom: (A, B) VO_x@rGO with citric acid (1 – 2 eq. in mol) (C, D) VO_x@rGO with excess citric acid (> 3 eq. in mol) and (E, F) VO_x@rGO with excess citric acid and less starting V_2O_5 material.

produces an amorphous composite. This phenomenon arises from the chelating power associated to the tridentate citrate compared to the bidentate oxalate. The citrate system is probably more constraint and hence reduces the motion of vanadium ions which results in an amorphous oxide. The further thermal treatment allows the citrate to be consumed and furnishes the extra energy required for the vanadium atoms ordering in V_2O_3 or VO_2(M/B) crystals.

The synthesis methods of the VO_x@rGO library, as displayed in **Scheme 2.1**, rely on the use of cost-effective V_2O_5 as starting material, commercial rGO as support, without addition of surfactant or other additives and environmentally friendly acids (oxalic and citric acids) as reducing and capping agents. A library of VO_x nanostructures were easily obtained using this versatile and green approach and directly deposited on rGO sheets in one pot. The crystal structure, theoretical electrochemical properties and morphology of the synthesised VO_x@rGO composites are summarized in **Table 2.1** for following discussions.

2.2.2 Characterizations

Figure 2.3 groups the phases and morphologies of the synthesized VO_x@rGO composites. For comparative purposes, the XRD patterns of commercial VO_x(CM) are also given, whereas SEM images of the respective materials are shown in **Figure 2.4**. Starting rGO shows a broad diffraction peak with the associated graphite diffraction peaks absent, indicating that the used rGO is well exfoliated.[144] As depicted in **Figure 2.3**, all the synthesized composites display the broad peak of rGO as well as a series of minor peaks matching to the diffraction peaks of commercial analogues. From these we can deduce that the synthesized as well as commercial phases used are as follows: V_2O_5@rGO and V_2O_5(CM) –

orthorhombic; VO_2(B)@rGO, VO_2(CM) and VO_2(M/B)@rGO – monoclinic; and V_2O_3@rGO and V_2O_3(CM) – rhombohedral. For the VO_2(AM)@rGO, no additional peaks could be assigned, confirming its amorphous phase. The carbon content was analysed by thermogravimetric analysis and all composites have been found to contain similar amount of rGO (**Figure 2.5**, **Table 2.2**).

Figure 2.3 also illustrates the nanoscale morphology of the synthesized VO_x@rGO composites with typical VO_x particles size below 1 μm, with also uniform dispersion of VO_x nanoparticles within the rGO matrix (**Figure 2.6**). The composites have also different VO_x morphology with typically: nanoparticle for V_2O_5, cuboidal for VO_2(B) and urchin-like for the others. The CM materials have a typical particle size of over 1 μm (**Figure 2.4**). The synthesized VO_x@rGO composites have thus lower characteristic dimensions with also more uniform size distribution expected to positively impact the power-rate performances as detailed next.

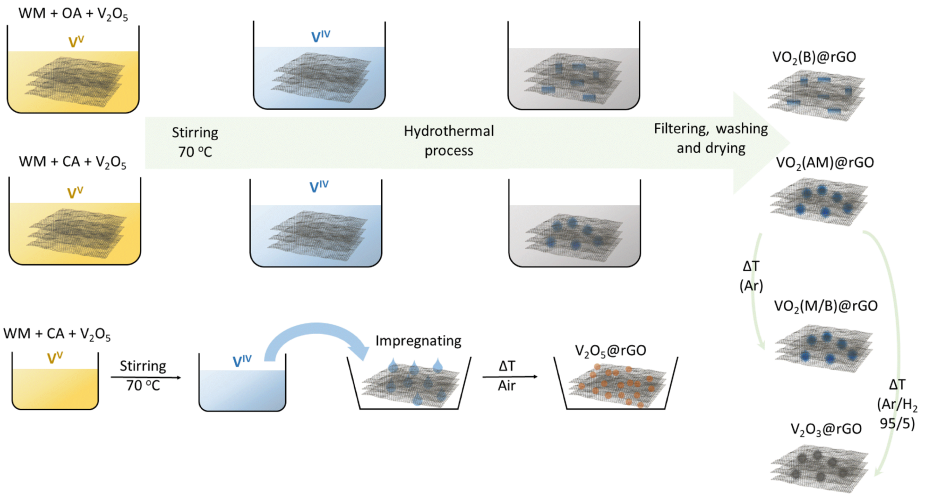

Scheme 2.1 Schematics resuming the VO_x@rGO library synthesis methods developed in this work. Legend: WM - Water/MeOH = 7/1 (v/v) mixture, CA - Citric acid, OA - Oxalic acid.

Table 2.1 The crystal structure, theoretical electrochemical properties and morphology of the synthesised VO_x@rGO composites and commercial VO_2(M) as comparison.

Sample	Oxidation state of V	Lattice parameter of VO_x	Crystal structure of VO_x	Theoretical capacity of VO_x (mAh g^{-1})	Possible redox couple	Morphology of VO_x on rGO
V_2O_5@rGO	+5	Orthorhombic a = 11.517 Å b = 3.568 Å c = 4.375 Å α = 90°	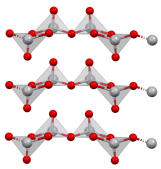	147 ~ $1Li^+$ 294 ~ $2Li^+$ 441 ~ $3Li^+$	$V^{5+/4+}$ $V^{5+/3+}$	Nanoparticle (< 100 nm)
VO_2(B)@rGO	+4	Monoclinic a = 12.03 Å b = 3.693 Å c = 6.42 Å β = 106.6°	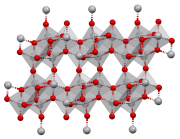	160 ~ $0.5Li^+$ 322 ~ $1Li^+$	$V^{4+/3+}$	Cuboidal nanostructure
VO_2(AM)@rGO	+4	Amorphous	Amorphous	160 ~ $0.5Li^+$ 322 ~ $1Li^+$	$V^{4+/3+}$	Urchin-like nanostructure
Commercial VO_2(M)	+4	Monoclinic a = 5.738 Å b = 4.52 Å c = 5.393 Å β = 122.7°	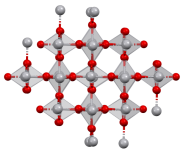	160 ~ $0.5Li^+$ 322 ~ $1Li^+$	$V^{4+/3+}$	Particle (> 1 μm)
VO_2(M/B)@rGO	+4	Mixture of VO_2(M) and VO_2(B)	Mixture of VO_2(M) and VO_2(B)	160 ~ $0.5Li^+$ 322 ~ $1Li^+$	$V^{4+/3+}$	Urchin-like nanostructure
V_2O_3@rGO	+3	Rhombohedral a = 4.952 Å c = 14.002 Å α= 120°	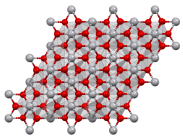	356 ~ $2Li^+$ 1070 ~ $6Li^+$	$V^{3+/2+}$ $V^{3+/0}$	Urchin-like nanostructure

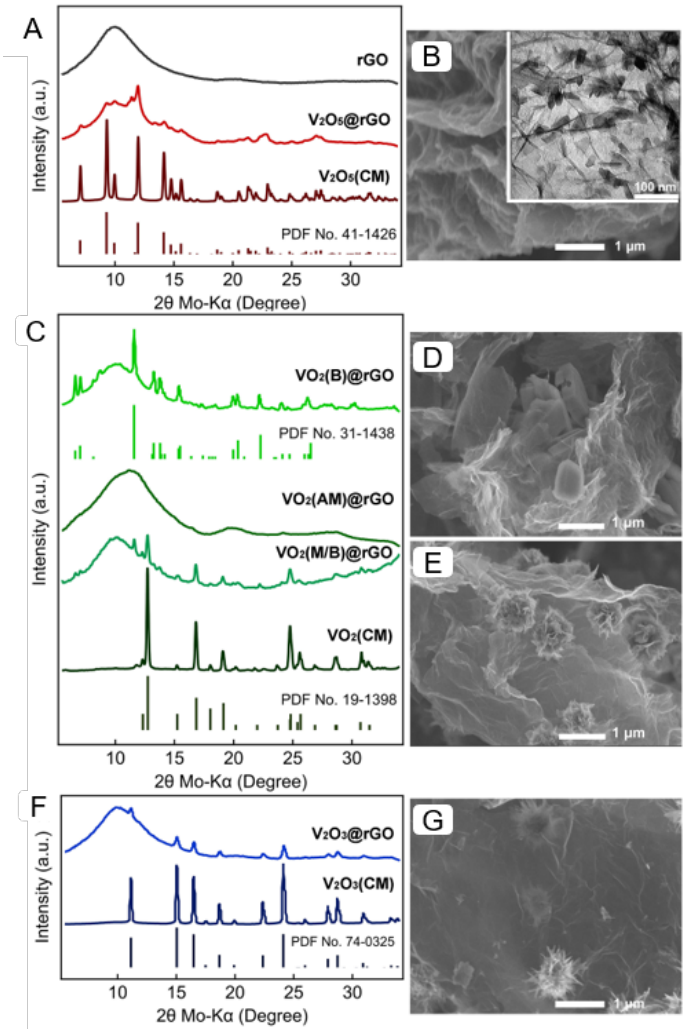

Figure 2.3 XRD patterns of (A) rGO, V_2O_5@rGO and V_2O_5(CM), (C) VO_2@rGO composites and VO_2(CM) and (F) V_2O_3@rGO and V_2O_3(CM); SEM images of (B) V_2O_5@rGO with an inset of TEM image, (D) VO_2(B)@rGO, (E) VO_2(AM)@rGO and (G) V_2O_3@rGO.

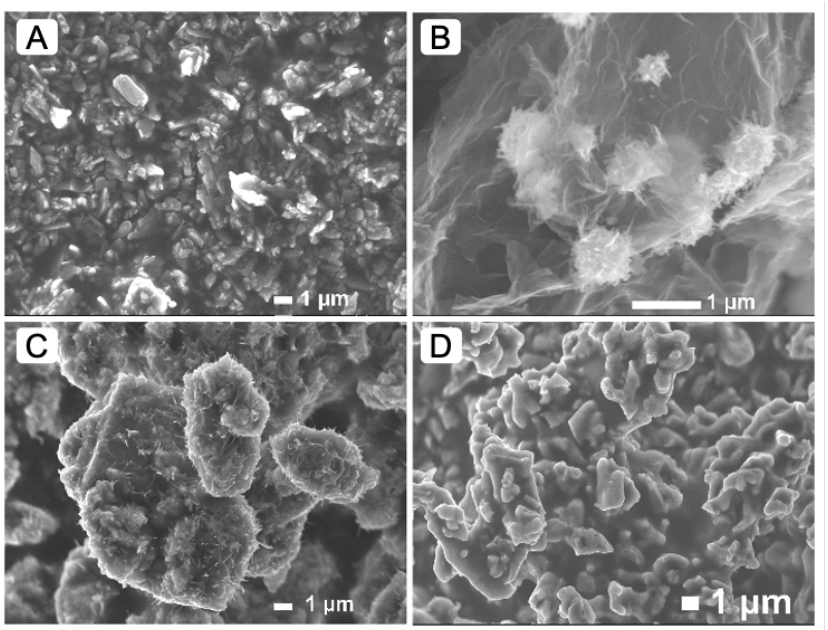

Figure 2.4 SEM images of (A) V_2O_5(CM), (B) VO_2(M/B)@rGO, (C) VO_2(CM) and (D) V_2O_3(CM).

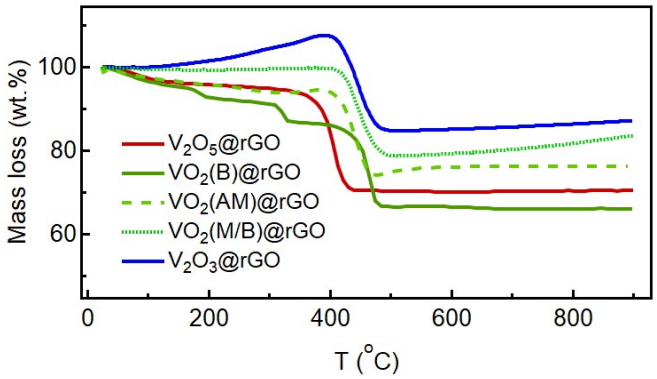

Figure 2.5 TGA curves of the synthesized materials. The measurements were performed in air. The abrupt drop of mass loss at about 150 and 320 °C for the VO_2(B)@rGO sample could be caused by a technical issue. The curve should be as smooth as those for the other samples and a similar VO_2(B)/rGO material in literature.[145]

Table 2.2 The vanadium oxide content in the electrode samples including the synthesized vanadium oxide/rGO composites and the mixture of commercial vanadium oxides and super P (SP) as conductive carbon. The vanadium oxide content in the vanadium oxide/rGO composites was estimated based on TGA data (**Figure 3.5**), considering that the mass change is from oxidation of vanadium to V_2O_5 and rGO totally oxidized to CO_2 gas without residue. The equations can be built as follows: $M(VO_x)+M(rGO)=M_0$; $M(V_2O_5)=M_1$ (M_0 is the starting mass and M_1 is the mass after measurement). $M(VO_x)/M_0$ can be calculated as vanadium oxide content in the vanadium oxide/rGO.

Electrode sample	**Vanadium oxide (wt%)**
V_2O_5@rGO	70.4
V_2O_5(CM)/SP	70.4
VO_2(B)@rGO	60.2
VO_2(AM)@rGO	69.5
VO_2(M/B)@rGO	76.2
VO_2(CM)/SP	69.5
V_2O_3@rGO	71.8
V_2O_3(CM)/SP	71.8

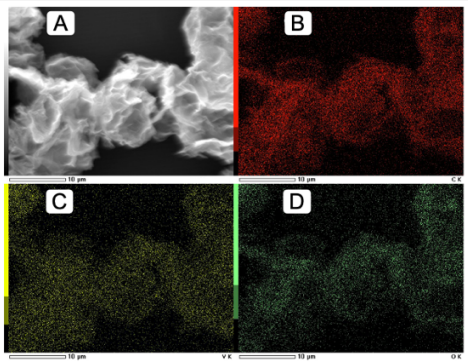

Figure 2.6 (A) SEM image of V_2O_5@rGO and the corresponding element mapping images of (B) C, (C) V and (D) O. The images further demonstrate that the V_2O_5 nanoparticles are evenly dispersed on the rGO sheets.

2.2.3 Electrochemical properties

With the morphology and the composition being established, we next entailed electrochemical performance analysis for Li as well as Na storage. The main property we screened was the optimal operation potential window to enable high-capacity charge storage while not compromising the cycling stability and coulombic efficiency.

2.2.3.1 V_2O_5@rGO electrodes for Li storage

First thing to notice here is that the V_2O_5@rGO electrodes exhibit sloping potentials *vs.* capacity charge-discharge profiles, with indistinct plateaus even during the initial cycling (**Figures 2.7A, B, C**), different from those of V_2O_5(CM) (**Figure 2.7D**) but similar to those of amorphous V_2O_5 found in literatures.[94, 146] In general, electrode materials with crystalline phase display plateaus in the charge-discharge potential profiles because of abrupt phase changes at certain amount of de/intercalated Li ion, whereas amorphous electrodes typically have sloping potential curves due to lack of evident phase transformations during insertion / extraction of Li ion.[94, 146] XRD pattern of the synthesized V_2O_5@rGO (**Figure 2.3A**) also confirms that the material has poor crystallinity, being probably a mixture of crystalline and amorphous phases. Furthermore, as shown by the TEM analysis, the particles are less than 100 nm in size with similar to flakes morphology. The material is thus characterized by surface rather than bulk redox, explaining the potential profiles similar to those of amorphous electrode materials.

Next, we targeted the cycling stability and coulombic efficiency (CE) function of the cycling potential window (**Figures 2.7E, F**). Within the working potential window of 1.0–4.1 V (*vs.* Li^+/Li) high initial capacities,

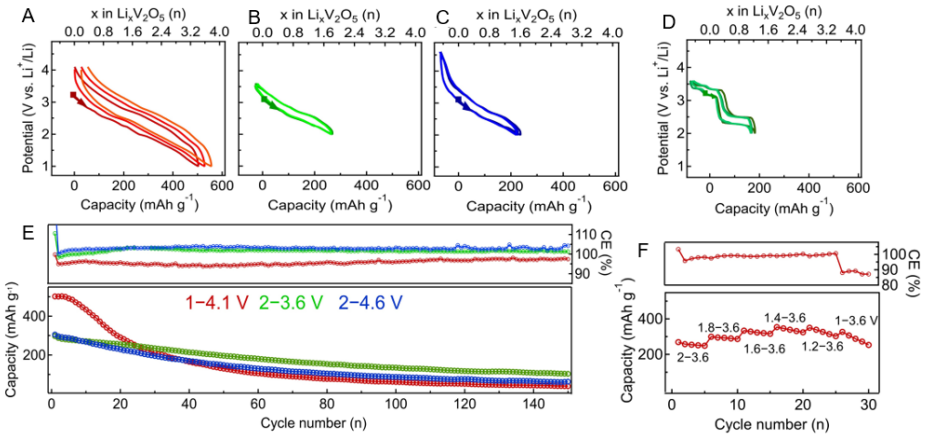

Figure 2.7 Galvanostatic potential versus gravimetric capacity (bottom axis) and Li-content (top axis) profiles for V_2O_5@rGO electrodes cycled in potential window of (A) 1.0–4.1 V, (B) 2.0–3.6 V; (C) 2.0–4.6 V; and (D) comparison with for V_2O_5(CM) electrode in the 2.0–3.6 V window. (E) Charge capacity and coulombic efficiency (CE) retention with cycling, a constant charge-discharge current density of 100 mA g^{-1} $_{(V2O5)}$. (F) Coulombic efficiency and stored charge amount chart in various potential windows at charge-discharge current density of 30 mA g^{-1} $_{(V2O5)}$.

of up to 500 mAh $g^{-1}{}_{V2O5}$ (per gram of V_2O_5 in the composite) are attained. This would correspond to 3.4 Li^+ insertion and extraction per formula unit, exceeding the typical 3 Li^+ insertion (ω-$Li_3V_2O_5$). This has also been observed by others and could be explained by additional capacitive contribution by the high surface area electrodes (summed up contribution rGO and V_2O_5).[147-149] The capacitive storage contribution of rGO was thus tested (**Figure 2.8**). Within the cycling window of 1.0–4.1 V (*vs.* Li^+/Li), the rGO can store almost 55 mAh $g^{-1}{}_{rGO}$, corresponding to capacity contribution of 15 mAh g^{-1} to V_2O_5@rGO (based on the calculation considering rGO content in the composite), which still does not suffice to balance the extra capacity. This could mean the additional part of the attained capacity in V_2O_5@rGO could come from the V_2O_5 high surface

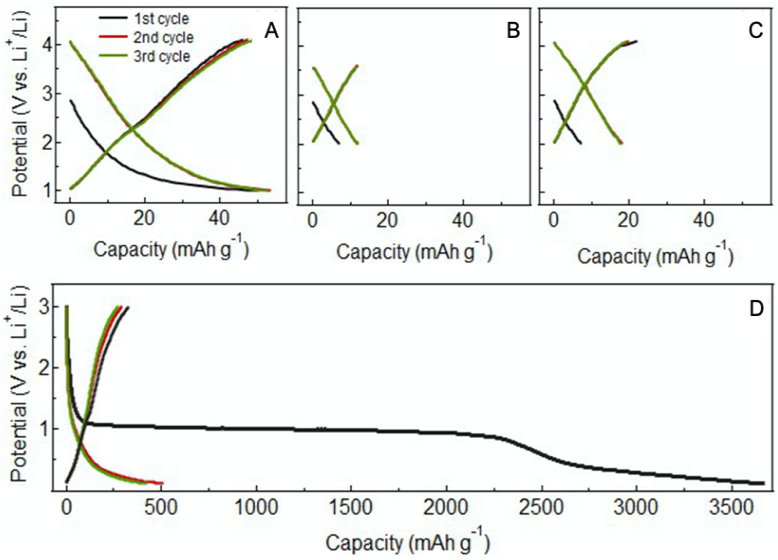

Figure 2.8 Galvanostatic charge-discharge tests for rGO. Potential vs. specific capacity profiles in potential window of (A) 1.0–4.1 V and (B) 2.0–3.6 V at 100 mA g^{-1} (rGO), and (C) 2.0–4.1 V and (D) 0.1–3.0 V at 10 mA g^{-1}(rGO).

material synthesized in this work or the onset of irreversible electrolyte decomposition at low potentials.

To further evidence the influence of deep lithiation limit on the reversibility and stability of V_2O_5@rGO, a galvanostatic charge-discharge test was performed with a gradually extending potential window: from 3.6-2.0 to 3.6–1.0 V (*vs.* Li^+/Li). As the results show in **Figure 2.7F**, the capacity indeed increases while extending potential window at the sacrifice of lower cycling stability. This could be already noticed by a decline in CE of close to 100% in the limited potential window to less than 90% when cycling in the extended potential window. This evidences that deep insertion of Li^+ can worsen the reversibility of the electrode, which could be due to the formation of irreversible phase (ω-$Li_3V_2O_5$), dissolution of V

in electrolyte under deep discharge conditions, as well as electrolyte decomposition.[126, 150, 151]

Whereas appealing charge storage metrics can be attained in this extended potential window (3.6–1.0 V *vs.* Li^+/Li), major irreversible changes are observed in the following cycles, with severe capacity loss and an average coulombic efficiency below 90% (**Figures 2.7E, F**). This is further significant of irreversible ω-phase changes during deep lithiation of V_2O_5, as also described in literature.[16,17] When limiting the potential window to 2.0–3.6 V (*vs.* Li^+/Li), the first cycle discharge capacity decreases to 269 mAh g^{-1}_{V2O5}, equivalent to 1.8 Li^+ insertion per formula unit (corresponding to $Li_{1.8}V_2O_5$). The cycling becomes highly reversible, with considerably improved capacity retention and an average coulombic efficiency of 100% (**Figure 2.7E**). When extending the working potential window to higher values, the gain in the amount of stored charge is minimal and the stability is again reduced. For example, if the upper potential is raised to 4.6 V (*vs.* Li^+/Li), similar capacities yet with faster degradation are obtained as compared to stable cycling window (2.0–3.6 V *vs.* Li^+/Li). This could be explained by increased electrolyte decomposition at the rGO or V_2O_5 surfaces.

Our results on V_2O_5@rGO are consistent with comparative and statistical analysis of nearly a hundred V_2O_5 electrodes in a recent review article.[117] Limiting lithiation at 2 Li^+ (corresponding to $Li_2V_2O_5$, equivalent to 294 mAh g^{-1}) could be favourable for V_2O_5 electrode to deliver decent capacity with good cycling stability. Moreover, the controllable synthesis method and similar test conditions for the electrodes make comparisons reliable and straightforward. Additionally, we take capacitive effects into consideration when the electrochemical performances of the nanoscale V_2O_5 are evaluated.

2.2.3.2 VO_2@rGO electrodes for Li storage

Similar methodology was applied to VO_2 (B) and (AM) phases and they show some similarities in capacity value and cycling trends, as resumed in **Figure 2.9**. When tested in the window of 1.0–4.1 V (*vs.* Li^+/Li), the electrodes delivered initial capacities of approximately 400 mAh g^{-1}_{VO2} with reversible capacities of around 300 mAh g^{-1}_{VO2}. This is nearly the theoretical value (323 mAh g^{-1}), corresponding to 1 Li^+ transfer per formula unit. The irreversible part could be ascribed to the side-reaction between the electrode and electrolyte at first cycle.[152] With fluctuations during the 40 cycles, the capacity decreased drastically in the following cycles. Gradual capacity loss is also detected when the working potential window is extended to 2.0–4.6 V (*vs.* Li^+/Li), resulting from decomposition of electrolyte. Only the electrode measured in the potential window of 2.0–3.6 V (*vs.* Li^+/Li) displayed excellent cycling stability and CE, with high capacity retention (over 150 cycles) of 96% and 67% for VO_2(B)@rGO and VO_2(AM)@rGO, respectively.

Whereas the cycling stability function of redox potential window dependence seems to be similar between both, VO_2(B)@rGO and VO_2(AM)@rGO electrodes, different potential profiles function of composition are obtained. The good crystallinity of the synthesized VO_2(B)@rGO results in clearly defined Li^+ insertion and extraction plateau at around 2.6 V (*vs.* Li^+/Li), in agreement with previous reports.[56, 137] In contrast, the VO_2(AM)@rGO electrode potential profile mainly shows a sloping features, consistent with the amorphous nature of the electrode, namely no distinctive transformation of crystalline structures during Li^+ insertion/extraction.[94, 146] The disordered framework of the amorphous materials can facilitate ionic diffusion and charge storage, which could

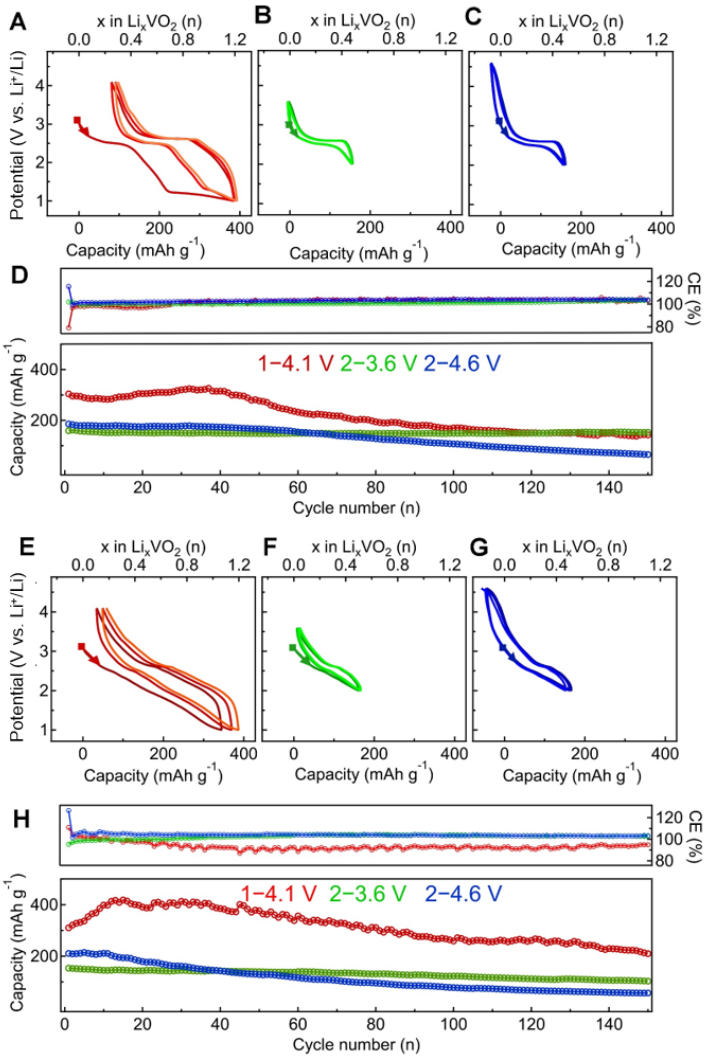

Figure 2.9 Galvanostatic charge-discharge tests at 100 mA g^{-1} $_{(VO2)}$. Potential *vs.* specific capacity and Li content profiles in potential window of (A) 1.0–4.1 V, (B) 2.0–3.6 V and (C) 2.0–4.6 V and (D) charge capacity and CE *vs.* cycle number, cycling performance for VO_2(B)@rGO, and the profiles in the window of (E) 1.0–4.1 V, (F) 2.0–3.6 V and (G) 2.0–4.6 V and (H) the cycling performance for VO_2(AM)@rGO.

explain why VO_2(AM)@rGO delivers an average charge storage capacity of 317 mAh g^{-1}_{VO2} (almost 1 Li^+ extraction) in the wide window of 1.0–4.1 V (vs. Li^+/Li).[93, 153]

To further get insight into the electrochemical behaviour differences between the VO_2(B)@rGO and VO_2(AM)@rGO, the electrodes were galvanostatically cycled at low current density of 10 mA g^{-1} in the stable cycling potential window (of 2.0–3.6 V *vs.* Li^+/Li). The potential vs. specific capacity and dQ/dV *vs.* V profiles of all tested phases, including also VO_2(M/B)@rGO and VO_2(CM) are shown in **Figure 2.10**. As also pointed above, VO_2(B)@rGO and VO_2(AM)@rGO electrodes were found to exhibit similar capacity (220 mAh g^{-1}_{VO2} corresponding to 0.7 Li^+ transfer) and first cycle reversibility (86%). Yet only VO_2(B)@rGO displays a noticeable reduction and oxidation plateau around 2.6 V (vs. Li^+/Li). This is also evidenced by the intense pair of peaks in the corresponding dQ/dV *vs.* V profile, due to the phase transition of VO_2(B) during Li^+ insertion and extraction.[137]

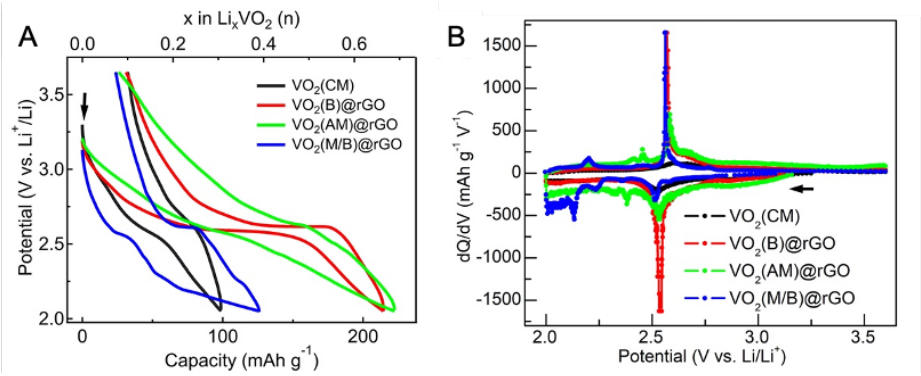

Figure 2.10 Comparison of galvanostatic charge-discharge performance at 10 mA $g^{-1}_{(VO2)}$ at the first cycle for VO_2(B)@rGO and VO_2(AM)@rGO. (A) Potential *vs.* specific capacity and (B) dQ/dV *vs.* V profiles.

The additional peaks in the dQ/dV *vs.* V profile for VO_2(AM)@rGO electrode are consistent with the literature and are characteristic of redox processes of low-valent vanadium oxides during Li^+ insertion into and extraction from VO_2(AM).[57, 154] The M-phase VO_2(CM) electrode shows poor Li^+ insertion and extraction with also low capacities attained, which suggests poor electrochemical activity, as it is also the case for VO_2(M/B)@rGO. Prepared through post thermal treatment of VO_2(AM)@rGO, VO_2(M/B)@rGO has inherited the morphology but becomes crystalline with both M phase and B phase present. It can be thus stated that the amorphous and B-phase VO_2 are more suitable as electrode materials for LIBs, compared to their M-phase counterpart.

To summarize, when cut-off potential limits down to 1 V, all the V_2O_5@rGO and VO_2@rGO electrodes suffer from poor cycling stability, with ca. 3.4 and 1 Li^+ insertion per formula unit at first discharge, respectively. The lowest attainable valence of vanadium is thus roughly V^{3+}. Deep Li^+ insertion into V_2O_5 and VO_2 is also found to lead to irreversible or unstable phases. Additionally, there might exist barriers to further electrochemical reduction of vanadium to the lower valence. On the contrary, the electrodes show enhanced cycling performance in the narrow window of 2.0–3.6 V (*vs.* Li^+/Li), with less Li^+ insertion, of *ca.* 1.8 and 0.5 Li^+ for V_2O_5@rGO and VO_2@rGO, respectively. Whereas it has been already reported that insertion of more than 2 Li^+ into V_2O_5 could form irreversible phases (ω-$Li_xV_2O_5$), phase reversibility of deep Li^+ insertion into VO_2 remains scarcely studied.

2.2.3.3 V_2O_3@rGO electrodes for Li storage

Finally, we also analysed and report here the electrochemistry of the V_2O_3@rGO with rhombohedral crystalline phase. To be mentioned

beforehand that the reported capacity values of V_2O_3 differ significantly in literature, depending on structure, morphology and modification with carbon. For example, V_2O_3-rGO has been reported to deliver first discharge capacity of 1400 mAh g^{-1} in the potential window of 0–3 V (*vs.* Li^+/Li) at 70 mA g^{-1}, with reversible capacity of 830 mAh g^{-1}.[120] Only 80 mAh g^{-1} was obtained by V_2O_3 nanorods in the same potential window at 100 mA g^{-1}.[155] Furthermore, as mentioned in the introductory part, Hong and co-workers calculated the Li storage capacity of V_2O_3 being as high 1073 mAh g^{-1}, when considering the heterogeneous reaction of V_2O_3 being reduced to V° and the formation of V/Li_2O nanocomposites phases. However, the practical full Li uptake could not be attained.[139]

Following the developed rationale for V_2O_5 and VO_2 electrodes, we started by testing the electrochemical activity of V_2O_3@rGO in various potential windows. The results were unexpectedly different from V_2O_5 and VO_2 counterparts. First, when cycled in the potential window of 2.0–4.1 V (*vs.* Li^+/Li) at low current density of 10 mA g^{-1}, a very low capacity of 38 mAh g^{-1}_{V2O3} was attained (**Figure 2.11**). Complementary measurements on pure rGO electrodes (**Figures 2.8 and 2.12**) show that this capacity originates mainly from the capacitive charge storage at V_2O_3@rGO surface, with thus little contribution from redox of V_2O_3 in this potential window. This corroborates with the findings on V_2O_5 and VO_2 electrodes since the oxidation states attained, even when deep-cycled, were still above V^{3+}, signifying that further reduction of V_2O_3 would take place at lower potentials.

In an attempt to understand the absence of electrochemical activity of the synthesized V_2O_3@rGO composite, we have prepared electrodes without rGO, by investigating the behaviour of V_2O_3(CM)/SP electrode (refer to **Table 2.2** and Experimental Section for details). Slow galvanostatic cycling (10 mA g^{-1}_{V2O3}, 0.1–3.0 V *vs.* Li^+/Li) combined with

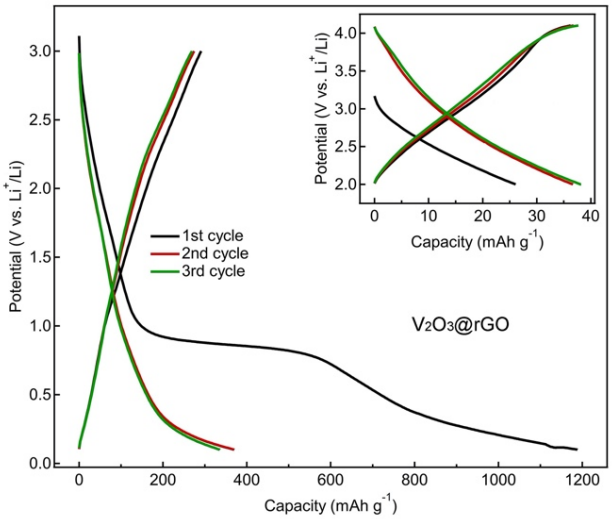

Figure 2.11 Galvanostatic charge-discharge profiles for V_2O_3@rGO electrode in potential window of 0.1–3.0 V (*vs.* Li^+/Li) at 10 mA g^{-1} $_{(V2O3)}$. Inset shows the 2.0–4.1 V region with stored charge attributed to combined capacitive charge storage of rGO and V_2O_3 nanocomposite.

ex-situ XRD was applied (**Figure 2.13**). The charge-discharge profile resembles the V_2O_3@rGO composite with the onset of electrolyte decomposition at 0.8 V and an extended discharge (reduction) capacity. The reversibility is poor, below 20%. The minor response around 2.4 V is attributed to partial V_2O_3 oxidation during handling, and correspondingly electrochemical activity. The extended tail beyond the primary SEI formation region, below 0.6 V, could be still assigned to conversion or insertion reactions and this was probed via ex-situ XRD (**Figure 2.13b**). No phase change was observed after deep-lithiation and subsequent polarizing to 3 V. A conversion reaction can be thus certainly excluded as no new phases or products (such as metallic V^0, Li_2O or Li_xV-alloys) were

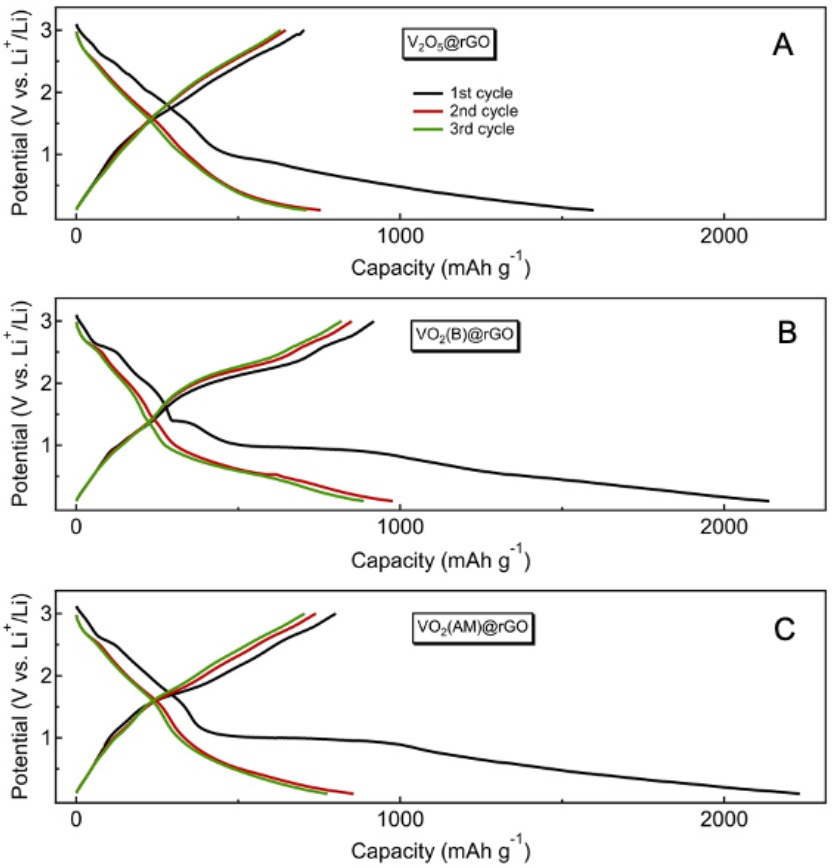

Figure 2.12 Galvanostatic charge-discharge tests in potential window of 0.1−3.0 V (vs. Li^+/Li) at 10 mA g^{-1} (VO_x). Potential vs. specific capacity profiles for (A) V_2O_5@rGO, (B) VO_2(B)@rGO and (C) VO_2(AM)@rGO. For comparison purposes, charge-discharge tests have also been performed for V_2O_5@rGO, VO_2(B)@rGO and VO_2(AM)@rGO in the low potential window of 0.1−3.0 V (vs. Li^+/Li) at 10 mA g^{-1} (VO_x). Their potential profiles show similar characteristics to those of V_2O_3@rGO, whereas the reversible capacities are more than double of that of their V_2O_3 counterpart. This implies that V_2O_3 is less electrochemically active than those with higher oxidation state. Specifically, it is sluggish for VO_x to form products with valence of vanadium lower than V^{3+} via deep Li uptake (lithiation).

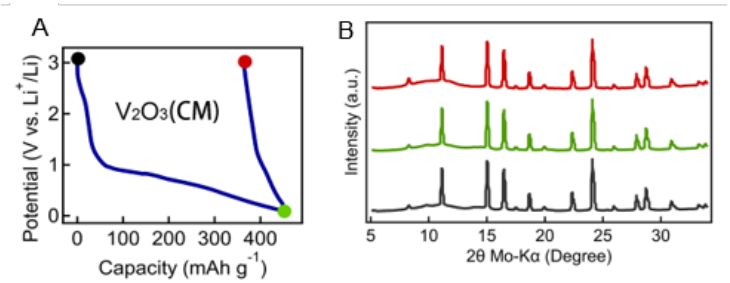

Figure 2.13 (A) potential *vs.* specific capacity profiles for V_2O_3(CM)/SP in potential window of 0.1–3.0 V (*vs.* Li^+/Li) at 10 mA g^{-1} $_{(V2O3)}$ and (B) corresponding ex-situ XRD patterns before cycling (black), after discharging to 0.1 V (green) and re-charging to 3.0 V (red).

detected. More intriguing however, is that no additional peaks, neither peak shift could be detected, with the XRD pattern being identical between the pristine - deeply discharged - re-charged electrode. This implies that the rhombohedral-phase V_2O_3 synthesized and studied in this work is electrochemically inert. In other words, the electrochemical reduction of V^{3+} to lower valence states is hindered requiring further investigation to understand whether this peculiar behaviour is thermodynamically or kinetically limited.

2.2.3.4 Power-rate performances of VO_x@rGO electrodes for Li storage

With the electrochemical activity and stability conditions established, we further studied and compared the power-rate performances of the synthesized electrode materials with similar mass loading, cell assembly and test conditions (refer to Experimental Section for details). The results are summarized in **Figure 2.14**. All commercial powder based electrodes display poor rate performances. Of all, VO_2(CM) additionally shows poor material utilization even at low current density. In turn, V_2O_5 based electrodes all show high capacities at low rate and while the CM electrodes

fail in delivering high power performances. The synthesized here V_2O_5@rGO shows excellent power rate capability among all electrodes, with nearly 43% of the capacity (304 mAh g^{-1}_{V2O5}) retained at a current density of 500 mA g^{-1}_{V2O5} (equivalent of 5C rate).

Similar performance trends are found of VO_2@rGO composites. The results also show that (B) and (AM) phases of VO_2@rGO outperform V_2O_5@rGO in terms of capacity retention with applied current density. Whereas the low-rate capacity for V_2O_5 is higher, VO_2 electrodes display better capacity retention: 61% for VO_2(B)@rGO and 59% for VO_2(AM)@rGO at 5C rate. The amorphous VO_2@rGO electrode is competitive in rate capability but not superior to VO_2(B)@rGO phase

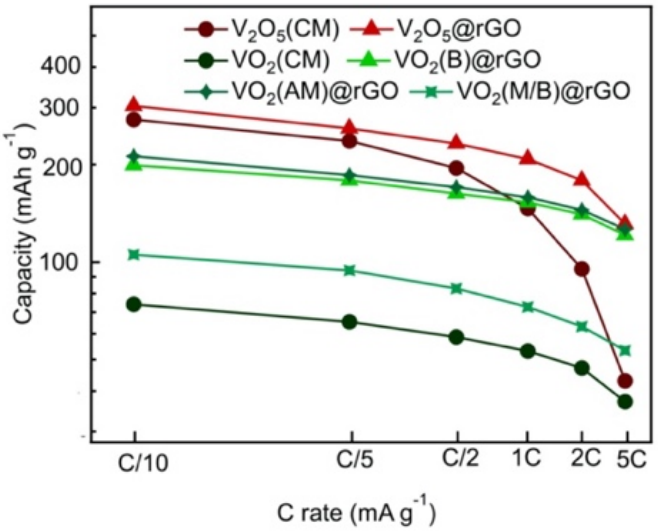

Figure 2.14 Rate capability of the V_2O_5 and VO_2 electrode materials in the potential window of 2.0–3.6 V (vs. Li^+/Li). (C=100 mA $g^{-1}_{(VOx)}$)

counterpart, indicating power-rate performance is affected by nanostructuration and rGO charge transporter rather than phase kinetics. The general behaviour of the presented power-rate performances can be clearly explained by the fact that the Li^+ and electron transport distances are significantly shortened in the synthesized rGO nanocomposites, resulting in improved electrode kinetics and charge transfer.

2.2.3.5 VO_x@rGO electrodes for Na storage

Lastly, Na storage properties have also been evaluated and the main results summarized in **Figure 2.15**. The electrochemical behaviour for Na storage was found to differ significantly as compared to Li storage. It can be first observed that all synthesized and analysed phases (V_2O_5@rGO, VO_2(B)@rGO and VO_2(AM)@rGO) have sloped potential-capacity profiles. The absence of noticeable potential plateau in the profiles of VO_2(B)@rGO could indicate the difficulty of Na^+ insertion into the crystalline VO_2(B). This can also explain lower Na storage capacities and higher electrode polarization (hysteresis). In turn, the V_2O_5@rGO with poor crystallinity and the amorphous VO_2(AM)@rGO can deliver comparable initial capacities to those for Li cells. Over 50 cycles, there is slight capacity loss for all electrodes, but retained capacities are still higher than those for bulk commercial electrode materials when tested in Na cells (**Figure 2.16**). The poor rate capability and deficient Na storage capacity for commercial counterparts reflect the positive effect of nanostructuring with rGO scaffold on electrochemical performance of the vanadium oxides.

Besides charge storage via guest species intercalation into ordered, crystalline structure of electrode materials, there exist capacitive storage mechanisms contributing to the overall charge storage capacity simultaneously. The capacitive storage mostly can be reflected by sloping

feature of potential profiles. It has been reported that the capacitive contribution of VO_2(B) electrode in Na cells plays the dominant role in the charge storage process, accounting for 76% of the total storage capacity.[56] In some previous studies, VO_x electrodes have been also found to exhibit potential profiles without noticeable plateaus and suffer from fast capacity decay.[93, 156, 157] This could be attributed to larger size of Na^+ than Li^+ resulting in sluggish electrochemical reaction and gradual structure collapse during Na^+ insertion / extraction processes for electrode materials.

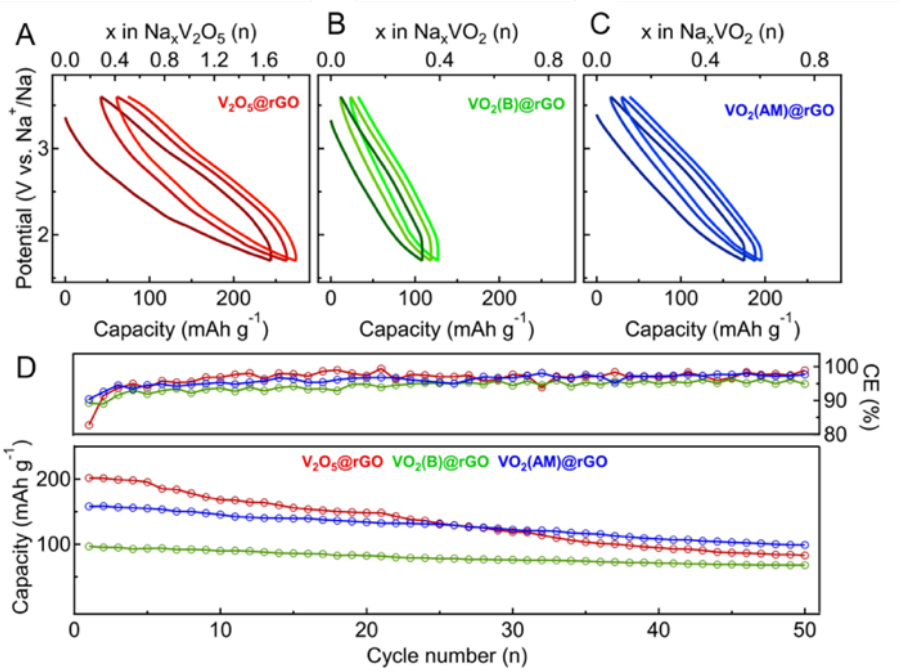

Figure 2.15 Sodium storage performances of V_2O_5@rGO and VO_2@rGO composite electrodes cycled at a current density of 10 mA g^{-1} $_{(VOx)}$. Potential *vs.* specific capacity and Na content profiles for (A) V_2O_5@rGO, (B) VO_2(B)@rGO and (C) VO_2(AM)@rGO in potential window of 1.7−3.6 V (*vs.* Na^+/Na), and (d) cycling performance.

Amorphous materials have been considered as promising electrode candidates for alkali storage, because more open framework arising from disordered arrangement of atoms could potentially facilitate ionic diffusion. As shown above, VO_2(AM)@rGO shows similar Li storage performance to VO_2(B)@rGO, in terms of capacity values and rate capability (**Figures 2.9 and 2.14**). However, the amorphous phase outperforms the crystalline one when applied for Na storage. This indicates that amorphous electrode materials could be competitive to accommodate Na^+ and other alkali ion with larger ionic radius.

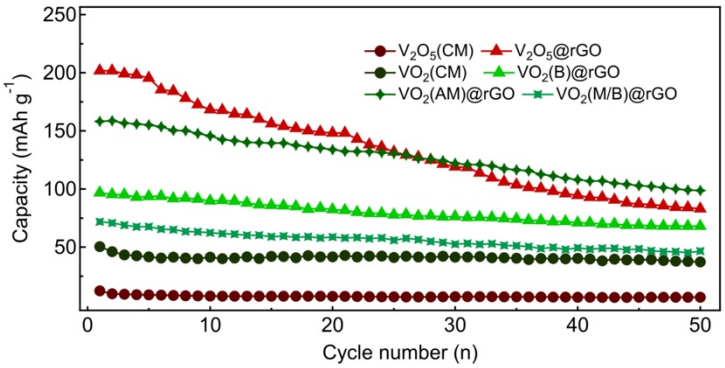

Figure 2.16 Cycling performance of V_2O_5 and VO_2 electrode materials for SIBs.

2.2.4 Further discussion

With the phase structure, morphology and in-depth electrochemical properties of the VO_x@rGO composites analysed and compared, a summary is made to have a broader picture on the influence parameters on their electrochemical behaviours as follows.

Among the V_2O_5@rGO and VO_2@rGO electrodes, the V_2O_5@rGO has the high oxidation state of vanadium and can deliver more capacity for both LIBs and SIBs. Furthermore, the open layered crystal structure of

V_2O_5 facilitate ion diffusion and even commercial V_2O_5 in micron particle size exhibits the similar high capacity of around 300 mAh g^{-1} to V_2O_5@rGO, yet only for Li storage at low current density. Nanostructured V_2O_5@rGO electrode shows improved power rate capability but the long-term cycling stability is unsatisfactory even tested in a narrow potential window. The nanoparticle (< 100 nm) morphology of V_2O_5 on rGO boosts electrolyte contacting area and thus efficient electrochemical redox on one hand. On the other hand, it can cause the acceleration in vanadium dissolution in electrolyte, resulting in poor cycling performance. Carbon coating directly on V_2O_5 particle could be an effective way to tackle the issue.

Although those VO_2@rGO with middle oxidation state of vanadium possess lower theoretical capacity, the cycling stability is greatly improved. To note that the VO_2(M/B)@rGO and commercial M-phase VO_2 lack electrochemical activity, which can be explained by the limited ion diffusion pathways in the crystal structure of M-phase VO_2. In contrast, the B-phase and amorphous VO_2 can deliver descent capacity. The superior Na storage performance for amorphous one can be attributed to its the disordered and open structure to accommodate large ions. From this point of view, it can be seen that it is intrinsic phase structure to basically define the performance of electrode materials for charge storage. Meanwhile, morphology has an influence on active material utilization and power rate capability of the electrode materials. The excellent power rate capability of VO_2(B)@rGO and VO_2(AM)@rGO electrodes for Li storage can be attributed to the nanostructured VO_2 on rGO matrix to lower the ion diffusion length and increase the electrical conductivity.

In theory, V_2O_3 as electrode material can be electrochemically reduced to lower oxidation state of V^{2+} or even metallic V^0. However, practically in this study, reduction of V_2O_3@rGO and commercial V_2O_3 seems to be

unfavourable. It is also found that reduction of V_2O_5@rGO and VO_2@rGO electrodes to lower than V^{3+} hardly occur, which indicates the difficulty in reaching at lower than V^{3+} by lithiation of VO_x produced in this work. Although very high capacity can be obtained for all the VO_x@rGO electrodes in the low potential window of 0.1–3 V (vs. Li^+/Li). We assume that most of it could be contributed from capacitance due to the large surface area in those nanostructured VO_x@rGO.

Compared with this type of electrode materials in literature, the performance of the VO_x@rGO electrode in this work is not among the best ones, probably resulting from the high mass loading (4–5 mg composite powder per square-cm) of the powder electrode. However, the controllable, cost-effective and green synthesis methods make large-scale production of those materials possible. More importantly, relying on the similar synthesis process, similar carbon content and same coin cell configuration and test conditions, the comparative analyses are more critical and easier than those in review articles by comparing the materials prepared and evaluated via various procedures.

2.3 Conclusions and significance of this work

We developed a cost-effective, versatile and environmentally friendly synthetic approach for the decoration of rGO carbon with various VO_x nanostructures. The synthesis proceeds through green methods, relies on easily available precursors with high yield and limited waste generation thus making the methods proposed suitable for large-scale applications. This allowed us to synthesize a rich library of VO_x@rGO electrode materials making possible a systematic and critical comparison of their electrochemical performances. Both Li and Na ion storage properties were analysed.

Whereas precise quantitative guidelines will be dependent on specific composition, morphology and electrode formulation, the important findings of this work, that could be further generalized to other VO_x battery electrode composites, are: (i) the limited potential window for high capacity retention and coulombic efficiency. A balance needs to be found between the amount of stored charge and stable cycling; (ii) V_2O_5 can deliver more charge storage, while (B) and (AM) VO_2 phases are better choices as highly reversible and cycling stable cathodes; (iii) Power performances essentially depend on nanostructuration as well as carbon content and interfacing, while being minimally affected by the VO_x composition and crystal phase; (iv) Amorphous VO_x phases are more suitable for Na storage, worthy of further investigation and optimisation; (v) Electrochemical reduction of V^{3+} seems to be unfavourable in solid-phase.

Similar to those reviews in literature but in a more critical and straightforward way, this work made a comprehensive and comparative study on the electrochemical behaviour of VO_x in different oxidation states, crystalline phases and morphologies. That benefits from the facile and

controllable synthesis methods to produce the various samples as well as the same electrochemical test conditions. Basically, the intrinsic phase structure determines the electrochemical activity, while composite and morphology designs can improve the performance of the electrodes. Meanwhile, the consideration of capacitance contribution from nanostructured carbon matrix and active material can assist in better understanding the electrochemical behaviours.

It has also been found that potential window for electrochemical tests can significantly affect the properties of those electrodes, which should be taken into great consideration in future investigation. In addition, efforts are needed to unravel the origin of hardly reduction of the V_2O_3 electrode materials in this work.

Overall, this work gives an exhaustive experimental overview on the electrochemistry of vanadium oxides composites and may be used as a baseline for future developments for this class of next-generation battery materials.

2.4 Experimental section

2.4.1 Impregnation synthesis of V_2O_5@rGO

The precursor solution was prepared by mixing V_2O_5 (91.5 mg, 99.9%, Alfa Aesar) and citric acid monohydrate (644 mg, GR for analysis, Merck) in 3.5 mL of Milli-Q water under vigorous stirring at 70 °C for 30 min (until the colour of the solution changed from yellow (V^{5+}) to blue (V^{4+})). rGO (35 mg, Graphene N002-PDR, Angstron Materials) was deposited into a crucible and impregnated with the solution to which 0.5 mL of methanol was added to improve wettability. After vacuum drying at 50 °C for 15 min, the powder was heated to 600 °C for one hour under Ar atmosphere. V_2O_5@rGO was finally obtained by heating the powders at 300 °C for 15 min in air.

2.4.2 Hydrothermal synthesis of VO_2(B)@rGO

VO_2(B)@rGO was synthesized using hydrothermal conditions with oxalic acid, as previously reported.[145] In a typical synthesis, 35 mg of rGO was first dispersed in 35 mL Milli-Q water under sonication for 45 min. To increase the dispersibility of the hydrophobic rGO in water, 2 mL of methanol was added to the suspension. V_2O_5 (93.5 mg) and oxalic acid dihydrate (196 mg, GR for analysis, Merck) were added to the suspension, followed by stirring at 70 °C for 45 min, until the V_2O_5 was completely dissolved. Next, the mixture was poured into a 300 mL Teflon lined stainless steel autoclave and kept at 200°C for 15 h while stirred at 200 rpm in a heating mantle. Finally, the product was vacuum-filtered through a 0.22 μm PVDF membrane and washed thoroughly with Milli-Q water and

ethanol. VO_2(B)@rGO was obtained after drying under vacuum at 50 °C for 24 h.

2.4.3 Hydrothermal synthesis of VO_2(AM)@rGO and V_2O_3@rGO

VO_2(AM)@rGO was obtained using the same protocol as VO_2(B)@rGO, except that the oxalic acid dihydrate was replaced by citric acid monohydrate (314 mg). V_2O_3@rGO was obtained by annealing VO_2(AM)@rGO at 500 °C for 2 h under reducing Ar/H_2 (5%) atmosphere. If annealed under non-reducing, pure Ar atmosphere, the VO_2(AM)@rGO became crystalline, denoted hereafter as VO_2(M/B)@rGO.

2.4.4 Materials characterizations

Thermogravimetric analysis (TGA) was performed with air as carrier gas, up to 900 °C, at a heating rate of 10 °C min^{-1} on a Mettler Toledo TGA/DSC 3^+ STAR^e System, using alumina containers. Powder X-ray diffraction (XRD) was employed to confirm the crystalline phases of the synthesized composite samples and compared to those of commercial materials: V_2O_5 (99.9%, Alfa Aesar), VO_2 (≥99%, Sigma-Aldrich) and V_2O_3 (98%, Sigma-Aldrich). The powders were introduced into 0.5 mm thin-walled glass capillaries (Hilgenberg GmbH, Germany), mounted on a goniometer head and kept at 200 mm distance from the detector. Diffractograms were collected at room temperature using a MAR345 diffractometer (MarResearch GmbH), a Mo-Kα (0.71073 Å) anode and a XENOCS focusing mirror. The obtained 2D diffractograms were azimuthally integrated using the Fit2D software and calibrated with a LaB_6 standard (NIST 660b Standard). The microstructure and morphology of the

samples were characterized by Scanning Electron Microscopy (SEM, JEOL JSM 7600F), Energy-dispersive X-ray spectroscopy (EDX, JEOL JSM 7600F) and Transmission Electron Microscope (TEM, LEO 922 OMEGA) after dispersing these on holey carbon film on copper grids.

2.4.5 Electrochemical cell assembly and measurements

The working electrodes were fabricated by dry grinding the VO_x@rGO composites (90 wt%) with Poly tetra fluoroethylene (PTFE, powder, Sigma-Aldrich) as binder (10 wt%), followed by pressing certain amount of powder onto coin cell case. The typical mass loading was of approximately 4–5 mg composite powder per square-cm. The commercial VO_x samples, denoted hereafter as VO_x(CM), were ball milled with super P carbon (SP) as conductive agent at 300 rpm for 2 h under Ar, followed by dry grinding with PTFE binder. For comparison purposes, the carbon content (approximately 30 wt.%) was kept similar to the VO_x@rGO counterparts, as listed in **Table 2.2**. Besides, rGO electrodes were also prepared by grinding with PTFE (27.6 wt.%).

The electrochemical characterization was performed in half-cells (CR2032 coin cell format) with either metallic Li or Na as counter and reference electrode and one sheet of glassfibre (Whatman, GF/D) separator. The assembly was performed in an Ar filled glove box (less than 0.1 ppm in water and oxygen). For Li half-cells, the electrolyte solution was made by dissolving 1 M $LiPF_6$ in a 1:1 (v:v) mixture of ethylene carbonate (EC) and dimethyl carbonate (DMC). Galvanostatic charge-discharge tests were carried out with various current densities and potential window conditions using Neware battery test system at ambient temperature. For Na half-cells, $NaClO_4$ dissolved in a 1:1 (v:v) mixture of EC and diethyl carbonate (DEC) containing 5 vol% fluoroethylene carbonate (FEC) was used. Galvanostatic

charge-discharge tests were performed for Na cells on Neware battery testing system at ambient temperature. Reported capacities are per gram of VO_x in the electrodes， denoted as mAh g^{-1}_{VOx}.

2.4.6 Ex-situ XRD measurement

To confirm the electrochemical inactivity of the synthesized V_2O_3 composite, the cells containing commercial V_2O_3, were first discharged to 0.1 V (vs. Li^+/Li) or subsequently re-charged to 3.0 V (vs. Li^+/Li) at a current density of 10 mA $g^{-1}_{(V2O3)}$. Subsequently, the cells were disassembled in the glovebox, and the electrode powder was collected and then washed with DMC. After drying, the powder was sealed in glass capillaries for XRD analysis.

CHAPTER 3 – Exploring the Chemical Space of Metastable Fe-PO_4-F Cathode Materials for High Performance Sodium Storage

Abstract

Na and Fe make up the perfect combination for the growing demand of sustainable energy storage systems given the natural abundance and sustainability of these two building block elements. However, most Na-Fe electrode chemistries are plagued by intrinsic low energy densities with continuous ongoing efforts to solve this. Herein, the chemical space of metastable, off-stoichiometric Fe-PO_4-F materials is unraveled and found to show far improved electrochemical activity for Na storage, as compared to the amorphous or thermodynamically stable phases of equivalent composition. The metastable crystalline material of $Na_{1.2}Fe_{1.2}PO_4F_{0.6}$ delivers a reversible capacity of more than 140 mAh g^{-1} with an average discharge potential of 2.9 V (vs. Na^+/Na^0) resulting in a practical energy density of 400 Wh kg^{-1}, outperforming many developed analogues thus far, with further multiple possibilities to be explored towards improved energy storage metrics. Overall, this study unlocks the possibilities of off-stoichiometric Fe-PO_4-F cathode materials and reveals the importance to explore the often-overlooked metastable materials for energy storage.

3.1 Introduction

Polyanionic frameworks with SO_4^{2-}, PO_4^{3-} BO_3^{3-} and SiO_4^{4-} form a major stream of positive electrode material candidates for LIB and SIB.[27, 35, 48, 158] Compared to layered or disordered oxides, these typically have a higher redox potential, owing to inductive effect, as well as stable framework structure which ensures longer-term cycling stability. Additionally, the reduced safety concerns benefit also from their higher thermal stability.[158] Further energy density increase of these can be attained through substitution with lightweight and electronegative groups like F, N or OH.[27, 35] Fluorinated class of polyanionic cathode materials has thus emerged as a promising chemistry, wherein the higher electronegativity of F translates into enhanced ionic character of the bonds and correspondingly higher redox potential.[119]

Out of the respective building blocks - *i.e.*, Na^+, TM (transition metal), F^- and PO_4^{3-} - many stoichiometric compositions with promising electrochemical performances have been designed and tested thus far. These can be grouped into following main classes: $NaMPO_4$, $NaMPO_4F$, and Na_2MPO_4F (where M can be Fe, Mn, Co, V, Cr, Ni).[45, 159] With the possible polymorphism in these multiplying the possibilities here, off-stoichiometric compositions further enrich this landscape and have attracted recent attention. For instance, off-stoichiometric phosphate and sulfate compositions have been found to show better active material utilization at higher redox potentials.[160-162] The off-stoichiometric chemistries also allow for fine tuning of the composition and balance the Na content to equivalent of redox active transition metal, while allowing to lower the weight of the anion framework (for example, substituting PO_4^{3-} by F^-). With this respect, Yamada *et al.* recently reported on a peculiar

$Na_{0.6}Fe_{1.2}PO_4$ phase, which further broadened the off-stoichiometric positive electrode materials family.[107] The $Na_{0.6}Fe_{1.2}PO_4$ phase can be regarded as an Fe-rich phase (0.4 Na^+ being replaced by 0.2 Fe^{2+}) with potentially 1.2 redox electrons being available, while practically being limited to only 0.6 due to the Na^+ formula content. F doping, bringing along higher Na^+ content, could thus be regarded as a means to further increase the specific capacity of this material.

Finally, of essential relevance to developments in this work, it is important to recall that most of today's positive electrode chemistries (e.g. $Li[Co,Ni,Mn,...]O_2$, $LiFePO_4$, $Na_3V_2(PO_4)_3$, Na_2FePO_4F) are prepared and investigated in their thermodynamically stable form.[86, 163, 164] On the contrary, metastable phases are kinetically trapped phases with positive free energy above the equilibrium state, with many of these known to exhibit superior properties than their corresponding stable phases.[165] Although with moderate interest and applicability so far, these also start gaining interest in the battery materials field.[59, 100, 166-168] Tatsumisago et al. have recently summarized the state-of-art progress on glassy and metastable crystalline materials as solid electrolytes and electrode materials, aiming at emphasizing the attention on the under-explored potential of metastable materials for battery applications.[95] The metastable phases tend to have larger molar volumes(or less compact) and higher symmetry crystalline structures, favourable thus for ion conduction and have been proposed for investigation as solid electrolytes. Nonetheless, the research and application of this type of materials as cathodes for electrochemical energy storage remains rather limited while the possibilities for metastable phases might be endless, and so the electrochemical properties.

Herein, we explore the above three concepts within one class of battery materials, in which a set of chemistries based only on Na^+, Fe^{2+},

PO_4^{3-} and F^- are found to be library-level rich by tuning the stoichiometry of these building bricks while also trapping the systems outside the thermodynamic stability range. Inspired by the knowledge on reported archetypal $Na_{1+x}FePO_4F_x$ (with x=0, or 1) and $NaFeF_3$ chemistries, as well as the recently reported $Na_{0.6}Fe_{1.2}PO_4$ we developed a series of linear combinations of these with the empirical formula of $Na_{0.6+x}Fe_{1.2}PO_4F_x$ (with analysed values of x = 0, 0.2, 0.4, 0.6, 0.8 and 1).[31, 107, 169, 170] Likewise the compositional building units (the $Na_{0.6+x}Fe_{1.2}PO_4F_x$ could be regarded as a mixture of $NaFePO_4$ and $NaFeF_3$) we found the thermodynamically stable phases to be electrochemically less active and focused our interest on the intermediate synthesis phase. Altogether combined, this work uncovers the electrochemistry of five crystalline compounds based on the diverse Na-Fe-PO_4-F composition map (by changing x in $Na_{0.6+x}Fe_{1.2}PO_4F_x$); with as many as six electrochemically active materials for solely the $Na_{1.2}Fe_{1.2}PO_4F_{0.6}$ composition. Through electrochemical and analytical analyses we reveal the mechanistic rationales behind the enhanced electrochemical properties being attributed to open Na diffusion channels in the crystal structure. We also postulate that other, low-energy metastable and chemical compositions exist and can be synthesized for this class, while other compositions based on different than Fe redox centre, or PO_4^{3-} anion framework could be subsequently developed based on principles developed in this work.

3.2 Results and discussion

3.2.1 Synthesis strategy of the metastable materials in the $Na_{0.6+x}Fe_{1.2}PO_4F_x$ chemical space

Relying on the introductory rationales while focusing on the exotic Fe-rich, Na-deficient chemistry proposed by Yamada (i.e. $Na_{0.6}Fe_{1.2}PO_4$) we have undergone this extended study on mixing the six-key essential parameters of a high-performance positive electrode chemistry for SIBs (**Figure 3.1A**). The nominal composition of our study, namely the $Na_{0.6+x}Fe_{1.2}PO_4F_x$ synergistically mixes these concepts. The inclusion of F in the parent $Na_{0.6}Fe_{1.2}PO_4$ composition was designed with a two-fold interest. First, this increases the Na content with minimal penalty on the specific capacity while secondly considering the redox potential increase associated with F doping. Preliminary analysis of synthesis conditions also revealed a series of crystalline intermediate materials with superior electrochemical properties and the broad plethora of materials found have been thus characterized. These include: (i) thermodynamically stable phases, made at elevated temperature and long annealing conditions; (ii) amorphous (or non-crystalline) phase made by low temperature; as well as the (iii) intermediate metastable crystalline materials (**Figures 3.1B and 3.1C**). All the synthesised samples are listed in **Tables 3.1 and 3.2** for following discussions.

The $Na_{0.6+x}Fe_{1.2}PO_4F_x$ materials were obtained by changing the stoichiometry of precursors and annealing under same conditions (temperature and time). The amorphous, crystalline metastable and crystalline stable compounds for $Na_{1.2}Fe_{1.2}PO_4F_{0.6}$ were obtained by changing the annealing conditions (time or temperature), which can be explained by transition states in the free energy diagram (**Figure 3.1B**).

Note that other possibilities in the composition – synthesis conditions diagram may exist and remain unexplored. The synthesis design relied on careful analysis of the intermediate products in the precursor preparation and annealing processes. The starting reactants consisted in mixing the desired molar ratios of iron oxalate dehydrate ($FeC_2O_4 \cdot 2H_2O$), sodium carbonate (Na_2CO_3), ammonium dihydrophosphate ($NH_4H_2PO_4$) and sodium fluoride (NaF). These were selected so that they can react and decompose at low temperatures with all volatile, or gaseous products generation.

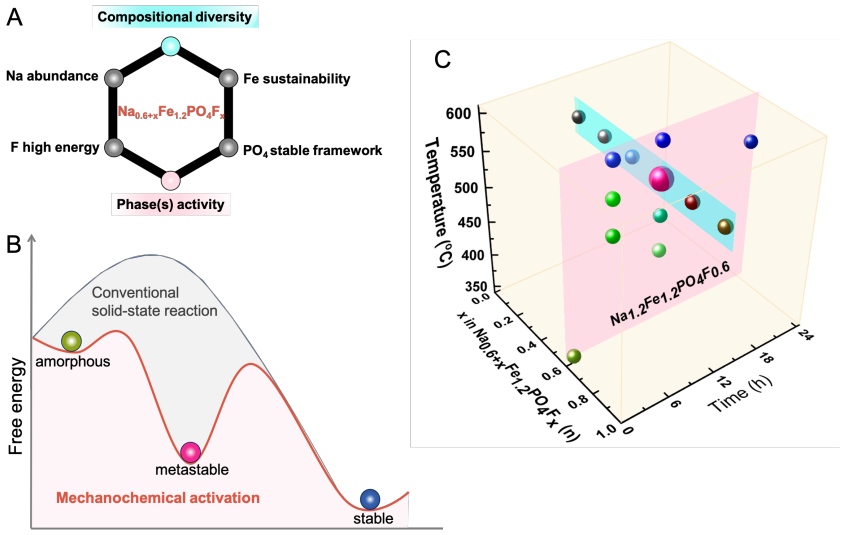

Figure 3.1 (A) A set of chemistries and advantages of $Na_{0.6+x}Fe_{1.2}PO_4F_x$ series materials. (B) Evolution of a system from an amorphous, to a metastable, finally to a state of stable equilibrium during synthesis (bullets color code corresponds to the samples in the pink plane depicted in phase-diagram of panel C). (C) Samples and composition map/diagram of studied combination in this work. The various composition samples with the change of x are within the blue plane; and the various phases for x=0.6 are contained within the pink plane.

Table 3.1 The $Na_{0.6+x}Fe_{1.2}PO_4F_x$ materials in different compositions.

Sample name / Composition	x (NaF)	Theoretical capacity (mAh g^{-1})	Annealing condition (Temperature_Time)
$Na_{0.6}Fe_{1.2}PO_4$	0	91	550 ºC_12h
$Na_{0.8}Fe_{1.2}PO_4F_{0.2}$	0.2	116	
$NaFe_{1.2}PO_4F_{0.4}$	0.4	139	
$Na_{1.2}Fe_{1.2}PO_4F_{0.6}$	0.6	160	
$Na_{1.4}Fe_{1.2}PO_4F_{0.8}$	0.8	154	
$Na_{1.6}Fe_{1.2}PO_4F$	1	148	

Table 3.2 The $Na_{1.2}Fe_{1.2}PO_4F_{0.6}$ (x=0.6) materials annealed under different temperature and time conditions

Sample name	State	Annealing condition (Temperature_Time)	Theoretical capacity (mAh g^{-1})
$Na_{1.2}Fe_{1.2}PO_4F_{0.6}$_**AM**	Amorphous	350 ºC_1h	160
$Na_{1.2}Fe_{1.2}PO_4F_{0.6}$ (Intermediates)	Intermediate	450 ºC_12h 500 ºC_6h 500 ºC_12h 550 ºC_6h	
$Na_{1.2}Fe_{1.2}PO_4F_{0.6}$_**M**	Metastable	550 ºC_12h	
$Na_{1.2}Fe_{1.2}PO_4F_{0.6}$_**S**	Stable	550 ºC_24h 600 ºC_6h 600 ºC_12h	

High-energy ball milling of the starting materials before annealing (precursors) was already found to induce major chemical and phase changes (**Figure 3.2A**) as a direct consequence of combined mechanochemical and acid-base reactions in the system. It should be noted that the mixing conditions of the starting materials were found to significantly affect the precursors composition with further impact on the final products (for example, manual grinding or low-energy planetary ball

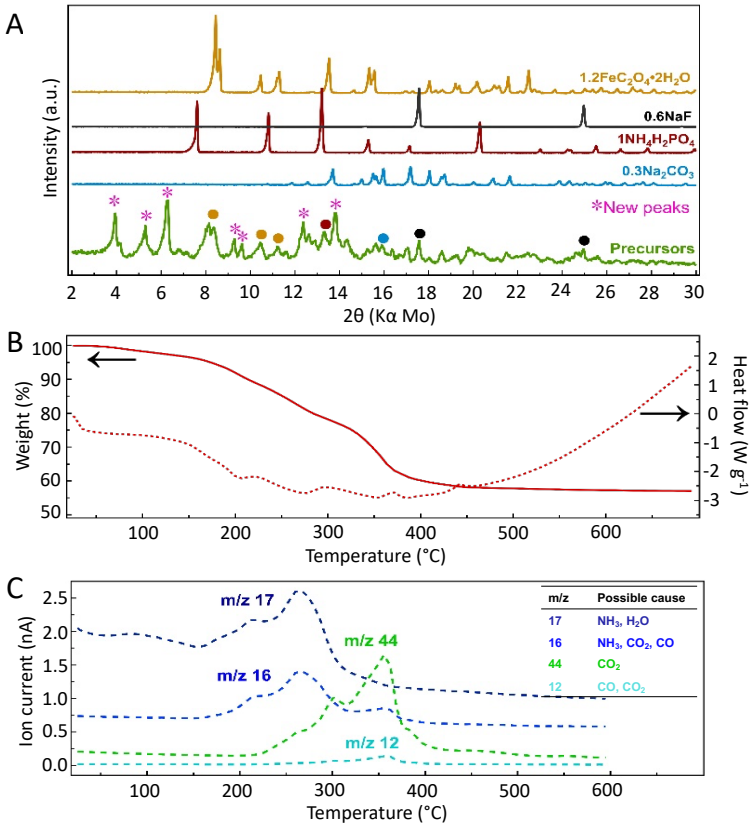

Figure 3.2 Insight into synthesis process of $Na_{1.2}Fe_{1.2}PO_4F_{0.6}$ materials (A) Powder X-ray Diffraction (PXRD) patterns of starting materials and precursors prepared by high-energy ball milling of starting materials before annealing. (B) TGA-DSC and (C) corresponding MS analysis for the precursors annealing step.

milling leading to different phases, **Figure 3.3**). The two high-energy ball milled samples (BM1 and BM2) show similar patterns, whereas the pattern for planetary ball milled sample (BM3) is different with peaks from maricite $NaFePO_4$ and FeO_x impurities. Unreacted NaF can be observed in the pattern of product made by hand grinding. The rest of the peaks are broadened possibly requiring longer time or higher temperature for further reaction. This indicates that high-energy ball milling can induce effective mechanochemical activation for precursors and then accelerates the solid-state reaction during annealing. As a result, some new intermediate materials have been identified and are presented in this work.

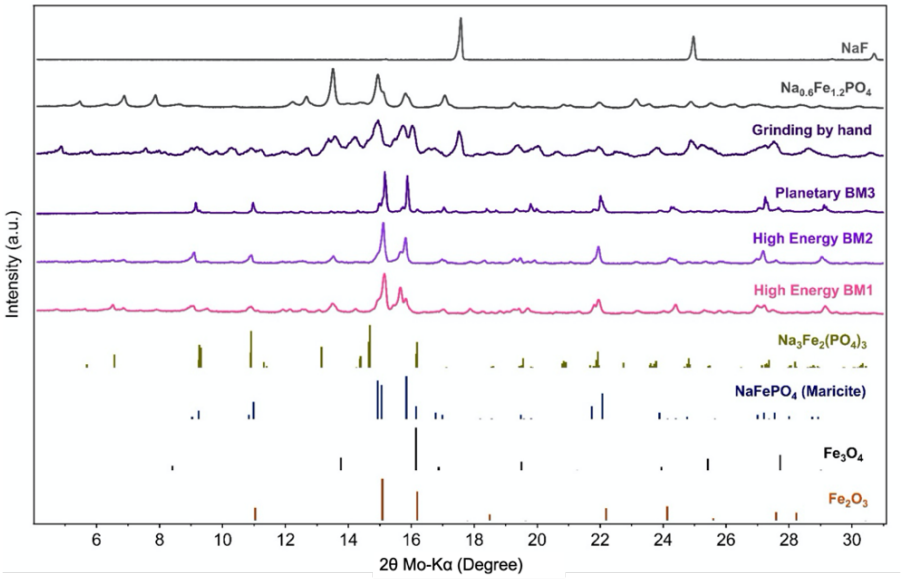

Figure 3.3 Comparison of PXRD patterns of $Na_{1.2}Fe_{1.2}PO_4F_{0.6}$ products using different approaches to prepare precursors (by grinding by hand or ball milling) followed by annealing under same conditions (550 °C for 12 h under Ar), together with PXRD patterns of NaF, $Na_{0.6}Fe_{1.2}PO_4$ and the peak assignment of possible impurities.[107]

Under high-energy ball milling conditions, new phases are formed, with also residuals of initial reactants (**Figure 3.2A**). Those new peaks in the PXRD pattern of precursors can be indexed to sodium amide phosphate hydrate, sodium imide phosphate hydrate and / or sodium phosphate hydrate, indicating that not only intimate mixing but also chemicals reactions occurred during this step. This can lower the diffusion length and barriers to diffusion for subsequent solid-state annealing step, which is often favourable to production of metastable phases.[82, 83]

Combined thermogravimetric analysis, differential scanning calorimetry and mass spectrometry (TGA-DSC-MS) further revealed a series of important features upon which we extensively relied to access the different phases in this work. The TGA data shows that the major mass losses occur between 100 °C and 350 °C assigned to the decomposition of the precursors, corresponding to exothermic processes over the same temperature as detected by DSC. The MS survey indicates removal of H_2O, NH_3, CO_2 and CO as the decomposition products, with no traces of HF, suggesting no F loss during annealing. The estimated total mass removal at 400 °C corresponds to a remaining composition of $Na_{0.6+x}Fe_{1.2}PO_4F_x$ as targeted (this elemental composition being also confirmed by other techniques, **Figure 3.4** and **Table 3.3**). Past this temperature, no further chemical composition change can be detected, and the endothermic processes taking place can be associated with further solid-state diffusion reaction and processes.

Note that the synthesis of the compounds requires strict inert atmosphere to avoid oxidation or reduction of Fe during annealing. **Figure 3.5** displays PXRD patterns of $Na_{1.2}Fe_{1.2}PO_4F_{0.6}$ products annealed for 12 h using different furnaces. With the patterns compared, it can be seen that $Na_{1.2}Fe_{1.2}PO_4F_{0.6}$_M synthesized via Furnace 1 (F1) at 550 °C cannot be perfectly reproduced using other furnaces. It tends to form

$Na_{1.2}Fe_{1.2}PO_4F_{0.6}$_S with $Na_3Fe_2(PO_4)_3$, maricite $NaFePO_4$ or FeO_x impurities. This could be because the decomposition of $FeC_2O_4{\cdot}2H_2O$ varies in different furnaces or under different atmospheres.[171, 172] To verify that, certain amount of $FeC_2O_4{\cdot}2H_2O$ has been treated under the same condition as how the compounds were annealed in the furnaces, and PXRD patterns of the decomposition products are shown in **Figure 3.6**.

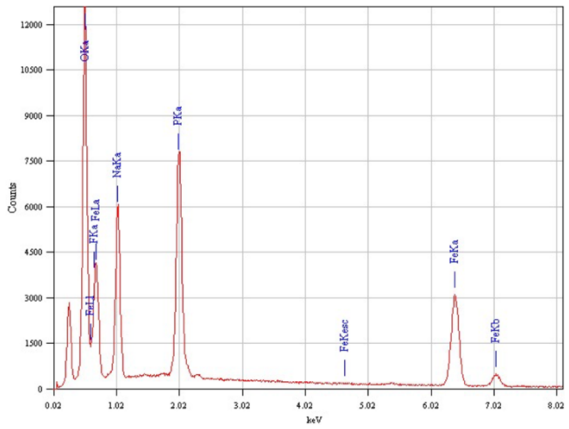

Figure 3.4 SEM-EDX of $Na_{1.2}Fe_{1.2}PO_4F_{0.6}$_M as an example for chemical composition analysis. Signals of all the elements in the compound can be detected. The peak at 0.277 keV is an artificial carbon peak.

Table 3.3 The atomic ratio of Na, Fe and P in $Na_{1.2}Fe_{1.2}PO_4F_{0.6}$_M measured by different techniques. The values from full-spectrum direct-reading inductively coupled plasma emission spectrometry (ICP, SPECTRO BLUE SOP) analysis are very close to theoretical composition (ratio of 1.2:1.2:1) based on the content of elements in starting precursor. The deviation in values from SEM-EDX could be due to measurement errors during EDX analysis which is very sensitive on many factors such as beam parameters, topography of sample, and atomic number of an element, and so on.

Sample	**Elemental ratio (Na:Fe:P)**		
	Nominal	**SEM-EDX**	**ICP**
$Na_{1.2}Fe_{1.2}PO_4F_{0.6}$_M	1.2:1.2:1	1.38:1.47:1	1.13:1.18:1

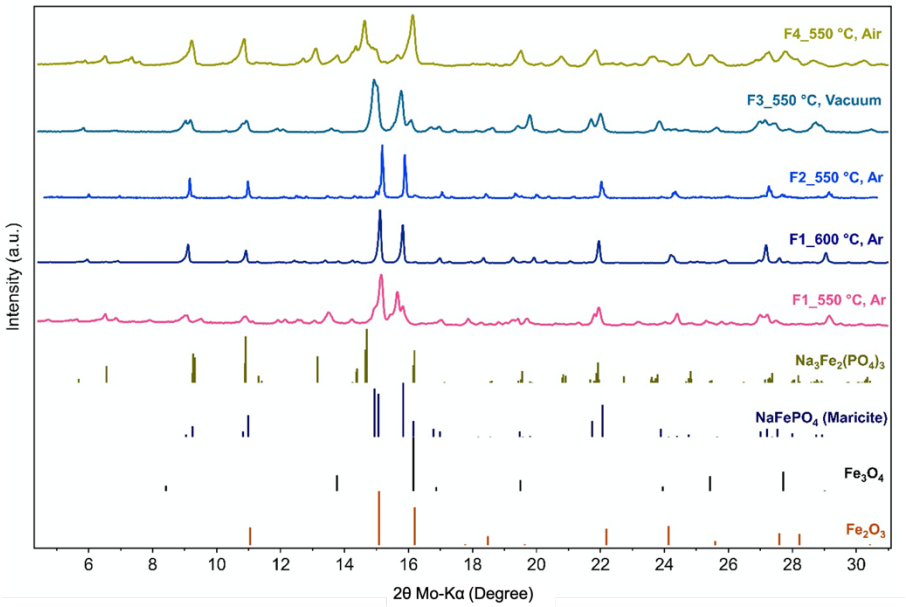

Figure 3.5 PXRD patterns of $Na_{1.2}Fe_{1.2}PO_4F_{0.6}$ products annealed for 12 h using different furnaces.

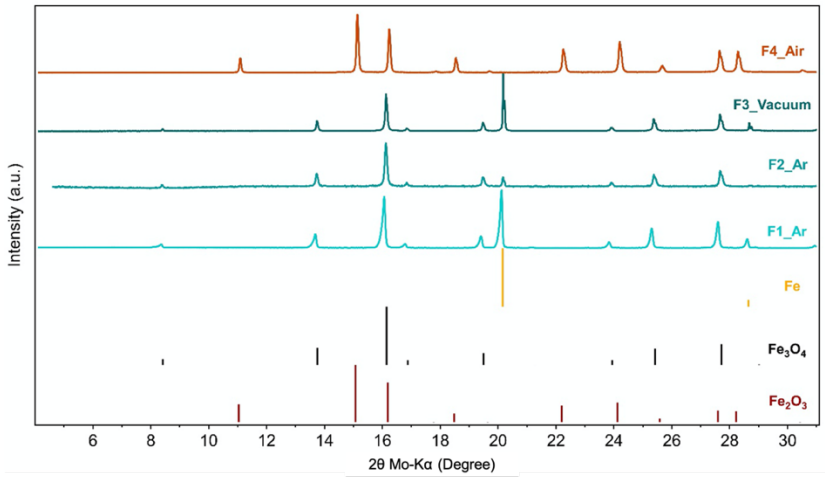

Figure 3.6 PXRD patterns of decomposition products of Fe(II)-oxalate using different furnaces.

It has been reported that its primary decomposition products are dependent on conditions and a mixture of Fe and Fe_3O_4 can form in an inert atmosphere ($FeC_2O_4 \rightarrow Fe + Fe_3O_4$).[171, 173] The peaks of the products can be indexed to the mixture of Fe and Fe_3O_4 for those annealed under Ar or vacuum, but the intensity of Fe and Fe_3O_4 varies significantly for different furnaces. It should be noted that all the furnaces are tube furnace, but only F1 is equipped with flange for effective sealing. Rubber or ground glass stopper were used as homemade sealing system for F2 and vacuum system in F3 has also been tried. Without fast inert gas flow during annealing or when the vacuum is inefficient, the decomposition could be under reductive atmosphere due to the gas residue (CO) for the vacuum furnace. In contrast, if the sealing system is not effective enough and gas leaking would occur, the iron could be oxidized to higher valence by air, resulting in presence of residual Fe^{3+} phases and miss of desired products. This could explain why the $Na_{1.2}Fe_{1.2}PO_4F_{0.6}$_M was failed to be prepared in other furnaces. The purity of the obtained compounds depends on the growth parameters, such as the temperature of calcination, and exposure time.[82] The impurity is possible especially at high temperature for long time, resulting from a small amount of oxygen included in inert gas flow and/or residual air trapped in the small pores of the particles.

3.2.2 The chemical space of $Na_{0.6+x}Fe_{1.2}PO_4F_x$ compositions and materials

Based on the three main degrees of freedom - the annealing temperature, reaction time and composition (**Figure 3.1C**) - characterizing the chemical space of $Na_{0.6+x}Fe_{1.2}PO_4F_x$ - we were able to synthesise as many as fourteen (14, **Figure 3.1C**) new materials. An overview of these is presented in **Figures 3.7 and 3.8**. From these free parameter analyses,

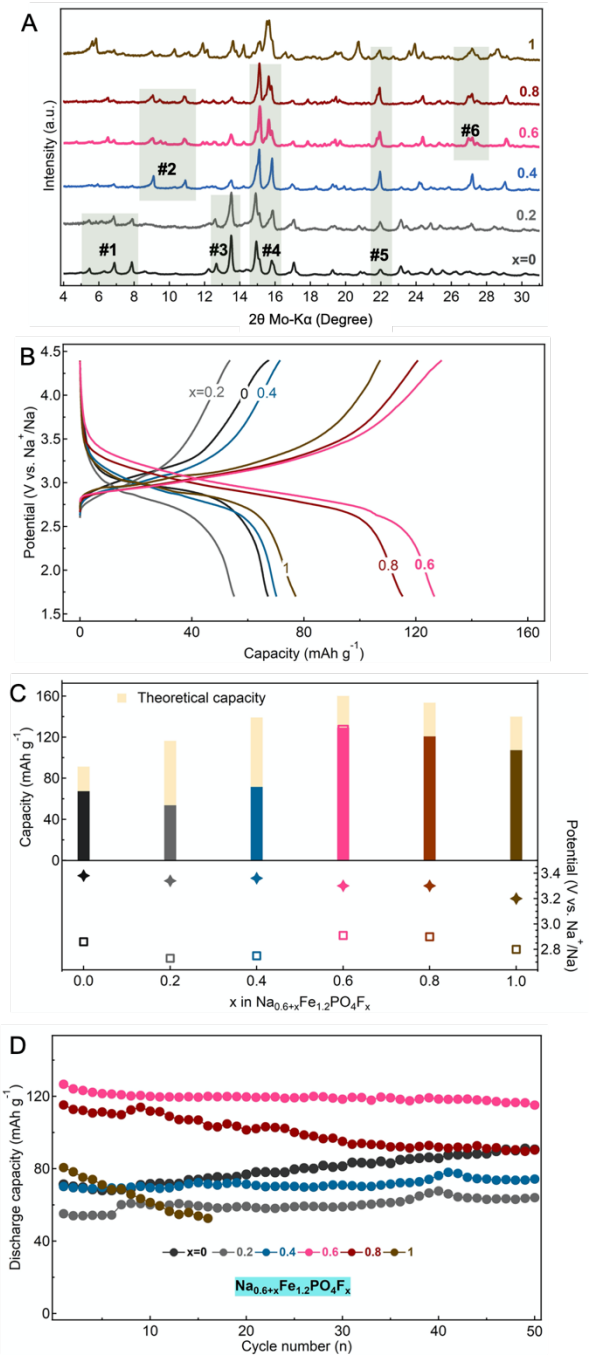

Figure 3.7 (A) PXRD survey of $Na_{0.6+x}Fe_{1.2}PO_4F_x$ series for various x. (B) First cycle potential vs. capacity galvanostatic plots for studied compositions. (C) Charge capacity (top) and average reduction potential evolution function of x in $Na_{0.6+x}Fe_{1.2}PO_4F_x$. The potentials were calculated through dividing the energy density (mAhV g^{-1}) by the maximum capacity (mAh g^{-1}). (D) Cycling performance of the $Na_{0.6+x}Fe_{1.2}PO_4F_x$ materials at a current density of 5 mA g^{-1}.

the $Na_{1.2}Fe_{1.2}PO_4F_{0.6}$ (x=0.6) composition prepared at 550 °C for 12 h was found to display the best performance and is considered as the main investigation target, although other materials were also found electrochemically active with peculiar properties.

Figure 3.7 resumes the analysis of the compositional changes in the $Na_{0.6+x}Fe_{1.2}PO_4F_x$ series (x varied from 0 to 1 in steps of 0.2). All materials were prepared by annealing for 12 h at 550 °C, which was found to be the optimal condition for the best performing $Na_{1.2}Fe_{1.2}PO_4F_{0.6}$ material (refer to **Figure 3.8** for details) in terms of active material electrochemical utilization. The comparative analysis of the PXRD (**Figure 3.7A**) and associated electrochemical properties (**Figure 3.7B, C and D**) reveals series of peculiar features. The $Na_{0.6}Fe_{1.2}PO_4$ (x=0) material made in this work shows similarity to the one reported by Yamada, indicating the reproducibility of the method.[107] As the NaF content (or x) increases, the PXRD pattern gradually evolves, while also maintaining similarities for specific diffraction regions (marked with #1-6 in **Figure 3.7A**).The two sets of materials (x= from 0 to 0.2, or x= from 0.4 to 0.8) share similar PXRD patterns separately, attributed to possible solid solutions existing in the respective x ranges. The new diffraction peaks appearing for x=1 composition imply the co-existence of more than one phase, requiring further optimization of synthesis conditions to form a pure phase (if possible).

According to the molar ratio of Na to Fe in the $Na_{0.6+x}Fe_{1.2}PO_4F_x$ series, the highest capacity is expected to be attained for x=0.6 with also the redox potential increase proportional to x. Both capacity and redox potential have been indeed found to follow this expected trend (**Figure 3.7B and C**). The highest reversible capacity of 127 mAh g^{-1} is attained for $Na_{1.2}Fe_{1.2}PO_4F_{0.6}$ (x=0.6) at a current density of 5 mA g^{-1} (corresponding to a C/32 rate). Interesting to note the analogy and differences between similar groups of

phases with for example low capacities and low redox potential attained for x=0.2; as well as for x=1. The materials obtained for x=0.6 and 0.8, albeit having similar PXRD patterns (despite minor differences), follow more closely the theoretical charge storage capacity estimates. The storage capacity difference between $Na_1Fe_{1.2}PO_4F_{0.4}$ (x=0.4) and $Na_{1.4}Fe_{1.2}PO_4F_{0.8}$ (x=0.8) can be explained by Na deficiency in the former (one electron-Na^+ theoretical redox) versus limited Fe content for the later (1.2 electron-Na^+ theoretical redox), while acquiring a higher molecular weight (192.5 and 209.4 g mol^{-1}, respectively). The redox potentials of these different materials are generally found to correlate with F content where F-rich materials do display the higher redox potential. The presented materials also display stable capacity retention, except the highest end member x=1 (**Figure 3.7D**).

Since in the series of $Na_{0.6+x}Fe_{1.2}PO_4F_x$ the composition with x=0.6 displays the best electrochemical performance (**Figure 3.7B**), its formation dynamics was investigated in parallel. Starting from the same precursors amounts and processing conditions (**Figure 3.2**), different annealing conditions were applied: from the lowest temperature and shortest time (350 °C, 1h) to gradually the highest temperature and longer annealing time (600 °C, 12h). The PXRD pattern evolution, the 1st cycle charge-discharge potential profiles and the corresponding dQ/dV curves are summarized in **Figure 3.8**.

The mass loss for the material prepared at 350 °C for 1h was measured to be very close to the value from TGA analysis (**Figure 3.2**), indicating complete decomposition of the starting materials under such condition. Only a broad diffraction pattern can be seen for this sample, suggesting an amorphous (or non-crystalline) state of $Na_{1.2}Fe_{1.2}PO_4F_{0.6}$ composition, as a result of a process sufficient for precursors decomposition yet not enough for structural ordering – in other words, an intermediate phase of the

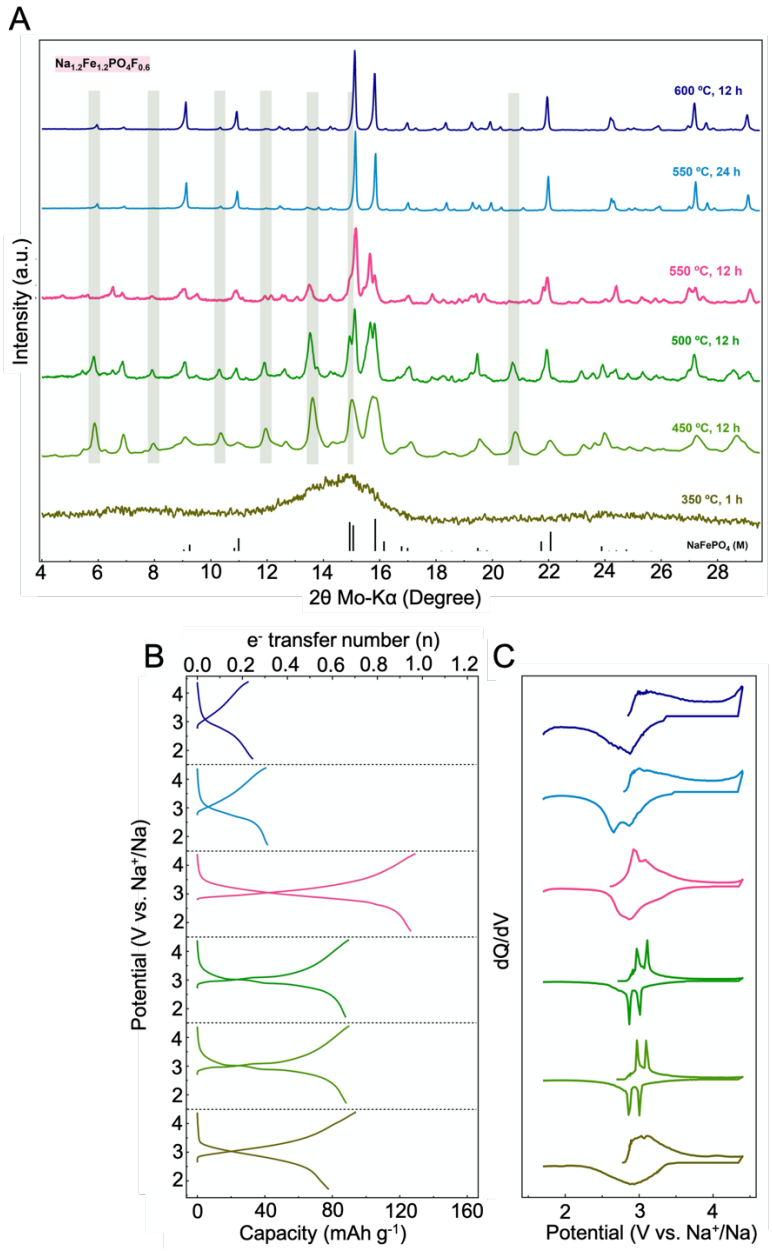

Figure 3.8 Phase diversity. (A) PXRD survey, (B) first cycle potential vs. capacity profile, and (C) corresponding normalized dQ/dV of the $Na_{1.2}Fe_{1.2}PO_4F_{0.6}$ materials.

thermodynamically stable product synthesis (**Figure 3.1B**). Surprisingly, this phase was found to be electrochemically active and deliver ca. 80 mAh g^{-1} (corresponding to 0.6 Na exchange), with sloping potential profiles and a corresponding broad redox dQ/dV peak (characteristic of amorphous materials). Further annealing defines the onset of phase(s) crystallization, higher material utilization, with also changes in the redox potentials (some similar intermediate products data not shown here).

The material prepared at 500 ºC for 12 h displays clear signs of crystallinity, presumably being composed of more than one phase. The two charge-discharge plateaus near 3 V (vs. Na^+/Na) or the corresponding sharp redox peaks in the dQ/dV curve could be another indication of a multiple phase composition although additional studies are required to ascertain this. As the annealing temperature is increased to 550 ºC, additional diffraction peaks disappear or become weaker (most significant being at 2Theta = 5.4, 7.9, 10.3, 11.9, 13.5, 14.9 and 20.8°, marked in grey), with only minor changes detected for annealing durations of 6 h and 12 h (both at 550 °C, the main difference being the change in the relative intensities of certain peaks). We assign this to the formation of new phase(s). The two materials share similar galvanostatic potential and dQ/dV profiles, with however the phase annealed for 12 h displaying considerably higher material electrochemical utilization.

Further annealing dramatically alters the process with also further phase evolution. Additional 12 h of annealing at 550 °C, or processing at higher temperatures (e.g. 600 °C) yielded a material with reduced number, yet sharper diffraction peaks, assigned as the thermodynamically stable phases of $Na_{1.2}Fe_{1.2}PO_4F_{0.6}$. Surprisingly, the electrochemistry of these end-series samples displayed the worst electrochemical activities, with less than 0.3 Na equivalents being possible to extract (at a current density of 5 mA g^{-1}) accompanied also by high polarization.

From this preliminary compositional and phase library mapping, the $Na_{1.2}Fe_{1.2}PO_4F_{0.6}$ composition clearly stands out as the best performing at this stage with the highest voltage and electrochemical utilization. Since the amorphous, metastable as well as stable materials could be isolated, we extensively characterized these to correlate the phase(s) and structure with the electrochemical activity. It should be however noted that this might not be eventually the best one as theoretically, we have explored only a minor part of the chemical space of (meta)-stable Na-Fe-PO_4-F compositions (**Figure 3.1C**). For sake of simplicity and clarity, hereafter the amorphous phase (annealed for 1 h at 350 ˚C) is denoted as $Na_{1.2}Fe_{1.2}PO_4F_{0.6}$_AM, and the metastable material prepared at 550 ˚C for 12 h as $Na_{1.2}Fe_{1.2}PO_4F_{0.6}$_M whereas the stable phase (prepared at 550 ˚C for 24 h or the one at 600 ˚C for 12 h) is termed as $Na_{1.2}Fe_{1.2}PO_4F_{0.6}$_S. The three will be of central interest in following discussion.

3.2.3 Comparative analysis of $Na_{1.2}Fe_{1.2}PO_4F_{0.6}$_S, _M and _AM

The large discrepancy in the crystallinity as well as the electrochemistry of the two _S (thermodynamically stable) and _M (metastable) materials, while being accessed in a narrow synthesis conditions range, motivated us for additional extended physicochemical analysis. Meanwhile, the properties of the _AM (amorphous) phase have also been evaluated for comparison. Indexing of the $Na_{1.2}Fe_{1.2}PO_4F_{0.6}$_S phase (**Figure 3.9A**) revealed its similarity to a reported iron-based compound $Ca_{0.1667}Na_{3.6667}FeP_2O_8F$ (ICSD #079632)[174] with however slight variations in the lattice parameters applied for $Na_{1.2}Fe_{1.2}PO_4F_{0.6}$_S: indexed to trigonal $P\bar{3}$ space group, with lattice parameters: a = b = 13.625

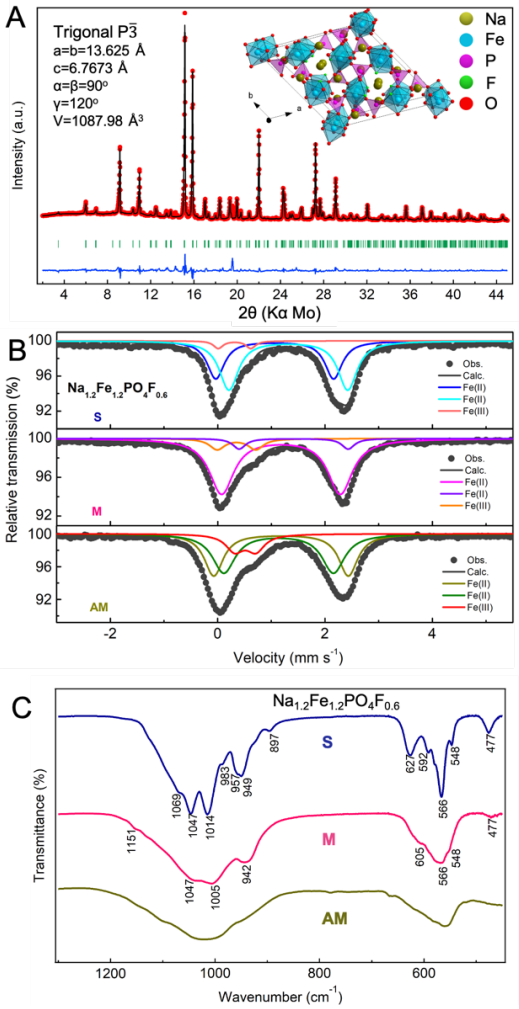

Figure 3.9 Characterizations of $Na_{1.2}Fe_{1.2}PO_4F_{0.6}$_S, _M and _AM. (A) PXRD patterns and results of the Rietveld refinement of $Na_{1.2}Fe_{1.2}PO_4F_{0.6}$_S: the red dots are the observed data, the black lines are the calculated patterns, the blue lines show the difference between the calculated and observed patterns whereas the green bars correspond to the expected positions of the Bragg reflection peaks. The inset in (A) shows the crystal structure of $Na_{1.2}Fe_{1.2}PO_4F_{0.6}$_S and views in different directions can be found in **Figure 3.10**. (B) Room-temperature Mössbauer and (C) Fourier transform infrared (FT-IR) spectroscopy spectra of $Na_{1.2}Fe_{1.2}PO_4F_{0.6}$_S, _M and _AM materials.

Å, c = 6.7673 Å, α = β = 90°, γ = 120° and V = 1087.98 Å^3 (**Figures 3.9A, 3.10** and **Table 3.4**). The resolution reveals a three-dimensional framework with corner-sharing PO_4 tetrahedral and FeO_6/FeO_5F octahedral units. Na^+ either locate in tunnels surrounded by the Fe octahedral and P tetrahedral groups or alternate with PO_4 tetrahedrons along the c-axis. The composition was determined to be $Na_{16}Fe_{13}(PO_4)_{12}F_6$ ($Na_{1.33}Fe_{1.08}PO_4F_{0.5}$) with higher content of Na than the nominal composition of $Na_{1.2}Fe_{1.2}PO_4F_{0.6}$, resulting from the limitations and imperfections of refinement by using PXRD data. The PXRD indexing of the $Na_{1.2}Fe_{1.2}PO_4F_{0.6}$_M has also been performed but a plausible refinement solution is hardly accessed. Although a solution can be attained by synchrotron PXRD analysis, a large unit cell volume of 8297 Å^3 indicates mixture of phases in $Na_{1.2}Fe_{1.2}PO_4F_{0.6}$_M (**Figure 3.11**). The phases structures of this metastable material require further in-depth investigation to understand the origin of its greatly enhanced Na storage performance in comparison to the stable counterpart.

The local coordination environment of Fe ions in $Na_{1.2}Fe_{1.2}PO_4F_{0.6}$_S, _M and _AM phases has been further investigated via Mössbauer spectroscopy (**Figure 3.9B**, fitting parameters are listed in **Table 3.5**). The spectrum of $Na_{1.2}Fe_{1.2}PO_4F_{0.6}$_S can be fitted to three doublets, corresponding to two types of Fe(II) environment (accounting for 34 and 61%, respectively) and one type of Fe(III) environment (5%). The relatively high isomer shift (δ) values (> 1 mm/s) of the two Fe(II) species indicate octahedral coordination (O_h), which agrees well with the FeO_6 and FeO_5F octahedra in the crystal structure of $Na_{1.2}Fe_{1.2}PO_4F_{0.6}$_S. To be noted that Mössbauer spectra reveal no presence of Fe_2O_3 in these materials with the Fe(III) component with low δ and ΔE_Q values present in the three materials, being due to surface oxidation during the long acquisition time (approximately two weeks).

Two Fe(II) (O_h) sites were also detected for $Na_{1.2}Fe_{1.2}PO_4F_{0.6}$_M, but the corresponding fit parameters are different, implying no $Na_{1.2}Fe_{1.2}PO_4F_{0.6}$_S (impurity) phase in the $Na_{1.2}Fe_{1.2}PO_4F_{0.6}$_M. The main Fe(II) ($O_h$) site (accounting to as much as 82%) has δ (1.17 mm/s) and a quadrupole splitting (ΔE_Q, 2.21 mm/s) parameters close to those of reported $Na_2Fe(II)PO_4F$ phase (typically 1.23 and 2.19 mm/s, respectively).[175] The weak remaining signal representing only 8% is attributed to structural defects or impurities, and it could be also formed from exposition to air during the long analysis time.[176] Note that δ and ΔE_Q the values (δ = 0.34 and ΔE_Q = 0.72 mm/s) of Fe(III) (O_h) for $Na_{1.2}Fe_{1.2}PO_4F_{0.6}$_M are roughly equivalent to those for $NaFe(III)PO_4F$ (δ = 0.37 and ΔE_Q = 0.71 mm/s), together with the similar parameters of the Fe(II) site mentioned above, implying that $Na_{1.2}Fe_{1.2}PO_4F_{0.6}$_M possesses similar Fe environment to that in the $Na_2Fe(II)PO_4F$ and the minor Fe(III) species/content originate from the air-exposure oxidation of the main Fe(II) site component rather than the weak one.[177] According to the Mössbauer spectroscopy analysis, it can be assumed that the $Na_{1.2}Fe_{1.2}PO_4F_{0.6}$_M material could consist of mainly a single-phase component but with impurity phase(s).

The $Na_{1.2}Fe_{1.2}PO_4F_{0.6}$_AM has two Fe(II) ($O_h$) sites with different δ and ΔE_Q values from the $Na_{1.2}Fe_{1.2}PO_4F_{0.6}$_S and_M, but the values are found to be very close to those of two main sites for $Na_{0.6}Fe_{1.2}PO_4$ (see the highlighted values in **Table 3.5**), indicating the similar Fe environment in $Na_{1.2}Fe_{1.2}PO_4F_{0.6}$_AM and $Na_{0.6}Fe_{1.2}PO_4$. This could imply the existence of $Na_{0.6}Fe_{1.2}PO_4$ or similar compound in amorphous state in the $Na_{1.2}Fe_{1.2}PO_4F_{0.6}$_AM. Together with further assessment and comparison of PXRD pattern evolutions in **Figures 3.7A and 3.8A**, where some peaks, especially at 13.5 and 14.9° found as two main peaks in the pattern of $Na_{0.6}Fe_{1.2}PO_4$ (x=0) become less pronounced either as x (the content of NaF)

increases or annealing temperature elevates for $Na_{1.2}Fe_{1.2}PO_4F_{0.6}$ composition, it can be assumed that $Na_{0.6}Fe_{1.2}PO_4$ may tend to form first and then get converted to $Na_{0.6+x}Fe_{1.2}PO_4F_x$ material(s) upon further annealing.

To further understand the phase composition and structure of $Na_{1.2}Fe_{1.2}PO_4F_{0.6}$_S, _M and _AM materials, we analysed the vibration modes of PO_4^{3-} units by Fourier transform infrared (FT-IR) spectroscopy (**Figure 3.9C**). The obtained spectra are consistent with those for maricite $NaFePO_4$, Na_2FePO_4F and Li_2CoPO_4F, with symmetric ν_1 and asymmetric ν_3 stretching modes located in the high-wavenumber region (900−1200 cm^{-1}), and the symmetric ν_2 and asymmetric ν_4 bending modes in the 450 to 650 cm^{-1} range.[178-180] All three materials share similar vibration peaks/bands, despite minor shift for some bands. However, broadening of the vibration bands are without exception identified in the case of _M and _AM materials as compared to the stable (_S) one. The broadened bands phenomenon has also been observed in this class of compounds in glass or amorphous state in literature and could be attributed to large difference in bond distances or disordering.[175, 181] This implies an elevated degree of disorder in the structure of the $Na_{1.2}Fe_{1.2}PO_4F_{0.6}$_M.

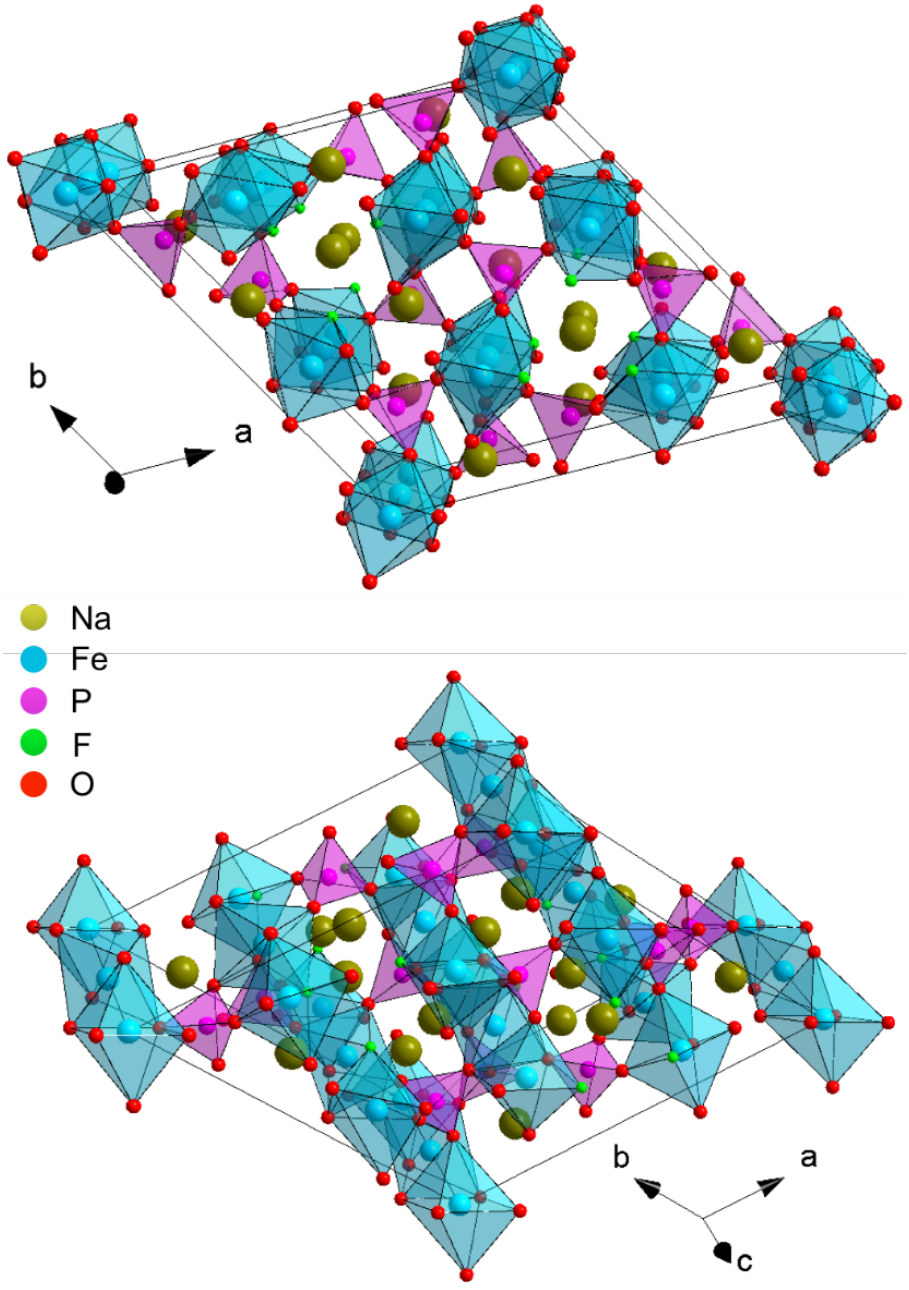

Figure 3.10 Crystal structure of $Na_{1.2}Fe_{1.2}PO_4F_{0.6}$_S from different view directions.

Table 3.4 Rietveld refinement results and atomic positions for $Na_{1.2}Fe_{1.2}PO_4F_{0.6}$ S.

Phase: $Na_{16}Fe_{13}(PO_4)_{12}F_6$, Trigonal, space group P
a = b = 13.625 Å, c = 6.7673 Å, α = β = 90°, γ = 120°, V = 1087.98 Å^3
Bragg R-factor = 8.21, Rf-factor = 7.91

Atom	x	y	z	B	Occ	Mult
Fe1	0.57731	0.70453	0.49198	1.243	1	6
Fe2	0	0	0	1.243	0.167	1
P1	0.62592	0.51145	0.76026	0.793	1	6
P2	0.81461	0.75062	0.25606	0.793	1	6
Fe3	0	0	0.5	0.793	0.071	1
Na2	0.33333	0.66667	1.0392	8.444	0.333	2
Na3	0.33333	0.66667	0.50898	8.444	0.333	2
Fe4	0.86966	0.58048	1.00113	1.243	1	6
Na5	0.06446	0.8193	0.23398	0.460	1	6
Na6	0.3908	0.49786	0.73202	0.539	1	6
F1	0.48511	0.71794	0.74036	0.926	1	6
O1	0.56061	0.44374	0.57623	0.926	1	6
O2	0.61476	0.61803	0.78273	0.926	1	6
O3	0.75001	0.54445	0.74727	0.926	1	6

Atom	x	y	z	B	Occ	Mult
O4	0.57098	0.43532	0.94494	0.926	1	6
O5	0.68726	0.70581	0.26085	0.926	1	6
O6	0.85145	0.71364	0.4453	0.926	1	6
O7	0.87875	0.8812	0.24742	0.926	1	6
O8	0.84814	0.70534	0.07493	0.926	1	6

Table 3.5 ^{57}Fe Mössbauer parameters obtained by fittings for $Na_{1.2}Fe_{1.2}PO_4F_{0.6}$_S, _M, _AM and $Na_{0.6}Fe_{1.2}PO_4$. Isomer shift (δ) are given with respect to metallic α-Fe. DE_Q = quadrupole splitting. Γ/2 = half width of the lines.

Sample	Site	δ (mm/s)	ΔE_Q (mm/s)	Γ/2 (mm/s)	Area fraction (%)
$Na_{1.2}Fe_{1.2}PO_4F_{0.6}$_S	**Fe(II)**	1.06	2.18	0.17	34
	Fe(II)	1.29	2.24	0.21	61
	Fe(III)	0.6	0.18	0.14	5
$Na_{1.2}Fe_{1.2}PO_4F_{0.6}$_M	**Fe(II)**	1.17	2.21	0.27	82
	Fe(II)	1.41	2.03	0.14	8
	Fe(III)	0.34	0.72	0.17	10
$Na_{1.2}Fe_{1.2}PO_4F_{0.6}$_AM	**Fe(II)**	**1.18**	**2.51**	**0.21**	40
	Fe(II)	**1.14**	**2.04**	**0.25**	45
	Fe(III)	0.51	0.40	0.20	15
$Na_{0.6}Fe_{1.2}PO_4$	**Fe(II)**	1.19	2.87	0.17	18
	Fe(II)	**1.18**	**2.45**	**0.23**	47
	Fe(II)	**1.12**	**1.94**	**0.25**	33
	Fe(III)	0.64	0.24	0.28	12

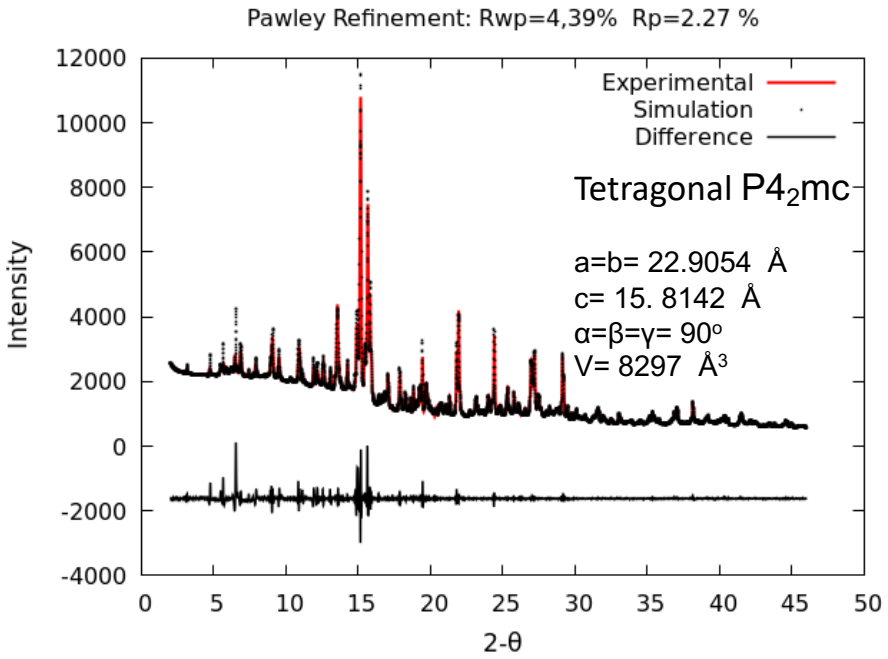

Figure 3.11. Synchrotron PXRD patterns and results of the Rietveld refinement of $Na_{1.2}Fe_{1.2}PO_4F_{0.6}$_M.

The powder diffraction pattern was recorded with Synchrotron radiation, wavelength being **λ** = 0.7085Å and the selected angular range 2**θ** between 2^0 and 46^0. Various indexing programs such as Treor, Ito, Dicvol, X-Cell from Reflex modules, implemented in Materials Studio software were used. The solutions with the highest confidence factor were obtained with the X-cell computing program. We have obtained that the compound crystallizes in the tetragonal system with the lattice parameters a = b = 22.9054Å and c = 15. 8142Å, the unit cell volume V = 8297Å^3 and the space group $P4_2mc$. The first 48/49 diffraction peaks were indexed, even those with very low intensity (the number of diffraction lines that can be entered in the program as input data is maximum of 50). We have obtained: Rel. Fom = 0.82 and FOM = 304 as reliable factors. These reliability factors are acceptable considering that the diffraction peaks are very broad and the positioning of the diffraction maxima is more difficult. To confirm the correctness of the obtained space group, Pawley Refinement was applied. After Pawley refining, the Rwp = 4.39%, and Rp = 2.27% were obtained.

3.2.4 Comparative analysis of charge storage performances of $Na_{1.2}Fe_{1.2}PO_4F_{0.6}$_M, _S, S/C and _AM materials

With the structure and solid-phase electrochemistry mechanism clarified, we have further analysed the Na storage performances of the respective materials. In terms of electrical conductivity of phosphate based polyanionic chemistries, the studied here $Na_{1.2}Fe_{1.2}PO_4F_{0.6}$ materials (valid also for other values of *x*) make no exception and are intrinsically insulating materials, and as with other chemistries of this class, carbon coatings can be applied to improve the charge transfer efficiency. Whereas a same logical could be pretended here, this has been revealed intrinsically impossible for the _M and _AM materials. In fact, being a metastable material, further annealing has been found to result in the thermodynamically stable one (_S phase, **Figure 3.12**). The carbon coated _S phase composite ($Na_{1.2}Fe_{1.2}PO_4F_{0.6}$_S/C) is in turn possible to attain and was prepared by simply adding a carbon source during the ball milling step (refer to **Figure 3.13** and associated content). The pore size distribution and specific surface areas of $Na_{1.2}Fe_{1.2}PO_4F_{0.6}$_M, _S/C and _S were characterized and compared using Brunauer-Emmett-Teller technique (BET, **Figure 3.14**) and gave the following values: 28, 17.9 and 4.9 $m^2\ g^{-1}$, respectively.

The microstructure and morphology of $Na_{1.2}Fe_{1.2}PO_4F_{0.6}$_M, _S and _S/C were also characterized and the images are shown in **Figure 3.15**. The small particle size of $Na_{1.2}Fe_{1.2}PO_4F_{0.6}$_M can be seen in the SEM image and it exhibits porous morphology with the pore size of ca. 100−200 nm, which is greatly noticeable in its HAADF image. It could be induced from the decomposition of the organic species releasing gases such as carbon dioxide, leading to abundant pore structures in the material. From

the electrochemical point of view, the porosity structures are advantageous to penetration of the liquid electrolyte through the particles. With higher temperature or longer annealing time for synthesis, the $Na_{1.2}Fe_{1.2}PO_4F_{0.6}$_S show dense particles in larger size. However, under the same annealing conditions, the particle growth has been inhibited by adding carbon source in starting materials before ball milling, resulting in its carbon coating counterpart ($Na_{1.2}Fe_{1.2}PO_4F_{0.6}$_S/C) with smaller and porous particle morphology. Those are accordant with the BET results in **Figure 3.14**. Additionally, the uniform distribution of Na, Fe, P, O, and F in typical particle for three compounds in the mapping images indicate that the raw reagents have been homogenously mixed in the ball milling process, ensuring the homogeneity of the obtained compounds.

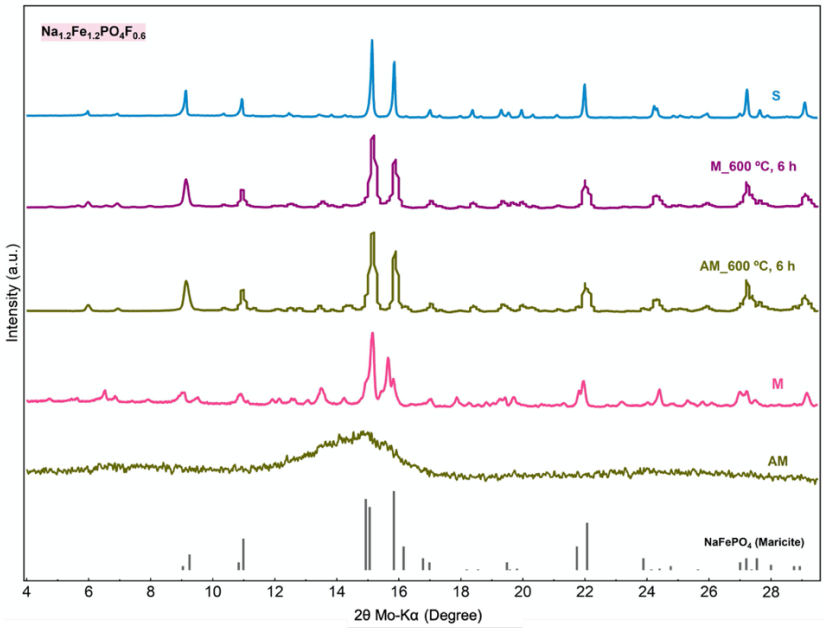

Figure 3.12 PXRD of $Na_{1.2}Fe_{1.2}PO_4F_{0.6}$_AM and _M annealed at 600 °C for 6 h, compared with the _AM, _M and _S counterparts.

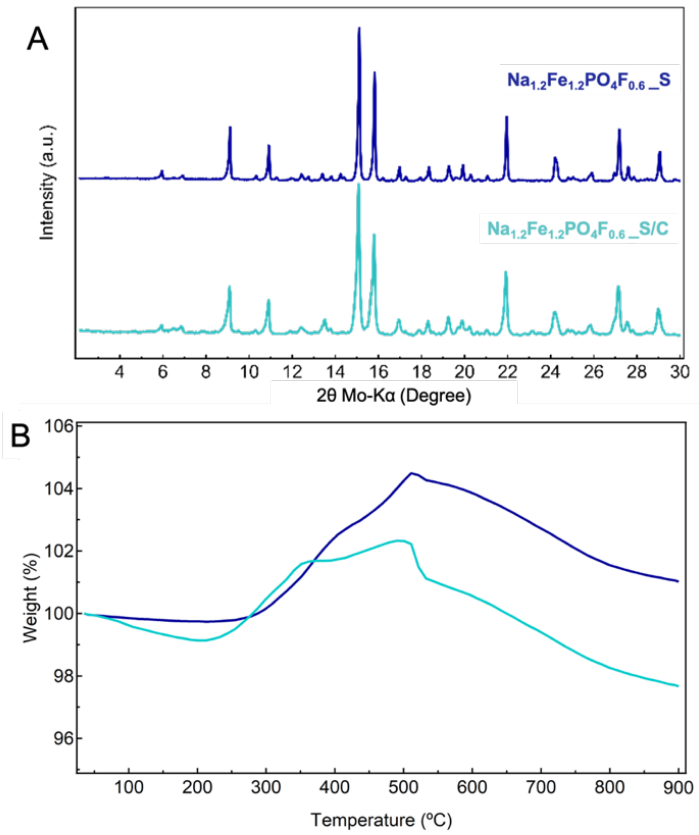

Figure 3.13 (A) PXRD and (B) TGA in air of $Na_{1.2}Fe_{1.2}PO_4F_{0.6}$ _S and _S/C. As expected, peak positions in the PXRD pattern does not change with a certain amount of carbon source added in starting materials before ball milling, but the peaks become broadened, resulting from its smaller particle size morphology. The carbon content of about 3 wt.% in the composite was estimated by the TGA test, considering that the mass change is from oxidation of Fe^{2+} to Fe^{3+} and carbon totally oxidized to CO_2 gas without residue. The equations can be built as follows: $M(Na_{1.2}Fe_{1.2}PO_4F_{0.6}) + M(carbon)=M_0$; $M(oxidized\ Na_{1.2}Fe_{1.2}PO_4F_{0.6})=M_1$ (M_0 is the starting mass and M_1 is the mass after measurement). $M(carbon)/M_0$ can be calculated as carbon content in the $Na_{1.2}Fe_{1.2}PO_4F_{0.6}$ _S/C.

The electrochemical performance of the respective materials was evaluated via similar galvanostatic charge-discharge protocols in Na half-cells and the results are summarized in **Figures 3.16 and 3.17**. When tested at 5 mA g^{-1} (C/32), the $Na_{1.2}Fe_{1.2}PO_4F_{0.6}$_S phase shows the lowest electrochemical active material utilization, with only 0.31 Na^+ equivalents being possible to extract within the tested electrochemical window, applied cell construct and analysis procedure. The electrochemical activity is clearly improved for the carbon coated $Na_{1.2}Fe_{1.2}PO_4F_{0.6}$_S/C analogue,

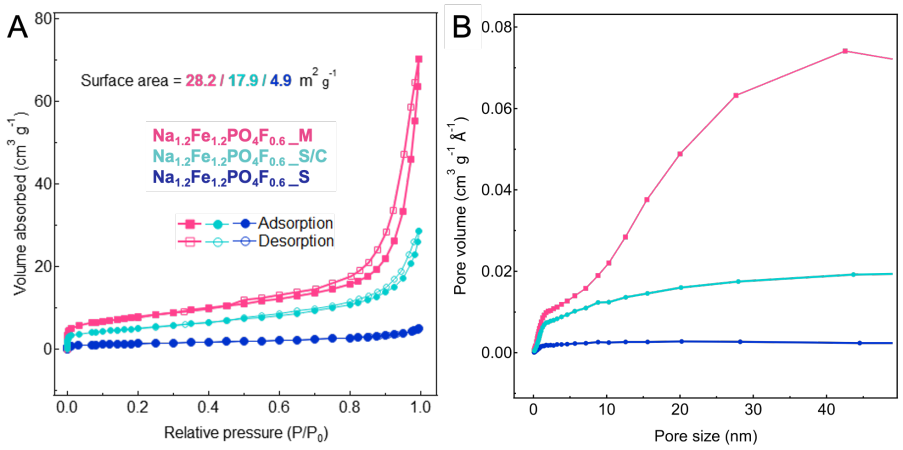

Figure 3.14 (A) Nitrogen-sorption isotherms (B) Pore size distribution of $Na_{1.2}Fe_{1.2}PO_4F_{0.6}$_M, _S and _S/C with pore size below 50 nm, as BET is able to accurately determine the surface area, volume, and pore size distribution for micro- and meso- pores. Micro-pores are below 2 nm, macro-pores are beyond 50 nm, and meso-pores are between 2nm and 50 nm.

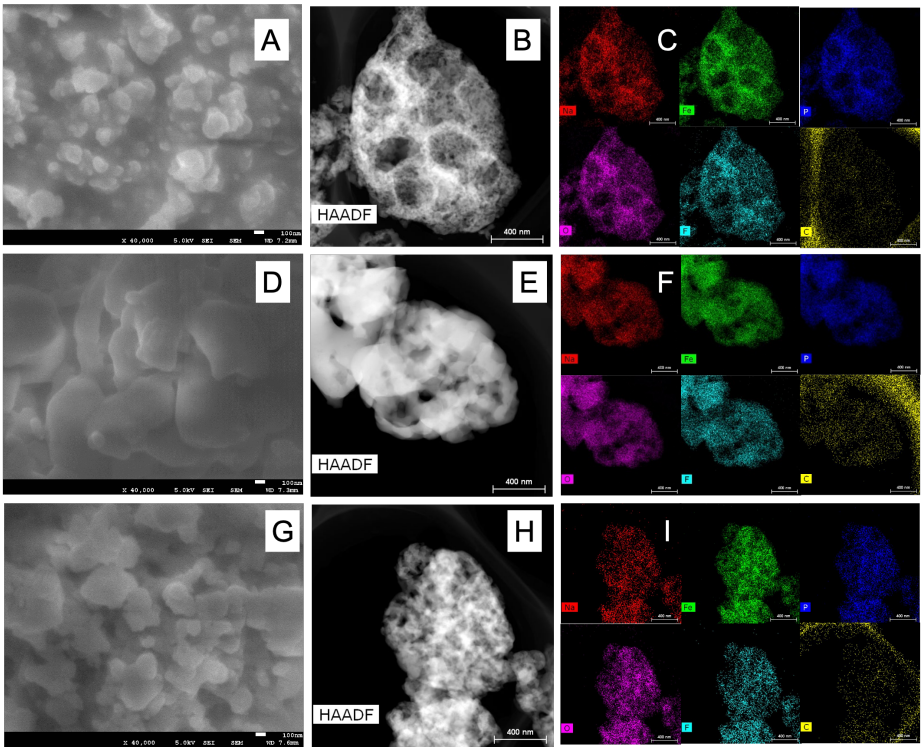

Figure 3.15 (A, D and G) SEM, (B, E and H) TEM-HAADF and (C, F and I) EDX mapping of elements images of $Na_{1.2}Fe_{1.2}PO_4F_{0.6}$_M, _S and _S/C, respectively.

with almost 0.56 Na^+ being possible to extract and reversibly insert, most certainly originating from a better electrochemical charge transfer. Surprisingly, the metastable $Na_{1.2}Fe_{1.2}PO_4F_{0.6}$_M material, despite not being carbon coated, delivers the largest reversible capacity, with 0.98 Na^+ equivalent being possible to reversibly exchange. One distinctive sloping plateau centered around 2.9 V (vs. Na^+/Na) can be seen in the potential profiles of both $Na_{1.2}Fe_{1.2}PO_4F_{0.6}$_M and $Na_{1.2}Fe_{1.2}PO_4F_{0.6}$_S/C, indicating a solid-solution electrochemical reaction. All three materials display good cycling stability with a capacity retention of more than 90% after 50 cycles at a charge-discharge rate of C/32 (**Figure 3.17A**).

Although about 94 mAh g^{-1} (0.7 Na extraction) can be attained by the $Na_{1.2}Fe_{1.2}PO_4F_{0.6}$_AM at first charge, only 86% is reversible and it shows a gradual decrease in capacity upon cycling (**Figure 3.17A and B**). The capacities for the other three materials stay stable. The CE for the _M, _S and _S/C cathodes are close to 100% over the period, except that the initial value for _S and _S/C are slightly higher than 100%, probably due to surface oxidation of materials obtained by annealing at high temperature or for very long time. In contrast, the CE for the _AM fluctuate severely around 100%. It suggests the unstable Na storage performance of this amorphous phase synthesised under low sintering temperature and the origins of this require further investigation.

The rate capability measurement further revealed outstanding capacity reversibility and long-term cycling stability of the $Na_{1.2}Fe_{1.2}PO_4F_{0.6}$_M material, again, despite not being a carbon-coated material. At low current density of 2 mA g^{-1} (equivalent of C/80 rate), almost the entire Na content (1.1 equivalents) can be reversibly extracted. The electrode maintains a high reversible capacity even at high rates, with almost 0.3 Na being possible to cycle at a rate of 2C. To compare, the _S phase delivered a low capacity when cycled at C/32, proving the higher electrochemical activity of the _M versus _S. The higher capacity delivered by the carbon coated _S/C phase can be attributed to the improved charge transfer, whereas the full material utilization in _M material is clearly not benefiting from this. Nanotexture as well as slightly higher surface area (_M > _S/C > _S) could be accounted as factors for improvement given possible intimate contact with carbon additive as well as lower diffusion scale. However, this clearly cannot be accounted for the observed improvements and the disordered structure of the _M material, with open Na diffusion channels in the crystal structure of the _M material advanced as the main explanation for the

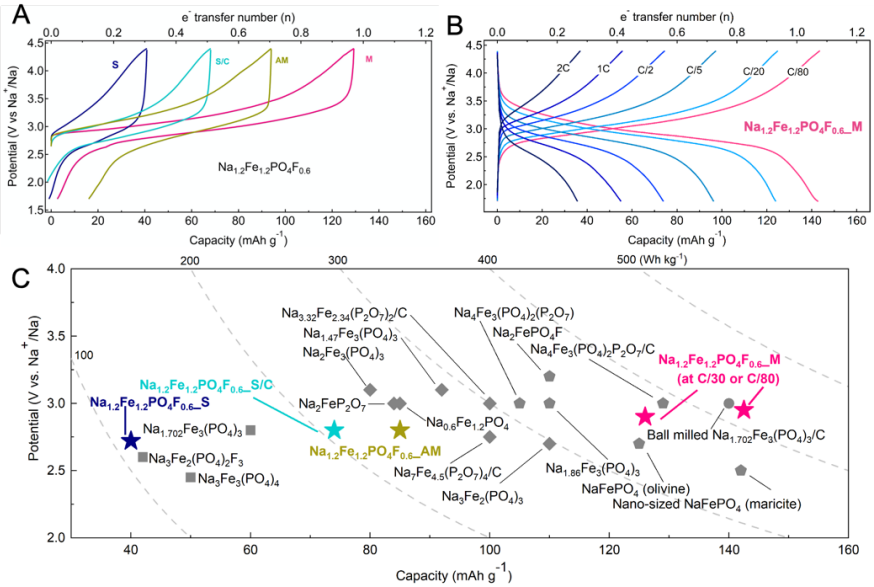

Figure 3.16 Comparative analysis of electrochemical performance. (A) First cycle potential vs. capacity galvanostatic plots for $Na_{1.2}Fe_{1.2}PO_4F_{0.6}$_M material and its stable (_S), carbon coated stable (_S/C) and amorphous (_AM) analogues. (B) Rate performance of $Na_{1.2}Fe_{1.2}PO_4F_{0.6}$_M electrode. (C) Energy density comparison (performances considered at the material level) of various iron phosphate and iron fluorophosphate cathode materials for SIBs.[107, 160, 182-195]

observed behaviour. The long-term cycling stability evaluated at C/2, following the variable rate test, clearly highlights the stability of this chemistry upon extended cycling and high current density utilization. In addition, the performance of the four main studied materials is compared with analogous cathode materials in literature, in terms of their average redox potential, reversible capacity and energy density in **Figure 3.16C**. The _M material stands out as one of the best with an energy density of about 400 Wh kg^{-1} estimated at the material level.

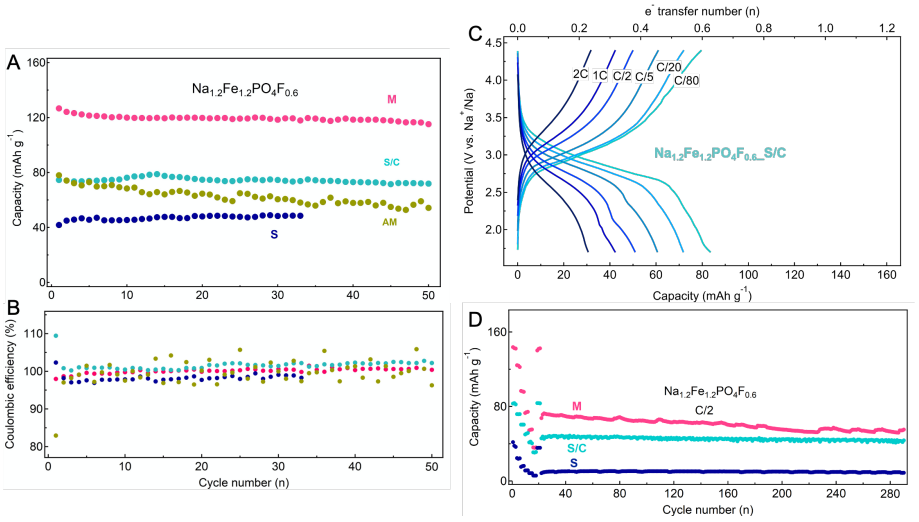

Figure 3.17 (A) Reversible discharge capacity and (B) coulombic efficiencies (CE) of $Na_{1.2}Fe_{1.2}PO_4F_{0.6}$_AM, _M, _S and _S/C cathode materials at 5 mA g^{-1} upon cycling. (C) Rate capability of the _S/C. (D) Reversible discharge capacity of $Na_{1.2}Fe_{1.2}PO_4F_{0.6}$_M, _S and _S/C cathode materials at different current densities and long-term cycling stability at C/2 (80 mA g^{-1}).

3.2.5 Tracking the reversible electrochemistry of $Na_{1.2}Fe_{1.2}PO_4F_{0.6}$_M

The charge and mass transfer kinetic behaviour of the $Na_{1.2}Fe_{1.2}PO_4F_{0.6}$_M electrode was examined using the galvanostatic intermittent titration technique (GITT, refer to Experimental Section). **Figure 3.18** depicts Na stoichiometry vs. potential profiles for charge and discharge process collected from GITT data. The profiles are similar to the galvanostatic charge-discharge ones in **Figure 3.16A**, and the full Na content can be extracted and reinserted under these close-to-equilibrium conditions. The sloping curve with no well-defined potential steps suggest the presence of solid solution behaviour over the entire Na extraction and insertion range.[169] Pronounced polarization occurs at end steps for both

charge and discharge processes, indicating the slow kinetics of Na diffusion when the electrode is approaching the theoretical capacity. The diffusion coefficient of Na^+ at each charge or discharge relaxation step has been calculated based on GITT data (**Figure 3.18B**). The coefficients were in the range from 10^{-18} to 10^{-16} cm^2 s^{-1} within the potential window of 2.2–4.4 V (vs. Na^+/Na) are comparable to those of known polyanionic compounds, such as $Na_{0.9}FePO_4$ ($8.63*10^{-17}$) and $Na_3V_2(PO_4)_3$-C (NASICON, $2*10^{-15}$).[34] Similar coefficients were obtained from GITT data under the same test conditions for the $Na_{1.2}Fe_{1.2}PO_4F_{0.6}$_S and _S/C electrodes, but lower Na exchange number and serious polarization can be

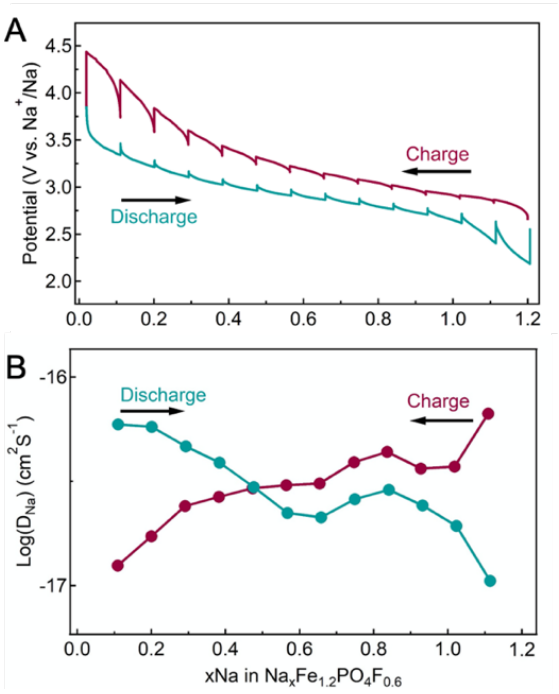

Figure 3.18 Na^+ diffusion and phase reversibility over charge and discharge process of $Na_{1.2}Fe_{1.2}PO_4F_{0.6}$_M. (A) GITT curves for the first cycle and (B) diffusion coefficient of Na^+ calculated from the GITT curves as a function of number of Na in the material.

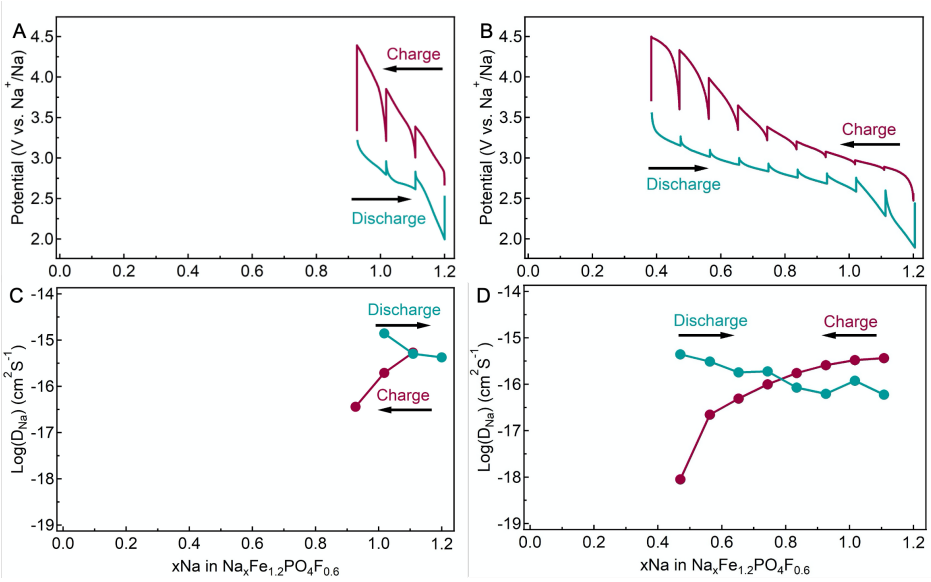

Figure 3.19 (A) and (B) GITT curves for the first cycle and (C) and (D) diffusion coefficient of Na^+ calculated from the GITT curves as a function of number of Na in the material for $Na_{1.2}Fe_{1.2}PO_4F_{0.6}$_S and _S/C, respectively.

seen from their potential profiles (**Figure 3.19**). This indicates the inefficient Na diffusion in the _S and _S/C electrodes, which could be explained by the inactive Na sites in crystal structure of the stable phase.

To have a further insight of Na^+ extraction and insertion processes, *in situ* electrochemistry - XRD survey was performed. The main diffraction region and the corresponding potential profiles of the first two charge-discharge cycles at C/32 are displayed in **Figure 3.20**. Most of the diffraction peaks gradually shift to the higher 2Theta values when charging to 4.4 V (vs. Na^+/Na), and the opposite process occurs when discharging to 1.7 V, which can be explained by structural re-arrangement and compaction during extraction, and vice-versa. The good structural reversibility is evidenced by the reversible evolution of peaks, which shift

back to the pristine position in discharged state. The good structural reversibility and stability demonstrate that the structure of $Na_{1.2}Fe_{1.2}PO_4F_{0.6}$_M is not remarkably impacted by the insertion and extraction of Na^+ upon cycling, in good agreement with its superior capacity cycling stability (**Figure 3.17A and D**).

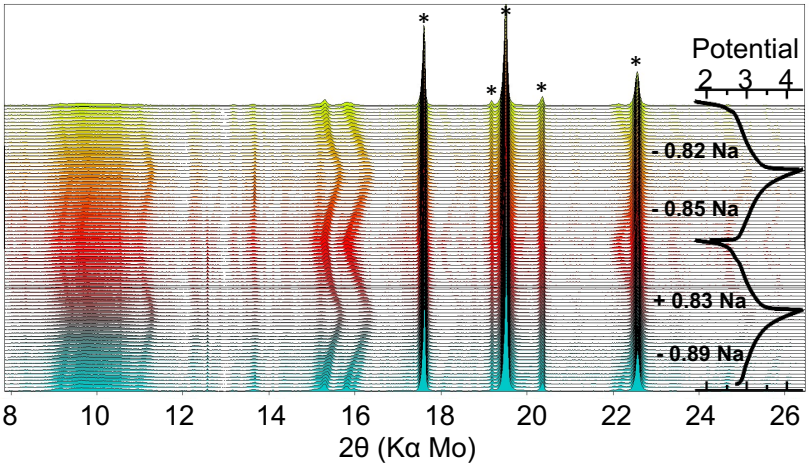

Figure 3.20 *In situ* XRD pattern evolution and corresponding potential profiles. Peaks from Al and Cu foil are marked by asterisks and one extra peak at 12.6 degree can be indexed to Na_2CO_3, due to the contamination of Na in the cell.

3.3 Outlook and significance of this work

Metastable phases and materials for energy applications remain sporadically in depth studied yet seem to hold great promises.[165] The poor exploration comes from the fact it is usually considered to work with the stable thermodynamic phases as these are also much easier to prepare. It is also typically assumed that the thermodynamically stable phases may also be the ones with best electrochemical performances, as it is indeed the case for most positive or negative battery electrode materials. However, metastable materials are also known to outperform their stable counterparts.[165] What is furthermore essential is the richness of the multiple possibilities here, hence the multitude of the reaction channels a process can follow before reaching its lowest energy equilibrium might be endless (**Figure 3.1B**). Our work analyses only a few of these, available in the simple chemical, yet complex compositional and phases diagram of Na-Fe-PO_4-F. With a total of 14 materials studied in this work, out of which 6 are in the thermodynamically stable state, we find particularly enhanced electrochemical activity of metastable phases.

The choice of $Na_{1.2}Fe_{1.2}PO_4F_{0.6}$ composition was guided by theoretical capacity estimates, being the composition with equimolar Na and Fe content, with thus redox of Fe being possible to compensate by Na cation extraction, while also optimizing the Fe - PO_4 - F ratio to decrease the overall molecular weight. While the Fe to PO_4 ratio was fixed in our work, it can be further presumed that additional compositions can be accessed by also altering this stoichiometry. Thus, the Na and Fe-rich (as compared to PO_4 equivalents) $Na_{1.2}Fe_{1.2}PO_4F_{0.6}$ polyanionic framework was selected amongst all as central interest to understand the fundamentals of its electrochemistry and structure – composition – property relationship. Within this same composition, we have accessed and analysed as many as

9 phases and show remarkable differences in characteristics, impacting on their electrochemical properties significantly. Further the electrochemistry and structural analysis shows a complex interplay between the Na^+ diffusion pathways in disordered structures, unit cell size, electrical conductivity and material morphology.

In terms of energy density, the best performing $Na_{1.2}Fe_{1.2}PO_4F_{0.6}$_M material in this work exhibits a practical energy density at the material level in the 400 Wh kg^{-1} range, marked at a leading position when compared to other iron phosphate-based cathode materials for SIBs in literature (**Figure 3.16C**). It is to be highlighted that for the many of the reported materials carbon coating, particle size control and ball milling treatment techniques have been employed to improve the electrochemistry performances (**Figure 3.16C**). The $Na_{1.2}Fe_{1.2}PO_4F_{0.6}$_M material is already at the forefront, being limited only by its moderate power performances given the absence of carbon coating. This later will require as ingenious as the material itself approaches, as it should be based on low temperature methods, so that the metastable phase(s) and activity are preserved. Although this particular metastable phase is still not well understood at present, in-depth structural and electrochemical studies are underway to unravel the complexity of the fundamental science for this promising cathode material, as it is often the case for new materials.

3.4 Experimental section

3.4.1 Sample preparation

The $Na_{0.6+x}Fe_{1.2}PO_4F_x$ (x=0, 0.2, 0.4, 0.6, 0.8 and 1) materials were synthesized via a solid-state reaction assisted by high-energy ball milling. The stoichiometric amounts of Na_2CO_3 (≥99.5%, Sigma-Aldrich), $NH_4H_2PO_4$ (99+%, Acros Organics), $FeC_2O_4 \cdot 2H_2O$ (99%, Sigma-Aldrich) and NaF (99%, Alfa Aesar), around 3.6–4 g in total, were first ball milled at 30 Hz for 20 min three times with 20 min pause under Ar atmosphere, using one stainless steel ball (25 mm diameter) in a 50 mL jar and high-energy miller (Ball Mill BM500, Anton Paar). To obtain very fine powder precursors, the jars were opened and the caked precursors were scraped down using a spatula, followed by ball milling at 15 Hz for 10 min under Ar atmosphere. For the carbon coated samples, 6 wt.% (referring to the total amount of reactants) of stearic acid (extra pure, Acros Organics) was used as carbon source. Then, the precursors were transferred into alumina crucibles and annealed at various temperatures for different annealing times under Ar flow (99.99% in purity) in a tube furnace with flange sealing system. The initial heating rate was 2 °C min^{-1} whereas the cooling process natural. All samples were transferred into a glovebox (MBraun, <0.1pmm O_2 and H_2O) with minimal exposure to air and stored therein for further analyses.

3.4.2 Physicochemical characterizations

Powder XRD (STOE DARMSTADT StadiP Transmission diffractometer system) using Mo K_α radiation (λ = 0.71073 Å) was employed to confirm crystalline phases of the commercial starting

materials, the ball milled precursors and the synthesized samples. FullProf Suite software was used for PXRD indexing and refinement of $Na_{1.2}Fe_{1.2}PO_4F_{0.6}$_S and FOX software for its structure solution.

TGA-DSC-MS was performed with N_2 as carrier gas at a heating rate of 10 °C min^{-1} on a Mettler Toledo TGA/DSC 3+ STARe System, using alumina containers. Full-spectrum direct-reading inductively coupled plasma emission spectrometry (ICP, SPECTRO BLUE SOP) analysis was performed to confirm atomic ratio at Hunan University in China. ^{57}Fe Mössbauer spectra were recorded at room temperature in transmission geometry mode with a constant acceleration mode conventional Wissel Mössbauer spectrometer equipped with a ^{57}Co (Rh) radioactive source, a Reuter Stokes proportional counter detector and a CMCA-550 multichannel analyzer. All isomer shifts in Mössbauer spectra are given respective to α-Fe. Fourier transform infrared spectroscopy (FT-IR) was carried out on pristine powders and spectra were recorded with a Shimadzu FTIR-8400S spectrophotometer.

Brunauer-Emmett-Teller technique (BET) was used to analyse Nitrogen-sorption isotherms and pore size distribution of the samples on Micromeritics ASAP 2020. The microstructure and morphology analyses were characterized by Scanning Electron Microscopy (SEM, JEOL JSM 7600F) and Energy dispersive X-ray spectroscopy (EDX, JEOL JSM 7600F), as well as Transmission Electron Microscope (TEM, Titan G2 60-300) and EDX (Titan G2 60-300) after dispersing the samples on holey carbon film on copper grids at Central South University in China.

In situ XRD patterns were recorded using a STOE Stadi P diffractometer operated in transmission mode, equipped with a Mo anode X-ray source (Kα radiation, operating at 50 kV − 40 mA) and Dectris Mythen 1K strip detector and details can be found in **Figure 3.21**. Measurements were performed with a simple holder able to accommodate

an in-house *in situ* coin cell. Firstly, one hole (6 mm diameter) is drilled in the centre of both cases of the SS316 coin cell as well as the spacer (8 mm diameter hole). Al and Cu foils (thickness 25 µm) were fixed in the inner side of the cases with epoxy and used as X-ray partially permeable windows for positive and negative cases, respectively. The working electrode was prepared by mixing $Na_{1.2}Fe_{1.2}PO_4F_{0.6}$_M, Super P and PTFE with a composition ratio of 70:25:5 wt.% (10.4 mg in total). This composite was then pressed at 8 tons on Al mesh current collector. Sodium metal disk was used as negative electrode, one sheet of glassfibre (Whatman, GF/D) as separator and $NaClO_4$ dissolved in a 1:1 (v:v) mixture of ethylene carbonate (EC) and diethyl carbonate (DEC) containing 5 vol% fluoroethylene carbonate (FEC) as electrolyte.

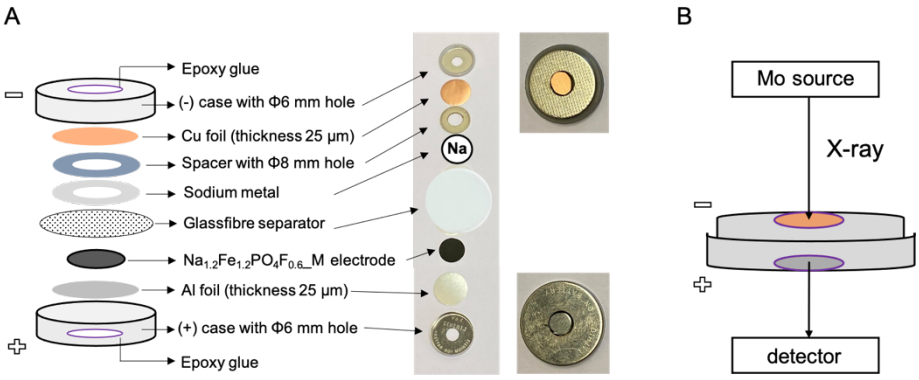

Figure 3.21 (A) Schematic representation and optical image of the in-house coin-cell used for in-situ XRD measurements. (B) Schematic illustration of XRD measurement according to transmission configuration used in this work (image reprinted from other work).[196]

3.4.3 Electrochemical cell assembly and measurements

The working electrodes were fabricated by dry grinding the samples (70 wt.%) with super P carbon (SP) as conductive agent (25 wt.%) and Poly tetra fluoroethylene (PTFE, powder, Sigma-Aldrich) as binder (5 wt.%), followed by pressing certain amount of powder onto coin cell case (CR2032, SS-316 steel). The typical mass loading was of approximately 1–1.5 mg active material (6–9 mg per square-cm). The electrochemical tests were performed in half-cells (CR2032 coin cell format) with metallic Na as counter and reference electrode and one sheet of glassfibre (Whatman, GF/D) as separator. $NaClO_4$ dissolved in a 1:1 (v:v) mixture of ethylene carbonate (EC) and diethyl carbonate (DEC) containing 5 vol% fluoroethylene carbonate (FEC) was used as electrolyte. The assembly was carried out in an Ar filled glove box (MBraun, <0.1pmm O_2 and H_2O).

Galvanostatic charge-discharge tests were performed for the cells on Neware battery testing system at ambient temperature. Galvanostatic intermittent titration technique (GITT) was carried out by charging or discharging at a current pulse of C/80 for 6 h followed by relaxation at open circuit for 24 h at each step on BioLogic – Battery Cycling and Testing systems at ambient temperature. Schematic diagram of a single-step GITT experiment is shown in **Figure 3.22**.

Na^+ diffusion coefficients (D_{Na}) were determined for each step from GITT. The change in the steady-state voltage E_s is obtained by subtracting the original potential (E_0) from the steady-state potential (E_s). The process of the chemical diffusion is assumed to obey Fick's second law of diffusion. If sufficient small currents are applied for short time intervals, then $dE/d\sqrt{t}$ can be considered linear, as well as the coulometric titration curve over the composition range involved in that step. With these conditions, the equation of D_{Na} can be simplified to:**[197]**

$$D_{Na} = \frac{4}{\pi t}(\frac{n_m V_m}{S})^2(\frac{\Delta E_s}{\Delta E_t})^2$$

Here, t (s) is the duration of the current pulse; n_m (mol) is the number of moles; V_m $(cm^3\ mol^{-1})$ is the molar volume of the electrode; S (cm^2) is the contact area between the electrode and electrolyte; ΔE_s (V) is the steady-state potential change, due to the current pulse and ΔE_t (V) is the potential change during the constant current pulse, eliminating the IR drop. In this study, the V_m (65.5 $cm^3\ mol^{-1}$) of the stable $Na_{1.2}Fe_{1.2}PO_4F_{0.6}$_S, calculated from its unit cell parameters and structure solution formula, was used as an approximation and the specific surface area (28.2 m^2 g^{-1}) and mass loading of the electrode were applied to estimate S for the D_{Na} calculation of $Na_{1.2}Fe_{1.2}PO_4F_{0.6}$_M.

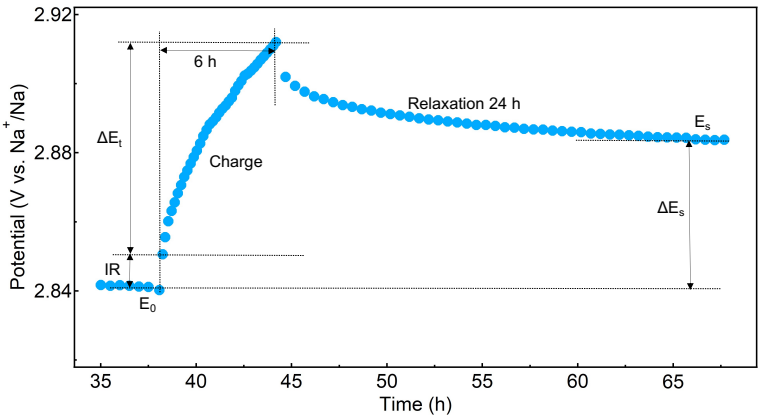

Figure 3.22 Schematic diagram of a single-step GITT experiment for $Na_{1.2}Fe_{1.2}PO_4F_{0.6}$_M at the current density of C/80 (2 mA g^{-1}).

CHAPTER 4 – Unlocking the Electrochemistry and Activation Mechanism in Iron-rich $Na_{0.6}Fe_{1.2}PO_4$ Phase

Abstract

SIBs are considered as the immediate sustainable alternative to LIBs. To reduce the competitiveness gap, improved performances and better understanding of Na storage, especially in new phases based on sustainable materials, are further required. In this work, we provide advanced investigation of the structure and the electrochemistry of a peculiar off-stoichiometric iron-rich phase ($Na_{0.6}Fe_{1.2}PO_4$) for Na storage. An interesting electrochemical activation phenomenon is described and contrary to conventional ageing processes, it is found to enhance significantly the energy and power rate performances.

4.1 Introduction

SIBs as a sustainable and cost-effective alternative technology, are attracting increasing attention[16, 17], also because the similarity to the LIB technology, progressed SIBs to an already commercial level.[198] Whereas there is major progress achieved on SIB anode materials, cathode materials remain one of the blocking elements on the way of progress. The success story of olivine $LiFePO_4$ has motivated researchers to study the electrochemistry of the Na equivalent, $NaFePO_4$ phases.[199] However, opposite to olivine $LiFePO_4$, the thermodynamically stable phase of $NaFePO_4$ is the maricite, which lacks of practical electrochemical activity.[28, 29] Improvements have been attained by nano-structuration, or by working with the metastable Na-olivine phase, made via ion exchange processes from the olivine $LiFePO_4$. Nevertheless, the rate capabilities remain unsatisfactory, attributed to low electrical conductivity and slower diffusion of larger Na ions in the host materials.[31, 32, 195] Other Fe-based phosphate cathode materials such as $Na_2FeP_2O_7$, $Na_4Fe_3(PO_4)_2(P_2O_7)$ and $Na_3Fe_2(PO_4)_3$ have been also proposed and show promising performances.[189, 190, 200] Additionally, the class of off-stoichiometric Fe-phosphates ($Na_{3.12}Fe_{2.44}(P_2O_7)_2$, $Na_{3.32}Fe_{2.34}(P_2O_7)_2$, $Na_{0.71}Fe_{1.07}PO_4$)[106, 160, 201] provide flexibility in tuning the composition and the properties, enriching this library with novel cathode candidates.[27]

In a recent report, Yamada proposed a peculiar Fe-rich sodium phosphate phase, the $Na_{0.6}Fe_{1.2}PO_4$, to be of great interest as cathode material for Na storage.[107] This material was found to operate at an average potential of 3 V (vs. Na^+/Na), delivering a reversible capacity of 85 mAh g^{-1} (for a theoretical of 91 mAh g^{-1}) at a rate of C/20 (the first cycle performance is reproduced in **Figure 4.1A**. However, high

polarization (and thus low energy efficiency), limited power performances, and rapid capacity fade were reported, calling for further improvements along with additional structural and mechanistic insight.

Herein, nano-sized $Na_{0.6}Fe_{1.2}PO_4$ phase was synthesized and enhanced electrochemical performances are attained. The side reactions at high potential are avoided, polarization is considerably reduced, and better reversibility is obtained, as compared with the initial report (**Figure 4.1B**).[107] Through advanced analysis we provide novel insight into the physico-chemical and electrochemical properties of this peculiar material. The galvanostatic charge-discharge behaviour is evaluated in different

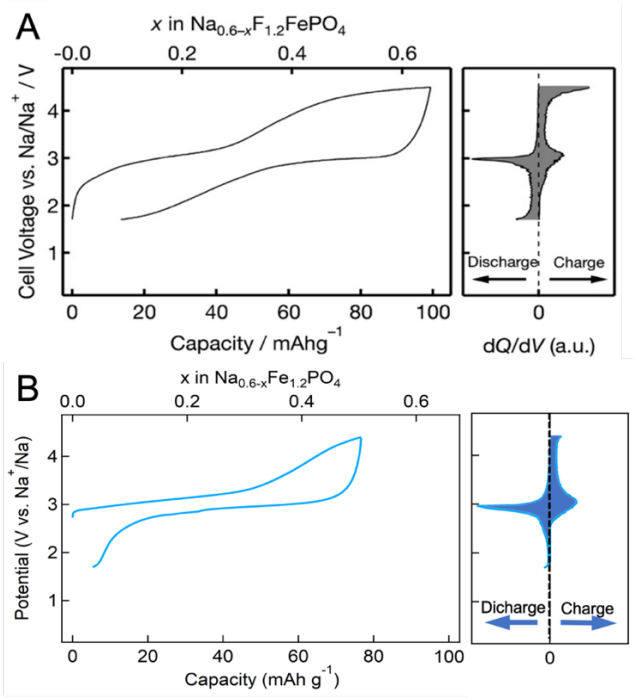

Figure 4.1 Comparison of first cycle performance for $Na_{0.6}Fe_{1.2}PO_4$ (A) as reported by Yamada using $NaPF_6$ in PC with 2 vol% FEC as electrolyte, reprinted with permission from Reference [107]; and (B) the material synthesized in this work using $NaClO_4$ in EC/EMC with 5 vol% FEC as electrolyte.

electrolyte formulations and optimal conditions are provided. We also detail an exotic electrochemical activation mechanism upon extended galvanostatic cycling, characterized by gradual appearance and elongation of a redox plateau at 3.8 V (vs. Na^+/Na) accompanied by capacity increase. The activation phenomenon is independent of the electrolyte used and current density applied, making it an interesting and promising cathode material candidate worth of further investigation of pristine and activated phases.

4.2 Results and discussion

4.2.1 Characterizations

Intrigued by the interesting properties of this off-stoichiometric iron-rich material proposed by Yamada, but also by the noticeable limitations highlighted in the original work, we aimed at further investigations and potential performance improvements.[107] The $Na_{0.6}Fe_{1.2}PO_4$ was synthesized by following the reported protocol and it is also detailed in the Experimental Section. The chemical composition was analysed via inductively coupled plasma emission spectrometry and the obtained Na, Fe and P elemental ratio was found similar to the theoretical values (**Table 4.1**), implying no element loss during synthesis. The powder X-ray diffraction (PXRD) pattern (**Figure 4.2A**) was indexed to a similar unit cell ($a = 14.86$ Å, $b = 6.43$ Å, $c = 10.32$ Å, $\alpha = \beta = \gamma = 90°$ and $V = 985.6$ Å^3) as of the reported one (**Table 4.2**), suggesting the successful reproduction of the results.[107]

The Mössbauer spectrum is shown in **Figure 4.2B** and the estimated parameters from fitting of isomer shift δ, quadrupole splitting Δ, half width of peak Γ, and absorption area intensity ratio S are summarized in **Table 4.3**. The observed spectrum can be fitted to four doublets. The presence of three types of Fe^{2+} sites with large values of δ (>1.1 mm s^{-1}) and Δ (>1.9 mm s^{-1}) associated to octahedral coordination suggests complex local environment of Fe^{2+} ions in the crystal structure along with structural distortion. One doublet with small value of δ (=0.64 mm s^{-1}) and Δ (=0.24 mm s^{-1}) indicates the presence of traces of Fe^{3+} which could be due to surface oxidation of the sample.

Table 4.1 Atomic ratio of Na, Fe and P in $Na_{0.6}Fe_{1.2}PO_4$ measured by full-spectrum direct-reading inductively coupled plasma emission spectrometry (ICP, SPECTRO BLUE SOP).

Sample	Elemental ratio (Na:Fe:P)	
	Nominal	ICP
$Na_{0.6}Fe_{1.2}PO_4$	0.6:1.2:1.0	0.61:1.23:1.00

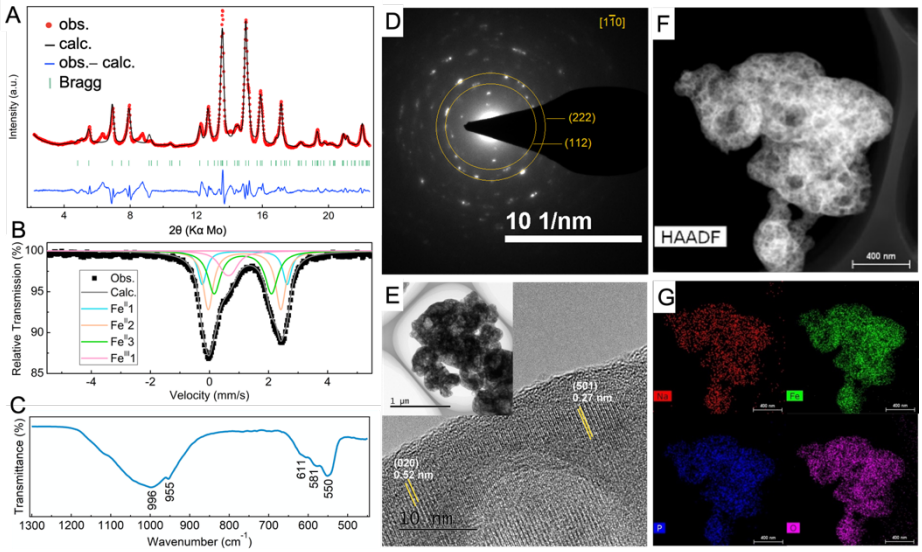

Figure 4.2 (A) PXRD pattern and the Rietveld refinement; (B) Room-temperature Mössbauer spectrum and fitting results; (C) FTIR spectrum; (D) SEAD image; (E) HRTEM with inset of TEM images; (F) TEM-HAADF; and (G) EDX elemental mapping for the synthesized $Na_{0.6}Fe_{1.2}PO_4$ phase.

Table 4.2 Comparison of unit cell parameters from PXRD indexing results in Reference 1 and this work.

$Na_{0.6}Fe_{1.2}PO_4$	a	b	c	α, β, γ	V
Reference	14.82 Å	6.40 Å	10.32 Å	α = β = γ = 90°	978.83 Å^3
This work	14.86 Å	6.43 Å	10.32 Å	α = β = γ = 90°	985.60 Å^3

Table 4.3 ^{57}Fe Mössbauer parameters obtained by fittings for $Na_{0.6}Fe_{1.2}PO_4$. Isomer shift (δ) are given with respect to metallic α-Fe. ΔE_Q = quadrupole splitting. Γ/2 = half width of the lines.

Site	δ (mm s^{-1})	ΔE_Q (mm s^{-1})	Γ/2 (mm s^{-1})	S (%)
Fe(II)	1.19	2.87	0.17	18
Fe(II)	1.18	2.45	0.23	47
Fe(II)	1.12	1.94	0.25	33
Fe(III)	0.64	0.24	0.28	12

Infrared spectroscopy was used to analyse the characteristic intramolecular vibration bands of the PO_4 group in $Na_{0.6}Fe_{1.2}PO_4$ (**Figure 4.2C**). The symmetric ν_1 and asymmetric ν_3 stretching modes appear in the high-wavenumber region (850–1200 cm^{-1}), while the intramolecular bending modes (ν_2 and ν_4) occur between 700 and 500 cm^{-1} in the spectrum.[175, 178, 202] Note that the bands in the spectrum are broadened and low-resolved, explained by the difference in atomic distances, corroborating the structural disorder.[175, 181]

The transmission electron microscopy (TEM) analysis reveals additional insight into the morphology, crystallinity and elemental distribution. The selected area electron diffraction (SAED) pattern (**Figure 4.2D**) displays interplanar rings diffraction spots with ≈ 0.25 and ≈ 0.3 nm spacing, corresponding to the (112) and (222) planes, respectively. The high-resolution TEM (HRTEM) image (**Figure 4.2E**) shows the lattice fringes in $Na_{0.6}Fe_{1.2}PO_4$ with lateral d-spacings of ≈0.52 and ≈0.27 nm, matching the (020) and (501) planes from PXRD indexing results, respectively. Morphology analysis reveals a porous nano-sized particle morphology, with small agglomerates (inset of **Figure 4.2E**). The porous microstructure of the particles can be also observed in the high-angle

annular dark-field (HAADF) image in **Figure 4.2F** and the elemental mapping in **Figure 4.2G** further verifies uniform elemental distribution, indicating good phase homogeneity.

4.2.2 Electrochemical properties

We next focus on electrochemical analysis and discussion. It should be first noted that the galvanostatic charge-discharge performance in the initial report (**Figure 4.1A**), was accompanied by large polarization and electrolyte decomposition at high potential. This later, is visible by the appearance of a plateau at high potential during charge (the dQ/dV plot displaying an irreversible anodic current above 4V vs. Na^+/Na). Although no additional discussion was provided by the authors, we believe this could be the main reason accounting for fast capacity decay upon cycling. To verify this, we also tested same electrolyte formulation (1 mol $NaPF_6$ dissolved in propylene carbonate -PC with 2 vol% fluoroethylene carbonate - FEC). Our analysis also revealed low first cycle Coulombic Efficiency (CE), assigned to anodic decomposition (**Figure 4.3**). According to these, we thus first screened a series of electrolytes to find optimal conditions for stable cycling and high CE.

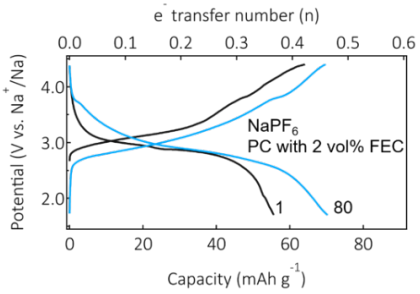

Figure 4.3 Potential vs. capacity profiles for the $Na_{0.6}Fe_{1.2}PO_4$ electrode using $NaPF_6$ in PC with 2 vol% FEC.

The best performing electrolytes found are the following - $NaClO_4$ in EC/DEC with 5 vol% FEC; $NaClO_4$ in EC/DEC; and $NaPF_6$ in EC/DEC. Cycling in these electrolytes were free of the high potential plateau, with initial capacities around 70 mAh g^{-1}, corresponding to 0.5 Na equivalent extraction at a rate of C/20 (1C rate corresponds to 91 mA g^{-1}, **Figures 4.4 and 4.5**). The cycling stability and rate capability are also significantly improved. However, the unexpected feature was the gradual capacity increase, and more intriguing, the appearance and elongations of an additional reversible process at around 3.8 V vs. Na^+/Na (**Figure 4.4A and B**) accompanying this process.

Consequently, we performed additional long-term galvanostatic cycling tests at low and high C-rates. For example, after 110 cycles at C/20, the capacity reaches 110 mAh g^{-1}, exceeding the theoretical capacity of 91 mAh g^{-1} (0.6 Na exchange per formula unit). Longer-term charge-discharge cycling performance at 1C and 2C were also found to be excellent (while taking into account the instability of Na-metal in the used carbonate-based electrolyte formulation). The potential profile features are significantly changed after 1000 cycles (**Figure 4.4C**), compared to the initial cycles at same rate. The shape and length of the 3.8 V plateau is similar to one attained C/20. For fast cycling cells, the capacity is stabilized after about 1000 cycles, with 97.3 and 75.5 mAh g^{-1} delivered at 1C and 2C, respectively, after 2000 cycles (**Figure 4.4D**).

The power rate capability was also been tested after the 2,000 cycles test (**Figure 4.4E**) and compared to the pristine material (**Figure 4.4F**). It shows significantly improved performance with 60 mAh g^{-1} retained at 5C, whereas a much lower rate of C/5 is required to reach a similar capacity for the pristine electrode material. The metrics of the thus obtained activated phase outperform many of the reported iron phosphate cathode materials for SIBs (**Figure 4.4G**).

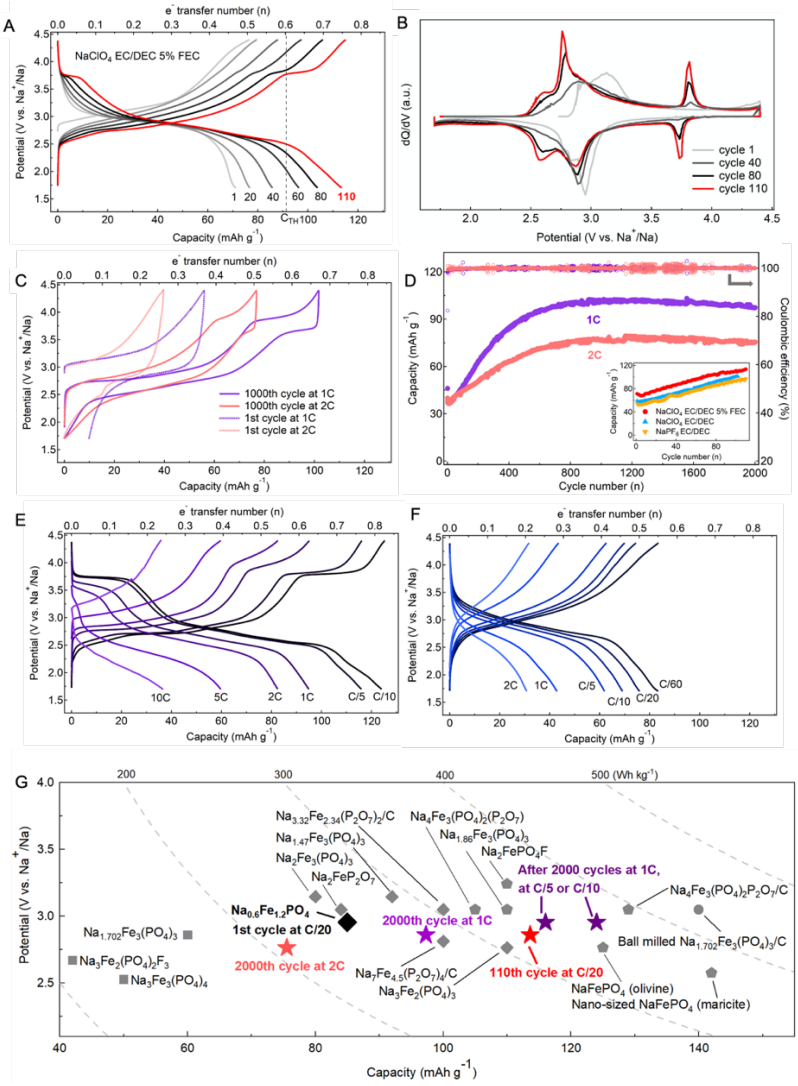

Figure 4.4 (A) Potential vs. capacity profiles and (B) corresponding dQ/dV curves at C/20 (C_{TH}=91 mAh g^{-1}) at various cycles for the $Na_{0.6}Fe_{1.2}PO_4$ electrode using $NaClO_4$ in EC/DEC with 5 vol% FEC. (C) Potential vs. capacity profiles of the first and 1000th cycles at 1C and 2C and (E) corresponding long-term cycling stability and inset for various electrolytes at C/20. Potential vs. capacity profiles at different C-rates of one typical cycle (three cycles at each C-rate) (E) after activation of the 2000 cycles at 1C and (F) from initial cycles. (G) Energy density comparison (performances considered at the material level) of various iron phosphate-based cathode materials for SIBs.[33, 35, 107, 160, 182-185, 187-194]

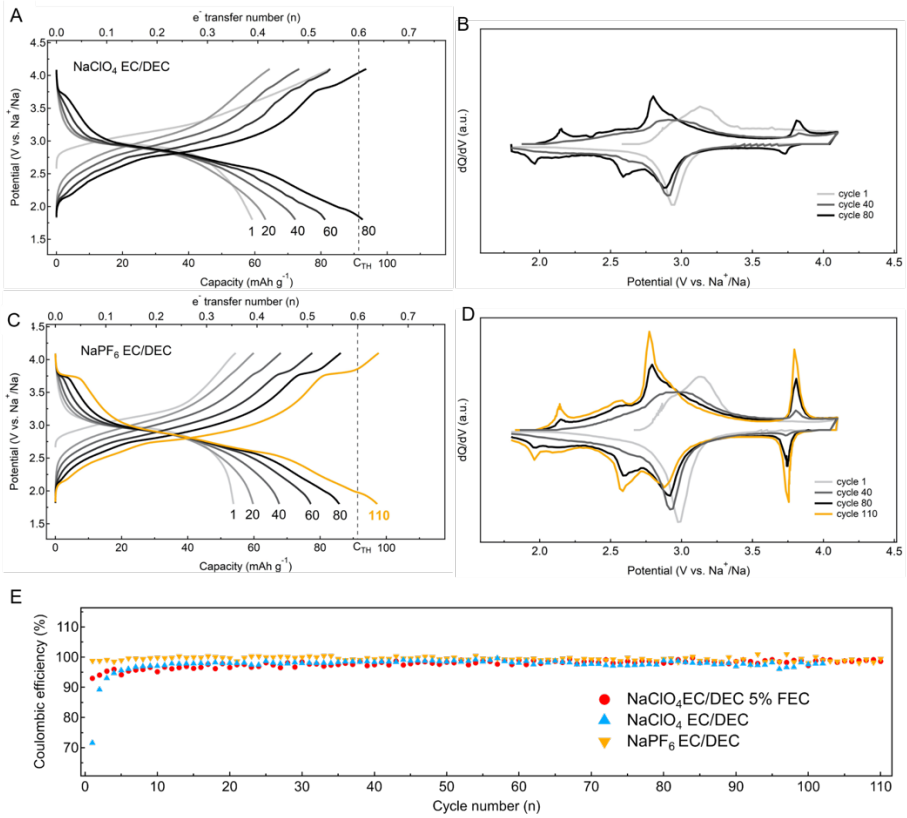

Figure 4.5 (A, C) Potential vs. capacity profiles and (B, D) corresponding dQ/dV curves at C/20 at various cycles for the $Na_{0.6}Fe_{1.2}PO_4$ electrode using another two electrolytes (1mol $NaClO_4$ in EC/DEC (V/V 1:1) and 1 mol $NaPF_6$ in EC/DEC (V/V 1:1)) for the test in a narrower potential window range of 1.8–4.1 V (vs. Na^+/Na) to avoid serious electrolyte decomposition. To note that the cells tested using the $NaClO_4$ in EC/DEC as electrolyte failed before 110 cycles. (E) Coulombic efficiency vs. cycle number plots for the electrode using $NaClO_4$ in EC/DEC with 5 vol% FEC, $NaClO_4$ in EC/DEC and $NaPF_6$ in EC/DEC as electrolyte.

An electrochemical activation processes of this type remains unusual, being rarely encountered in literature, and the origins could be various in nature, ranging from anion intercalation into the conductive carbon (however noting that the redox potential is low for this process to be

considered here);[199, 203] or in-situ electrochemical fluorination as already reported, but only in oxide materials.[204, 205] To unveil the origins, we first run a series of control experiments. A blank test with only Super P carbon and polytetrafluoroethylene (PTFE) binder were cycled and no capacity increase, or redox potential profile change could be noticed (**Figure 4.6**), ruling out any significant contribution to capacity from the coin cell construct, conductive carbon or binder. To test whether the activation process is enabled by a high potential anodic process, another control experiment was run. Using the $NaClO_4$ in EC/DEC with 5 vol% FEC as electrolyte, the cell was first charged in constant current (CC, C/20) regime, followed by a constant voltage (CV) hold at 4.4 V for 48 hours, and then discharged to 1.7 V at C/20 (**Figure 4.7A and B**). Continuous cycling using this protocol revealed a similar behaviour as for regular CC charge-discharge tests (**Figure 4.4A**) with the 3.8 V redox not activated at early stages of cycling (**Figure 4.7A**).

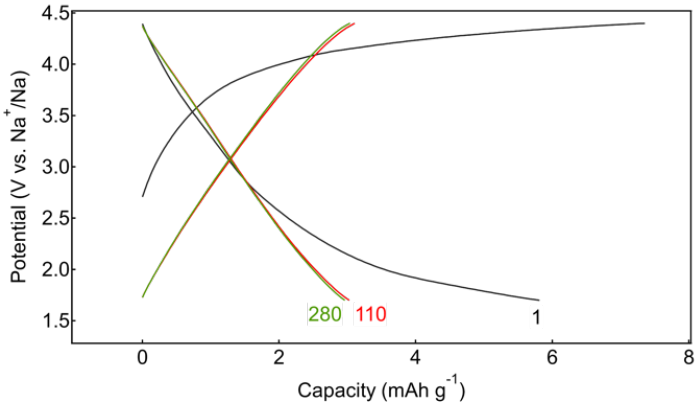

Figure 4.6 Potential vs. capacity profiles for blank test. The electrode containing only super P (83%) and PTFE (17%) has been tested at 1 mA g^{-1} during the first two cycles, followed by at 5 mA g^{-1}. It took 167 and 373 h for 110 and 280 cycles, respectively.

The 3.8 V redox appears after approximately 20 cycles at C/90, 40 cycles at C/20 (**Figures 4.7C and 4.4A**), or around 200 cycles at 1C (Not shown). To be mentioned that even before the clear emergence of this process, there is a steady increase in the capacity, accompanied by lowering the cell polarization and increase in CE (**Figures 4.4A, 4.4D and 4.5**). The dQ/dV analysis reveals a much more complex mechanism. The continuous evolution of redox processes at 3 V can be seen at first cycles, further evolving into a set of redox peaks at 2.6 and 2.8 V (**Figures 4.4B**). Along with this, the intensity of the peaks at 3.8 V increases. A similar trend was also observed for other electrolytes, with additional features being also observed (refer to **Figure 4.5** for a detailed discussion).

The analysis of data presented above implies that any potential anodic decomposition of the electrolyte, or other elements present in the cell are not the direct cause (although may be necessary) of the capacity increase or the appearance of the 3.8 V plateau. The activation process also seems also be time and desodiation/sodiation cycles number dependent. A gradual structural modification within the pristine $Na_{0.6}Fe_{1.2}PO_4$ phase could be one explanation, however, this does not support the fact that the theoretical capacity of 0.6Na is surpassed.

Next, we turned our attention to the chemical environment and found that all cells containing reactive fluoride species (e.g. PF_6^-, FEC) show rapid and obvious capacity increase and development of the 3.8 V plateau from pristine $Na_{0.6}Fe_{1.2}PO_4$ (**Figures 4.4A and 4.5C**). In the absence of these, electrochemical activation of $Na_{0.6}Fe_{1.2}PO_4$ was also observed, assigned to fluoride generation from the anodic (or cathodic) decomposition of PTFE binder (**Figure 4.5A**). In absence of any fluoride precursors (e.g., no PTFE, and using $NaClO_4$ in EC/DEC as electrolyte), insignificant activation was observed, implying that fluoride has an important role here (whereas not excluding involvement of other anionic

species). Partial structural re-organization accompanied by fluoride insertion into the lattice (yielding a new composition, of $Na_{0.6+x}Fe_{1.2}PO_4F_x$ stoichiometry) can be thus accounted for the observed electrochemical evolution with cycling.

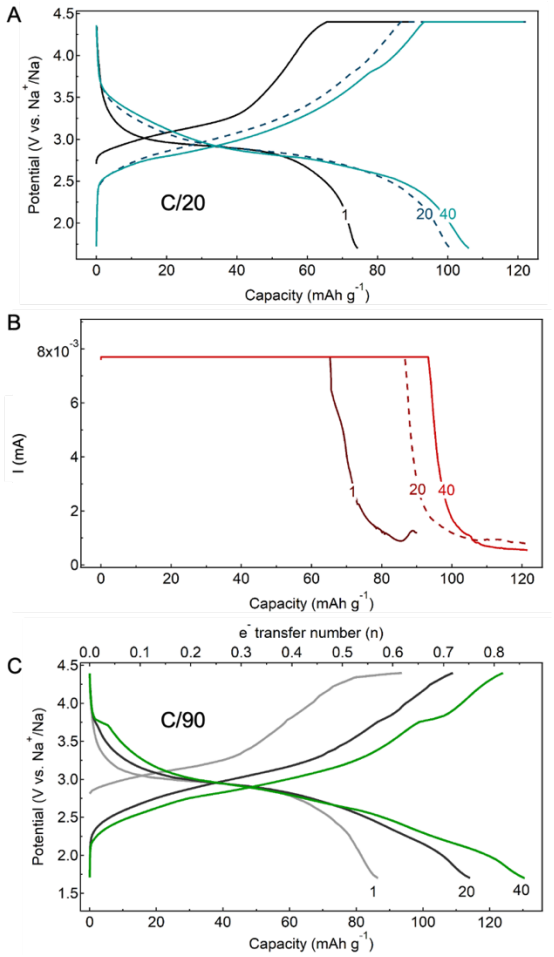

Figure 4.7 (A) Potential vs. capacity profiles for the $Na_{0.6}Fe_{1.2}PO_4$ electrode using $NaClO_4$ in EC/DEC with 5 vol% FEC as electrolyte and tested under charge in constant current constant voltage (CC-CV) mode with CV at 4.4 V for 48 hours and then discharge to 1.7 V at C/20 and (B) corresponding current vs. capacity profiles during charge process. (C) Potential vs. capacity profiles at C/90.

In an attempt to unravel the electrochemical activation mechanism, in situ and ex situ XRD analyses were performed. In situ PXRD data were collected during the charge and discharge processes at C/30 for the first (1st) and second (2nd) cycles (**Figure 4.8A**). During the charge process of each cycle, the main peaks shift to higher 2Theta angles and the process is reversible upon discharge. No significant diffraction pattern changes can be seen after two cycles. It means good structure stability and reversibility of the electrode at this early cycling stage. In contrast, new patterns were shown for the activated electrode after 2000 cycles at 1C by ex situ XRD analysis (**Figure 4.8B**). It indicates that the activation induced the phase transformation of the $Na_{0.6}Fe_{1.2}PO_4$ so as to facilitate the diffusion of Na ions and anionic species. As a result, the newly formed electrode exhibits excellent cycling performance and rate capability (**Figure 4.4**).

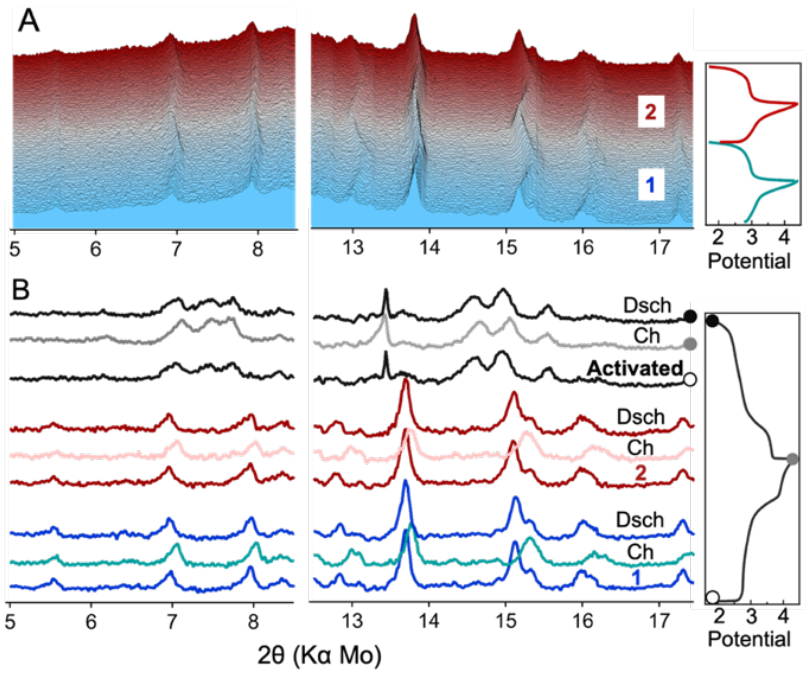

Figure 4.8 (A) *In situ* XRD patterns and corresponding potential profiles for the $Na_{0.6}Fe_{1.2}PO_4$ electrode at the first and second cycles. (B) XRD patterns for before the cycle, charge (Ch) and discharge (Dsch) states from the *in situ* XRD at the first (blue) and second (red) cycles and ex situ XRD for activated electrodes collected from disassembled coin cells after test at 1C for 2000 cycles (red).

4.3 Conclusions

The $Na_{0.6}Fe_{1.2}PO_4$ material prepared and analysed in this work not only shows improved electrochemical performances, but also a peculiar electrochemical activation process, appearance of a redox potential of as high as 3.8V vs. Na^+/Na. Whereas it is not possible at this stage to clarify the structure nor the mechanism behind its formation, it may be interesting to obtain the information and attempt further exploration. Despite these fundamental questions remained, the material we explore in this work achieves reversible capacities as high as 110 mAh g^{-1}, displays excellent rate capability, and stability on long long-term cycling, outperforming many of this type of cathode materials in literature (**Figure 4.4G**). The results in this work are encouraging to merit further investigation of this low-cost, safe and eco-friendly cathode material.

4.4 Experimental section

4.4.1 Sample preparation

The $Na_{0.6}Fe_{1.2}PO_4$ was synthesized via a solid-state reaction with precursors processing by high-energy ball milling. The stoichiometric amounts of Na_2CO_3 (≥99.5%, Sigma-Aldrich), $NH_4H_2PO_4$ (99+%, Acros Organics) and $FeC_2O_4 \cdot 2H_2O$ (99%, Sigma-Aldrich), around 3.6 g in total, were first ball milled at 30 Hz for 20 min three times with 20 min pause under Ar atmosphere, using one stainless steel ball (25 mm diameter) in a 50 mL jar and high-energy miller (Ball Mill BM500, Anton Paar). To obtain very fine powder precursors, the jars were opened and the caked precursors were scraped of the walls using a spatula, followed by and additional ball milling step at 15 Hz for 10 min under Ar atmosphere. The precursors were transferred into alumina crucibles and annealed at 550 ºC for 12 h under Ar flow (99.99% in purity) in a tubular furnace. The heating rate was 2 °C min^{-1} whereas the cooling was left to proceed naturally. The samples were transferred into a glovebox (MBraun, <0.1pmm O_2 and H_2O) with minimal exposure to air and stored therein for further analyses.

4.4.2 Characterizations

Powder XRD (STOE DARMSTADT StadiP Transmission diffractometer system) equipped with a Mo cathode - K_α radiation (λ = 0.71073 Å) was used to measure crystalline phase. ^{57}Fe Mössbauer spectra were recorded at room temperature in transmission geometry mode with a constant acceleration mode conventional Wissel Mössbauer spectrometer equipped with a ^{57}Co (Rh) radioactive source, a Reuter Stokes proportional counter detector and a CMCA-550 multichannel analyzer. All isomer shifts

in Mössbauer spectra are given respective to α-Fe. Fourier transform infrared spectroscopy (FTIR) was carried out on pristine powders and spectra were recorded with a Shimadzu FTIR-8400S spectrophotometer. The microstructure and morphology were characterized by SEM (JEOL JSM 7600F) as well as TEM and EDX (Titan G2 60-300) after dispersing the samples on holey carbon film supported by a copper grid at Central South University in China. The content of Na, Fe and P in the sample was measured by ICP (SPECTRO BLUE SOP) at Hunan University in China.

In situ PXRD patterns were recorded using same equipment as for PXPD data collection. The *in situ* coin cell assembly design is similar to the previous work.[196] The working electrode was prepared by mixing $Na_{0.6}Fe_{1.2}PO_4$, Super P and PTFE with a composition ratio of 70:25:5 wt.% (7 mg in total). This composite was then pressed at 8 tons on an Al mesh current collector. Sodium metal disk was used as negative electrode, one sheet of glass fibre (Whatman, GF/D) as separator and $NaClO_4$ in EC/DEC containing 5 v% FEC as electrolyte.

4.4.3 Electrochemical cell assembly and measurements

The working electrodes were fabricated by dry grinding the samples (70 wt.%) with super P carbon (SP) as conductive agent (25 wt.%) and Poly tetra fluoroethylene (PTFE, powder, Sigma-Aldrich) as binder (5 wt.%), followed by pressing the powder onto coin cell case. The typical mass loading was approximately 6–9 mg per square-cm. The electrochemical tests were performed in half-cells (CR2032, SS316 coin cell format) with metallic Na as counter and reference electrode and one sheet of glass fibre (Whatman, GF/D) as separator. Different electrolytes (DodoChem) were used as received. The assembly was carried out in an Ar filled glove box (MBraun, <0.1pmm O_2 and H_2O). Galvanostatic charge-discharge tests

were performed on Neware battery testing system at ambient temperature. CC-CV tests were performed on BioLogic – Battery Cycling and Testing systems at ambient temperature.

CHAPTER 5 – Final Conclusion and Perspectives

LIBs have been dominating the battery market for the high energy density, but scarcity of Li resources has brought our community to concerns about the sustainable development of LIBs in the long run. SIBs as one of the most appealing alternatives to LIBs have advantages of low cost and sustainability. However, accommodation of large Na ions in host electrode materials could be difficult and thus development of high-performance electrode materials especially cathode materials is essential for advancement of SIBs as a more practical energy storage system.

Many analogues of cathode materials for LIBs have been reported for Na storage. This work systematically investigated and compared the electrochemical behaviours of VO_x cathode materials for Li and Na storage. Although Na ions can be reversibly accommodated in the VO_x hosts, the process is sluggish and the performance is inferior in comparison to Li storage. The results indicate that efforts are required for not only understanding Na storage behaviours which can be different from Li chemistry, but also seeking for new advanced materials composed of abundant and environmentally benign elements for SIBs.

Then, cathode materials in Fe-PO_4-F chemical space have been originally explored based on the concepts of stable polyanion framework, off-stoichiometry and metastability. All the studied materials show electrochemical activity for Na storage, and the metastable

$Na_{1.2}Fe_{1.2}PO_4F_{0.6}$ material can display high energy density and good reversibility and stability. Although the physicochemical properties and electrochemical behaviours of this series of materials are not fully understood, this part of work suggests off-stoichiometric and / or metastable materials hold great potentials for high-performance charge storage. To better understand the implications of these results, in-depth studies in phase structures and its impact on the electrochemical performance of those materials are needed.

Finally, we found activation mechanisms and gave new insights in a reported novel $Na_{0.6}Fe_{1.2}PO_4$ cathode material for Na storage. It shows enhanced charge-discharge cycling stability and power rate capability with electrolyte formulations optimized. The appearance of a pair of 3.8 V (vs. Na^+/Na) redox potential upon cycling also contributed to the increased energy density. The phenomenon is assumed to be correlated with anions insertion in the material but needs further investigation to verify. More delicate characterization techniques such as synchrotron XRD, ex situ element analysis and ex situ TEM could be helpful to solve the puzzles.

Besides in-depth study of the interesting behaviours of the cathode materials in this thesis, there are rich possibilities remained for exploration. Firstly, those materials could be very promising for Ca and Mg storage. As another two promising post-Li electrochemical energy storage systems, Mg^{2+} and Ca^{2+} -based multivalent-ion batteries are now receiving great research interest. However, the developed cathode materials are limited and research on Ca and Mg ion insertion cathodes is still in its infancy.[206] V_2O_5 and VO_2 nanomaterials as cathode materials for multivalent-ion batteries have been reviewed in literature and are regarded as promising cathode material candidates for multivalent-ion batteries.[116] The VO_x@rGO nanocomposites can be expected to show decent performance

for Ca and Mg storage and moreover, their electrochemical behaviours can be systematically compared as the strategies were employed in this work.

We have given a try using metastable $Na_{1.2}Fe_{1.2}PO_4F_{0.6}$_M material as positive material and active carbon as negative material to assemble a Ca-ion cell, as show in **Figure 5.1**. It was found to be electrochemical active with 0.28 Ca reversibly intercalated, corresponding to about 70 mAh g^{-1}. Considering protocols not optimized, the results are very encouraging. Future tests can be done by first electrochemically or chemically removing all the Na from the material and then Ca or Mg insertion. Chemical synthesis of $Ca_{0.6}Fe_{1.2}PO_4F_{0.6}$ and $Mg_{0.6}Fe_{1.2}PO_4F_{0.6}$ could also be a good way to explore but different phases may form.

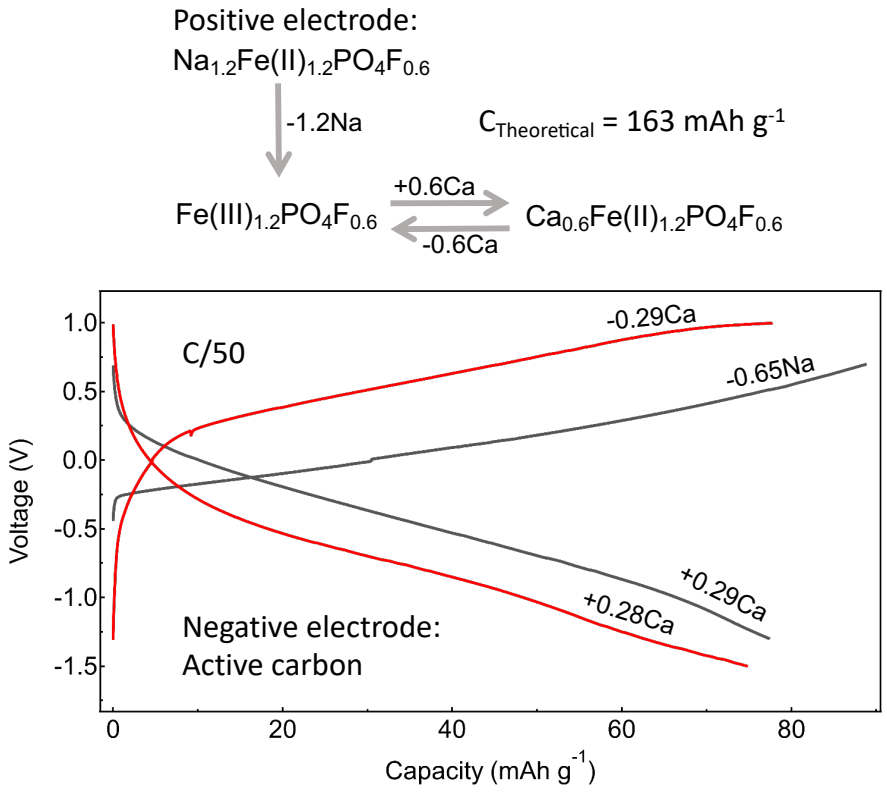

Figure 5.1 A try on metastable $Na_{1.2}Fe_{1.2}PO_4F_{0.6}$_M material for Ca storage.

Furthermore, this work emphasizes the large variety of materials produced in this work that need to be revisited and comprehensively studied as potential cathode materials, while there are also other possibilities to be explored. Simply in the $Na_{1.2}Fe_{1.2}PO_4F_{0.6}$ composition, Fe can be partially or fully substituted by Mn which is also an abundant and green element so that improved energy density can be expected without additional adverse environmental impact. By substituting F with O, we may produce a more environmentally friendly compound $Na_{1.2}Fe_{1.2}O_{0.3}PO_4$. In a word, the charge storage cation, the transition metal, polyanion and the doping anion have plenty of choices for replacement and the composition can be tailored accordingly.

It should be noted that the synthesis of the materials in metastable state via conventional methods might not be easy. Therefore, newly developed or combined methods can be adopted to strengthen the chances to obtain metastable materials, which can be referred to section 1.3.3.1 in this thesis. Another extension of this work is to synthesise $Na_{0.6+x}Fe_{1.2}PO_4F_x$ by firstly ball milling $Na_{0.6}Fe_{1.2}PO_4$ with xNaF to form amorphous compounds followed by annealing under different temperature and time conditions to verify the evolution of the phase and electrochemical activity. We have tried preparing amorphous $Na_{0.6}Fe_{1.2}PO_4$-0.6NaF by ball milling. It is very interesting to see that it shows promising Na storage performance (**Figure 5.2**). Efforts can be paid to avoid the oxidation of iron during ball milling process and then also to explore the annealed crystalline materials with different NaF content, especially high content of NaF.

Overall, Li storage and Na storage were compared in the case of VO_x@rGO cathode materials and a promising new class of iron-based polyanionic materials were investigated aiming at the development of low-cost, sustainable and high-performance cathode materials for SIBs. The design, synthesis and Na storage performance test processes of the

$Na_{0.6+x}Fe_{1.2}PO_4F_x$ cathode materials exemplify the value in chase of previously unreported materials. Perspectives on future work are also offered, in terms of the application for other metal-ion batteries, the continuous exploration of promising similar cathode materials and the other synthesis methods. This work could as guidelines for future investigation and development of new cathode materials.

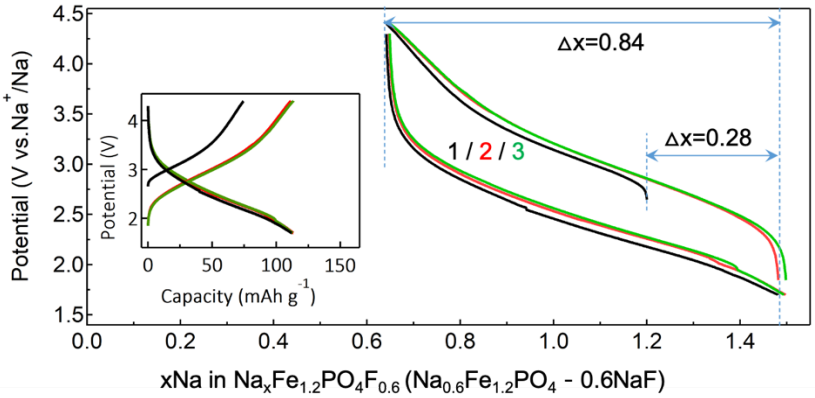

Figure 5.2 The first three cycles of potential vs. number of Na exchange plots with an inset of corresponding potential vs. capacity profiles for amorphous $Na_{0.6}Fe_{1.2}PO_4$-0.6NaF prepared by ball milling $Na_{0.6}Fe_{1.2}PO_4$ with 0.6 molar of NaF. The lower capacity during first charge (desodiation) could be due to partially oxidation of iron in the compound during ball milling.

Bibliography

1. Deng, D., *Li-ion batteries: basics, progress, and challenges.* Energy Science & Engineering, 2015. **3**(5): p. 385-418.
2. Zhang, H., et al., *From Solid-Solution Electrodes and the Rocking-Chair Concept to Today's Batteries.* Angew Chem Int Ed Engl, 2020. **59**(2): p. 534-538.
3. Shimotake, H. and E. Voss, *Progress in batteries and solar cells - Volume 6.* Progress in Batteries and Solar Cells. Volume 6, 1987.
4. Whittingham, M.S., *Lithium Batteries and Cathode Materials.* Chemical Reviews, 2004. **104**(10): p. 4271-4302.
5. Manthiram, A., *A reflection on lithium-ion battery cathode chemistry.* Nat Commun, 2020. **11**(1): p. 1550.
6. Manthiram, A., *An Outlook on Lithium Ion Battery Technology.* ACS Cent Sci, 2017. **3**(10): p. 1063-1069.
7. Nitta, N., et al., *Li-ion battery materials: present and future.* Materials Today, 2015. **18**(5): p. 252-264.
8. Chebiam, R.V., F. Prado, and A. Manthiram, *Structural Instability of Delithiated $Li_{1-x}Ni_{1-y}CoyO_2$ Cathodes.* Journal of The Electrochemical Society, 2001. **148**(1): p. A49.
9. Choi, J.W. and D. Aurbach, *Promise and reality of post-lithium-ion batteries with high energy densities.* Nature Reviews Materials, 2016. **1**(4).
10. Lee, K.T., S. Jeong, and J. Cho, *Roles of Surface Chemistry on Safety and Electrochemistry in Lithium Ion Batteries.* Accounts of Chemical Research, 2013. **46**(5): p. 1161-1170.
11. Nayak, P.K., et al., *From Lithium-Ion to Sodium-Ion Batteries: Advantages, Challenges, and Surprises.* Angew Chem Int Ed Engl, 2018. **57**(1): p. 102-120.
12. Hirsh, H.S., et al., *Sodium‐Ion Batteries Paving the Way for Grid Energy Storage.* Advanced Energy Materials, 2020. **10**(32).
13. Tarascon, J.-M., *Na-ion versus Li-ion Batteries: Complementarity Rather than Competitiveness.* Joule, 2020. **4**(8): p. 1616-1620.
14. Vaalma, C., et al., *A cost and resource analysis of sodium-ion batteries.* Nature Reviews Materials, 2018. **3**(4): p. 18013.

15. Wang, X., et al., *Progress in and application prospects of advanced and cost-effective iron (Fe)-based cathode materials for sodium-ion batteries.* Journal of Materials Chemistry A, 2021. **9**(4): p. 1938-1969.
16. Larcher, D. and J.M. Tarascon, *Towards greener and more sustainable batteries for electrical energy storage.* Nat Chem, 2015. **7**(1): p. 19-29.
17. Slater, M.D., et al., *Sodium-Ion Batteries.* Advanced Functional Materials, 2013. **23**(8): p. 947-958.
18. Mukherjee, S., et al., *Electrode Materials for High-Performance Sodium-Ion Batteries.* Materials (Basel), 2019. **12**(12).
19. Lyu, Y., et al., *Recent advances in high energy-density cathode materials for sodium-ion batteries.* Sustainable Materials and Technologies, 2019. **21**.
20. Ong, S.P., et al., *Voltage, stability and diffusion barrier differences between sodium-ion and lithium-ion intercalation materials.* Energy & Environmental Science, 2011. **4**(9).
21. Han, M.H., et al., *A comprehensive review of sodium layered oxides: powerful cathodes for Na-ion batteries.* Energy & Environmental Science, 2015. **8**(1): p. 81-102.
22. Yabuuchi, N., et al., *Research development on sodium-ion batteries.* Chem Rev, 2014. **114**(23): p. 11636-82.
23. Delmas, C., et al., *Electrochemical intercalation of sodium in Na_xCoO_2 bronzes.* Solid State Ionics, 1981. **3-4**: p. 165-169.
24. Kubota, K., et al., *Layered oxides as positive electrode materials for Na-ion batteries.* MRS Bulletin, 2014. **39**(5): p. 416-422.
25. Yabuuchi, N., et al., *P2-type $Na_x[Fe_{1/2}Mn_{1/2}]O_2$ made from earth-abundant elements for rechargeable Na batteries.* Nat Mater, 2012. **11**(6): p. 512-7.
26. Padhi, A.K., K.S. Nanjundaswamy, and J.B. Goodenough, *Phospho‐olivines as Positive‐Electrode Materials for Rechargeable Lithium Batteries.* Journal of The Electrochemical Society, 1997. **144**(4): p. 1188-1194.
27. Li, H., et al., *Engineering of Polyanion Type Cathode Materials for Sodium‐Ion Batteries: Toward Higher Energy/Power Density.* Advanced Functional Materials, 2020: p. 2000473.
28. Zaghib, K., et al., *Characterization of Na-based phosphate as electrode materials for electrochemical cells.* Journal of Power Sources, 2011. **196**(22): p. 9612-9617.

29. Sun, A., et al., *Synthesis, characterization, and electrochemical studies of chemically synthesized $NaFePO_4$.* Materials Science and Engineering: B, 2012. **177**(20): p. 1729-1733.
30. Li, W.-J., et al., *Commercial Prospects of Existing Cathode Materials for Sodium Ion Storage.* Advanced Energy Materials, 2017. **7**(24): p. 1700274.
31. Heubner, C., et al., *In-situ preparation and electrochemical characterization of submicron sized $NaFePO_4$ cathode material for sodium-ion batteries.* Electrochimica Acta, 2017. **233**: p. 78-84.
32. Zhu, Y., et al., *Comparison of electrochemical performances of olivine $NaFePO_4$ in sodium-ion batteries and olivine $LiFePO_4$ in lithium-ion batteries.* Nanoscale, 2013. **5**(2): p. 780-7.
33. Liu, Y., et al., *Approaching the Downsizing Limit of Maricite $NaFePO_4$ toward High-Performance Cathode for Sodium-Ion Batteries.* Advanced Functional Materials, 2018. **28**(30): p. 1801917.
34. Chen, S., et al., *Challenges and Perspectives for NASICON-Type Electrode Materials for Advanced Sodium-Ion Batteries.* Adv Mater, 2017. **29**(48).
35. Barpanda, P., et al., *Polyanionic Insertion Materials for Sodium-Ion Batteries.* Advanced Energy Materials, 2018. **8**(17).
36. Wang, C. and J. Hong, *Ionic/Electronic Conducting Characteristics of $LiFePO_4$ Cathode Materials.* Electrochemical and Solid-State Letters, 2007. **10**(3).
37. Park, M., et al., *A review of conduction phenomena in Li-ion batteries.* Journal of Power Sources, 2010. **195**(24): p. 7904-7929.
38. Wang, W., et al., *Reversible structural evolution of sodium-rich rhombohedral Prussian blue for sodium-ion batteries.* Nat Commun, 2020. **11**(1): p. 980.
39. Qian, J., et al., *Prussian Blue Cathode Materials for Sodium-Ion Batteries and Other Ion Batteries.* Advanced Energy Materials, 2018. **8**(17).
40. Li, W.J., et al., *Chemical Properties, Structural Properties, and Energy Storage Applications of Prussian Blue Analogues.* Small, 2019. **15**(32): p. e1900470.
41. Esser, B., et al., *A perspective on organic electrode materials and technologies for next generation batteries.* Journal of Power Sources, 2021. **482**.

42. Sawicki, M. and L.L. Shaw, *Advances and challenges of sodium ion batteries as post lithium ion batteries.* RSC Advances, 2015. **5**(65): p. 53129-53154.
43. de la Llave, E., et al., *Comparison between Na-Ion and Li-Ion Cells: Understanding the Critical Role of the Cathodes Stability and the Anodes Pretreatment on the Cells Behavior.* ACS Appl Mater Interfaces, 2016. **8**(3): p. 1867-75.
44. Xiao, J., et al., *Recent progress of emerging cathode materials for sodium ion batteries.* Materials Chemistry Frontiers, 2021. **5**(10): p. 3735-3764.
45. Zhu, L., et al., *Structural stability and ionic transport property of $NaMPO_4$ (M = V, Cr, Mn, Fe, Co, Ni) as cathode material for Na-ion batteries.* Journal of Power Sources, 2019. **438**.
46. Goodenough, J.B., *Cathode materials: A personal perspective.* Journal of Power Sources, 2007. **174**(2): p. 996-1000.
47. Goodenough, J.B. and K.-S. Park, *The Li-Ion Rechargeable Battery: A Perspective.* Journal of the American Chemical Society, 2013. **135**(4): p. 1167-1176.
48. Chen, M., et al., *High‐Abundance and Low‐Cost Metal‐Based Cathode Materials for Sodium‐Ion Batteries: Problems, Progress, and Key Technologies.* Advanced Energy Materials, 2019. **9**(14).
49. Murphy, D.W., et al., *Vanadium Oxide Cathode Materials for Secondary Lithium Cells.* Journal of The Electrochemical Society, 1979. **126**(3): p. 497-499.
50. Clites, M. and E. Pomerantseva, *Bilayered vanadium oxides by chemical pre-intercalation of alkali and alkali-earth ions as battery electrodes.* Energy Storage Materials, 2018. **11**: p. 30-37.
51. Le Pevelen, D.D. and G.E. Tranter, *FT-IR and Raman Spectroscopies, Polymorphism Applications*, in *Encyclopedia of Spectroscopy and Spectrometry*. 2017. p. 750-761.
52. Harris, R.K., *Polymorphism Studied by Solid-State NMR*, in *Encyclopedia of Spectroscopy and Spectrometry (Third Edition)*, J.C. Lindon, G.E. Tranter, and D.W. Koppenaal, Editors. 2017, Academic Press: Oxford. p. 709-717.
53. Srivastava, A., et al., *Selective growth of single phase VO_2(A, B, and M) polymorph thin films.* APL Materials, 2015. **3**(2).

54. Wang, S., et al., *Vanadium dioxide for energy conservation and energy storage applications: Synthesis and performance improvement.* Applied Energy, 2018. **211**: p. 200-217.
55. Lee, S., et al., *Epitaxial stabilization and phase instability of VO_2 polymorphs.* Sci Rep, 2016. **6**: p. 19621.
56. Mahadi, N.B., et al., *Vanadium dioxide – Reduced graphene oxide composite as cathode materials for rechargeable Li and Na batteries.* Journal of Power Sources, 2016. **326**: p. 522-532.
57. Zhao, Q., et al., *Facile synthesis of VO_2(B)/carbon nanobelts with high capacity and good cyclability.* Journal of Power Sources, 2012. **199**: p. 350-354.
58. Chung, S.C., et al., *Polymorphs of $LiFeSO_4F$ as cathode materials for lithium ion batteries - a first principle computational study.* Phys Chem Chem Phys, 2012. **14**(24): p. 8678-82.
59. Barpanda, P., et al., *A 3.90 V iron-based fluorosulphate material for lithium-ion batteries crystallizing in the triplite structure.* Nat Mater, 2011. **10**(10): p. 772-9.
60. Kirsanova, M.A., et al., *Monoclinic alpha-Na_2FePO_4F with Strong Antisite Disorder and Enhanced Na^+ Diffusion.* Inorg Chem, 2020. **59**(22): p. 16225-16237.
61. Wang, Q., et al., *Research progress on vanadium-based cathode materials for sodium ion batteries.* Journal of Materials Chemistry A, 2018. **6**(19): p. 8815-8838.
62. Islam, M.S. and C.A. Fisher, *Lithium and sodium battery cathode materials: computational insights into voltage, diffusion and nanostructural properties.* Chem Soc Rev, 2014. **43**(1): p. 185-204.
63. Baricco, M., et al., *Metastable phases and phase diagrams.* LA METALLURGIA ITALIANA, 2004. **96**(11-12): p. 49-56.
64. VAN DEN BROEK, J.J. and A.G. DIRKS, *Metastable phases and thermdynamic equilibrium.* Philips technical review, 1987. **43**(10): p. 304-313.
65. Xiong, F., et al., *Revealing the atomistic origin of the disorder-enhanced Na-storage performance in $NaFePO_4$ battery cathode.* Nano Energy, 2019. **57**: p. 608-615.
66. Deubener, J., et al., *Updated definition of glass-ceramics.* Journal of Non-Crystalline Solids, 2018. **501**: p. 3-10.

67. Nai, J., J. Kang, and L. Guo, *Tailoring the shape of amorphous nanomaterials: recent developments and applications.* Science China Materials, 2015. **58**(1): p. 44-59.
68. Suryanarayana, C., *Mechanical Alloying: A Novel Technique to Synthesize Advanced Materials.* Research (Wash D C), 2019. **2019**: p. 4219812.
69. Nakata, S., et al., *Cathode properties of sodium iron phosphate glass for sodium ion batteries.* Journal of Non-Crystalline Solids, 2016. **450**: p. 109-115.
70. Du, M., et al., *High specific capacity lithium ion battery cathode material prepared by synthesizing vanadate–phosphate glass in reducing atmosphere.* Journal of Power Sources, 2019. **424**: p. 91-99.
71. Kercher, A.K., et al., *Mixed Polyanion Glass Cathodes: Mixed Alkali Effect.* Journal of The Electrochemical Society, 2017. **164**(12): p. A2777-A2782.
72. Kitajou, A., et al., *Amorphous xLiF-$FeSO_4$ ($1 \leq x \leq 2$) composites as a cathode material for lithium ion batteries.* Solid State Ionics, 2018. **326**: p. 48-51.
73. Kitajou, A., et al., *Amorphous xNaF-$FeSO_4$ Systems ($1 \leq x \leq 2$) with Excellent Cathode Properties for Sodium-Ion Batteries.* ACS Applied Energy Materials, 2019. **2**(8): p. 5968-5974.
74. Zhu, Q., et al., *Mixed Anionic and Cationic Redox Chemistry in a Tetrathiomolybdate Amorphous Coordination Framework.* Angew Chem Int Ed Engl, 2020. **59**(38): p. 16579-16586.
75. Mathew, V., et al., *Amorphous iron phosphate: potential host for various charge carrier ions.* NPG Asia Materials, 2014. **6**(10): p. e138-e138.
76. Zhang, L., et al., *Amorphous FeF_3/C nanocomposite cathode derived from metal–organic frameworks for sodium ion batteries.* RSC Advances, 2017. **7**(39): p. 24004-24010.
77. Sabi, Y., et al., *A new class of amorphous cathode active material LixMyPOz (M = Ni, Cu, Co, Mn, Au, Ag, Pd).* Journal of Power Sources, 2014. **258**: p. 54-60.
78. Baba, M., et al., *Fabrication and electrochemical characteristics of all-solid-state lithium-ion rechargeable batteries composed of $LiMn_2O_4$ positive and V_2O_5 negative electrodes.* Journal of Power Sources, 2001. **97-98**: p. 798-800.

79. Ma, X.-H., et al., *Facile synthesis of amorphous $FeVO_4$ nanoparticles as novel cathode materials for sodium-ion batteries.* Journal of Alloys and Compounds, 2018. **768**: p. 181-189.
80. Chamorro, J.R. and T.M. McQueen, *Progress toward Solid State Synthesis by Design.* Acc Chem Res, 2018. **51**(11): p. 2918-2925.
81. Hayward, M., *Soft Chemistry Synthesis of Oxides*, in *Comprehensive Inorganic Chemistry II*. 2013. p. 417-453.
82. Jugović, D. and D. Uskoković, *A review of recent developments in the synthesis procedures of lithium iron phosphate powders.* Journal of Power Sources, 2009. **190**(2): p. 538-544.
83. Hayward, M., *Soft Chemistry Synthesis of Oxides.* 2013: p. 417-453.
84. Burova, D., et al., *The rapid microwave-assisted hydrothermal synthesis of NASICON-structured $Na_3V_2O_{2x}(PO_4)_2F_{3-2x}$ ($0 < x \leq 1$) cathode materials for Na-ion batteries.* RSC Advances, 2019. **9**(34): p. 19429-19440.
85. Lee, K.T., et al., *Topochemical Synthesis of Sodium Metal Phosphate Olivines for Sodium-Ion Batteries.* Chemistry of Materials, 2011. **23**(16): p. 3593-3600.
86. Tarascon, J.-M., et al., *Hunting for Better Li-Based Electrode Materials via Low Temperature Inorganic Synthesis†.* Chemistry of Materials, 2010. **22**(3): p. 724-739.
87. Kercher, A.K., et al., *Mixed Polyanion Glass Cathodes: Iron Phosphate Vanadate Glasses.* Journal of The Electrochemical Society, 2014. **161**(14): p. A2210-A2215.
88. Kercher, A.K., et al., *Mixed Polyanion Glass Cathodes: Glass-State Conversion Reactions.* Journal of The Electrochemical Society, 2015. **163**(2): p. A131-A137.
89. Kercher, A.K., et al., *Mixed Polyanion Glass Cathodes: Effect of Polyanion Content.* Journal of The Electrochemical Society, 2017. **164**(4): p. A804-A809.
90. Wei, Z., et al., *From Crystalline to Amorphous: An Effective Avenue to Engineer High-Performance Electrode Materials for Sodium-Ion Batteries.* Advanced Materials Interfaces, 2018. **5**(19).
91. Wang, Z. and Y. Lu, *Facile Construction of High-Performance Amorphous $FePO_4$/Carbon Nanomaterials as Cathodes of Lithium-Ion Batteries.* ACS Appl Mater Interfaces, 2019. **11**(14): p. 13225-13233.
92. Zhang, Z., et al., *A Yolk-Shell-Structured $FePO_4$ Cathode for High-Rate and Long-Cycling Sodium-Ion Batteries.* Angew Chem Int Ed Engl, 2020. **59**(40): p. 17504-17510.

93. Uchaker, E., et al., *Better than crystalline: amorphous vanadium oxide for sodium-ion batteries.* J. Mater. Chem. A, 2014. **2**(43): p. 18208-18214.
94. Mattelaer, F., et al., *Amorphous and Crystalline Vanadium Oxides as High-Energy and High-Power Cathodes for Three-Dimensional Thin-Film Lithium Ion Batteries.* ACS Appl Mater Interfaces, 2017. **9**(15): p. 13121-13131.
95. Sakuda, A., A. Hayashi, and M. Tatsumisago, *Metastable Materials for All-Solid-State Batteries.* Electrochemistry, 2019. **87**(5): p. 247-250.
96. Liu, P., et al., *Recent Progress in the Applications of Vanadium-Based Oxides on Energy Storage: from Low-Dimensional Nanomaterials Synthesis to 3D Micro/Nano-Structures and Free-Standing Electrodes Fabrication.* Advanced Energy Materials, 2017. **7**(23).
97. Liu, M., et al., *Recent Advances in Nanostructured Vanadium Oxides and Composites for Energy Conversion.* Advanced Energy Materials, 2017. **7**(23).
98. Fang, Y., et al., *High-Performance Olivine $NaFePO_4$ Microsphere Cathode Synthesized by Aqueous Electrochemical Displacement Method for Sodium Ion Batteries.* ACS Appl Mater Interfaces, 2015. **7**(32): p. 17977-84.
99. Jo, M.R., et al., *Triggered reversible phase transformation between layered and spinel structure in manganese-based layered compounds.* Nat Commun, 2019. **10**(1): p. 3385.
100. Harrison, K.L. and A. Manthiram, *Microwave-assisted solvothermal synthesis and characterization of metastable $LiFe_{1-x}(VO)_xPO_4$ cathodes.* Inorg Chem, 2011. **50**(8): p. 3613-20.
101. Lesley E. Smart, E.A.M., *Solid state chemistry: an introduction. 3rd Edition.* CRC Press, 2005: p. 214.
102. Oyama, G., et al., *Off-Stoichiometry in Alluaudite-Type Sodium Iron Sulfate $Na_{2+2x}Fe_{2-x}(SO_4)_3$ as an Advanced Sodium Battery Cathode Material.* ChemElectroChem, 2015. **2**(7): p. 1019-1023.
103. Ha, K.-H., et al., *$Na_{4-\alpha}M_{2+\alpha/2}(P_2O_7)_2$ ($2/3 \leq \alpha \leq 7/8$, M = Fe, $Fe_{0.5}Mn_{0.5}$, Mn): A Promising Sodium Ion Cathode for Na-ion Batteries.* Advanced Energy Materials, 2013. **3**(6): p. 770-776.
104. Aragón, M.J., et al., *Induced Rate Performance Enhancement in Off-Stoichiometric $Na_{3+3x}V_{2-x}(PO_4)_3$ with Potential Applicability as the Cathode for Sodium-Ion Batteries.* Chemistry – A European Journal, 2017. **23**(30): p. 7345-7352.

105. Yao, X., Z. Su, and H. Pan, *Synthesis and electrochemical properties of nonstoichiometric composition $Li_{2.7}Ti_2(PO_4)_3$/C with orthorhombic structure.* Chemical Physics Letters, 2016. **659**: p. 88-92.
106. Zhu, X., et al., *A new sodium iron phosphate as a stable high-rate cathode material for sodium ion batteries.* Nano Research, 2018. **11**(12): p. 6197-6205.
107. Lu, J., S.-i. Nishimura, and A. Yamada, *A Fe-rich sodium iron orthophosphate as cathode material for rechargeable batteries.* Electrochemistry Communications, 2017. **79**: p. 51-54.
108. Guerrero-Pérez, M.O., *Supported, bulk and bulk-supported vanadium oxide catalysts: A short review with an historical perspective.* Catalysis Today, 2017. **285**: p. 226-233.
109. Huotari, J., et al., *Pulsed Laser Deposited Nanostructured Vanadium Oxide Thin Films Characterized as Ammonia Sensors.* Sensors and Actuators B: Chemical, 2015. **217**: p. 22-29.
110. Yao, J., et al., *Revitalized interest in vanadium pentoxide as cathode material for lithium-ion batteries and beyond.* Energy Storage Materials, 2018. **11**: p. 205-259.
111. Li, H., et al., *High-surface vanadium oxides with large capacities for lithium-ion batteries: from hydrated aerogel to nanocrystalline VO_2(B), V_6O_{13} and V_2O_5.* Journal of Materials Chemistry, 2011. **21**(29).
112. Chernova, N.A., et al., *Layered vanadium and molybdenum oxides: batteries and electrochromics.* Journal of Materials Chemistry, 2009. **19**(17).
113. Kang, Y.-B., *Critical evaluation and thermodynamic optimization of the VO–$VO_{2.5}$ system.* Journal of the European Ceramic Society, 2012. **32**(12): p. 3187-3198.
114. Zhao, H., et al., *Vanadium oxides–reduced graphene oxide composite for lithium-ion batteries and supercapacitors with improved electrochemical performance.* Journal of Power Sources, 2013. **222**: p. 21-31.
115. Zhang, X., et al., *Recent progress in rate and cycling performance modifications of vanadium oxides cathode for lithium-ion batteries.* Journal of Energy Chemistry, 2021. **59**: p. 343-363.
116. Xu, X., et al., *Vanadium‐Based Nanomaterials: A Promising Family for Emerging Metal‐Ion Batteries.* Advanced Functional Materials, 2020. **30**(10).

117. Yue, Y. and H. Liang, *Micro- and Nano-Structured Vanadium Pentoxide (V_2O_5) for Electrodes of Lithium-Ion Batteries.* Advanced Energy Materials, 2017. **7**(17).
118. Zhao, L.N., et al., *Polyanion-type electrode materials for advanced sodium-ion batteries.* Materials Today Nano, 2020. **10**.
119. Sharma, L., et al., *Fluorophosphates: Next Generation Cathode Materials for Rechargeable Batteries.* Advanced Energy Materials, 2020. **10**(43).
120. Leng, J., et al., *V_2O_3 nanoparticles anchored onto the reduced graphene oxide for superior lithium storage.* Electrochimica Acta, 2017. **231**: p. 732-738.
121. Aricò, A.S., et al., *Nanostructured materials for advanced energy conversion and storage devices.* Materials for Sustainable Energy, 2005. **4**: p. 148-159.
122. Wang, G., et al., *Graphene nanosheets for enhanced lithium storage in lithium ion batteries.* Carbon, 2009. **47**(8): p. 2049-2053.
123. Allen, M.J., V.C. Tung, and R.B. Kaner, *Honeycomb Carbon: A Review of Graphene.* Chem. Rev., 2010. **110**: p. 132-145.
124. Yang, Y., et al., *Graphene nanoribbon/V_2O_5 cathodes in lithium-ion batteries.* ACS Appl Mater Interfaces, 2014. **6**(12): p. 9590-4.
125. Fang, Y., et al., *Recent Progress in Iron-Based Electrode Materials for Grid-Scale Sodium-Ion Batteries.* Small, 2018. **14**(9).
126. Delmas, C., et al., *The $Li_xV_2O_5$ system: An overview of the structure modifications induced by the lithium intercalation.* Solid State Ionics, 1994. **69**: p. 257-264.
127. Liu, H. and W. Yang, *Ultralong single crystalline V_2O_5 nanowire/graphene composite fabricated by a facile green approach and its lithium storage behavior.* Energy & Environmental Science, 2011. **4**(10).
128. Whittingham, M.S., *Lithium Batteries and Cathode Materials.* Chemical Reviews, 2004. **104**(10): p. 4271–4302.
129. Chan, C.K., et al., *Fast, Completely Reversible Li Insertion in Vanadium Pentoxide Nanoribbons.* Nano Letters, 2007. **7**(2): p. 490-495.
130. Christensen, C.K., et al., *Structural Evolution of Disordered $Li_xV_2O_5$ Bronzes in V_2O_5 Cathodes for Li-Ion Batteries.* Chemistry of Materials, 2018. **31**(2): p. 512-520.

131. Chae, O.B., et al., *Reversible Lithium Storage at Highly Populated Vacant Sites in an Amorphous Vanadium Pentoxide Electrode.* Chemistry of Materials, 2014. **26**(20): p. 5874-5881.
132. Leroux, C., G. Nihoul, and G.V. Tendeloo, *From VO_2(B) to VO_2(R): Theoretical structures of VO2 polymorphs and in situ electron microscopy.* PHYSICAL REVIEW B, 1998. **57**: p. 5111-5121.
133. Chirayil, T., P. Y. Zavalij, and M.S. Whittingham, *Hydrothermal Synthesis of Vanadium Oxides.* Chem. Mater., 1998. **10**: p. 2629-2640.
134. Song, H.J., et al., *Enhanced Lithium Storage in Reduced Graphene Oxide-supported M-phase Vanadium(IV) Dioxide Nanoparticles.* Sci Rep, 2016. **6**: p. 30202.
135. Chen, Y., et al., *Pressure-Temperature Phase Diagram of Vanadium Dioxide.* Nano Lett, 2017. **17**(4): p. 2512-2516.
136. Liu, L., et al., *Enhanced electrochemical performance of orientated VO_2(B) raft-like nanobelt arrays through direct lithiation for lithium ion batteries.* Nanotechnology, 2017. **28**(6): p. 065404.
137. Mai, L., et al., *Nanoscroll buffered hybrid nanostructural VO_2(B) cathodes for high-rate and long-life lithium storage.* Adv Mater, 2013. **25**(21): p. 2969-73.
138. Liu, P., et al., *Ultrathin VO_2 nanosheets self-assembled into 3D micro/nano-structured hierarchical porous sponge-like micro-bundles for long-life and high-rate Li-ion batteries.* Journal of Materials Chemistry A, 2017. **5**(18): p. 8307-8316.
139. Lia, H., P. Balaya, and J. Maier, *Li-Storage via Heterogeneous Reaction in Selected Binary Metal Fluorides and Oxides.* J. Electrochem. Soc., 2004. **151**(11): p. A1878-A1885.
140. Yoo, H.D., et al., *Intercalation of Magnesium into a Layered Vanadium Oxide with High Capacity.* ACS Energy Letters, 2019: p. 1528-1534.
141. Luo, W., J.-J. Gaumet, and L. Mai, *Nanostructured layered vanadium oxide as cathode for high-performance sodium-ion batteries: a perspective.* MRS Communications, 2017. **7**(02): p. 152-165.
142. Liu, X., et al., *V_2O_5-Based nanomaterials: synthesis and their applications.* RSC Advances, 2018. **8**(8): p. 4014-4031.
143. Povar, I., et al., *Revised Pourbaix diagrams for the vanadium – water system.* Journal of Electrochemical Science and Engineering, 2019. **9**(2): p. 75-84.
144. Park, S., et al., *Hydrazine-reduction of graphite- and graphene oxide.* Carbon, 2011. **49**(9): p. 3019-3023.

145. He, G., L. Li, and A. Manthiram, *VO_2/rGO nanorods as a potential anode for sodium- and lithium-ion batteries.* Journal of Materials Chemistry A, 2015. **3**(28): p. 14750-14758.
146. Van der Ven, A., J. Bhattacharya, and A.A. Belak, *Understanding Li Diffusion in Li-Intercalation Compounds.* Accounts of Chemical Research, 2013. **46**(5): p. 1216-1225.
147. Dou, Y., et al., *Template-free synthesis of porous V_2O_5 yolk-shell microspheres as cathode materials for lithium ion batteries.* Journal of Alloys and Compounds, 2018. **735**: p. 109-116.
148. Liang, X., et al., *Synthesis and characterization of novel hierarchical starfish-like vanadium oxide and their electrochemical performance.* Electrochimica Acta, 2016. **188**: p. 625-635.
149. Cao, Z. and B. Wei, *V_2O_5/single-walled carbon nanotube hybrid mesoporous films as cathodes with high-rate capacities for rechargeable lithium ion batteries.* Nano Energy, 2013. **2**(4): p. 481-490.
150. Leger, C., et al., *Structural and Electrochemical Properties of ω-$Li_xV_2O_5$ ($0.4 \leq x \leq 3$) as Rechargeable Cathodic Material for Lithium Batteries.* Journal of The Electrochemical Society, 2005. **152**(1).
151. Aurbach, D., et al., *Review on electrode–electrolyte solution interactions, related to cathode materials for Li-ion batteries.* Journal of Power Sources, 2007. **165**(2): p. 491-499.
152. Arora, P., R.E. White, and M. Doyle, *Capacity Fade Mechanisms and Side Reactions in Lithium‐Ion Batteries.* Journal of The Electrochemical Society, 1998. **145**(10): p. 3647-3667.
153. Si, H., et al., *Impact of the Morphology of V_2O_5 Electrodes on the Electrochemical Na^+-Ion Intercalation.* Journal of The Electrochemical Society, 2018. **165**(11): p. A2709-A2717.
154. Chao, D., et al., *Graphene quantum dots coated VO_2 arrays for highly durable electrodes for Li and Na ion batteries.* Nano Lett, 2015. **15**(1): p. 565-73.
155. Li, X., et al., *Peapod-like V_2O_3 nanorods encapsulated into carbon as binder-free and flexible electrodes in lithium-ion batteries.* Journal of Power Sources, 2016. **331**: p. 58-66.
156. Wang, H., et al., *Nanostructured V_2O_5 arrays on metal substrate as binder free cathode materials for sodium-ion batteries.* Electrochimica Acta, 2015. **182**: p. 769-774.

157. Su, D.W., S.X. Dou, and G.X. Wang, *Hierarchical orthorhombic V_2O_5 hollow nanospheres as high performance cathode materials for sodium-ion batteries.* Journal of Materials Chemistry A, 2014. **2**(29).
158. Gong, Z. and Y. Yang, *Recent advances in the research of polyanion-type cathode materials for Li-ion batteries.* Energy & Environmental Science, 2011. **4**(9).
159. Ellis, B.L., et al., *Crystal Structure and Electrochemical Properties of A_2MPO_4F Fluorophosphates (A = Na, Li; M = Fe, Mn, Co, Ni)†.* Chemistry of Materials, 2010. **22**(3): p. 1059-1070.
160. Chen, M., et al., *Carbon-Coated $Na_{3.32}Fe_{2.34}(P_2O_7)_2$ Cathode Material for High-Rate and Long-Life Sodium-Ion Batteries.* Adv Mater, 2017. **29**(21).
161. Li, H., et al., *Triclinic Off-Stoichiometric $Na_{3.12}Mn_{2.44}(P_2O_7)_2$/C Cathode Materials for High-Energy/Power Sodium-Ion Batteries.* ACS Appl Mater Interfaces, 2018. **10**(29): p. 24564-24572.
162. Watcharatharapong, T., S. Chakraborty, and R. Ahuja, *Mapping the sodium intercalation mechanism, electrochemical properties and structural evolution in non-stoichiometric alluaudite $Na_{2+2\delta}Fe_{2-\delta}(SO_4)_3$ cathode materials.* Journal of Materials Chemistry A, 2019. **7**(29): p. 17446-17455.
163. Fergus, J.W., *Recent developments in cathode materials for lithium ion batteries.* Journal of Power Sources, 2010. **195**(4): p. 939-954.
164. Xiang, X., K. Zhang, and J. Chen, *Recent Advances and Prospects of Cathode Materials for Sodium-Ion Batteries.* Advanced Materials, 2015. **27**(36): p. 5343-5364.
165. Sun, W., et al., *The thermodynamic scale of inorganic crystalline metastability.* Science Advances, 2016. **2**(11): p. e1600225.
166. Liu, X., et al., *Versatile Synthesis of Vanadium(III, IV, V) Oxides@Reduced Graphene Oxide Nanocomposites and Evaluation of their Lithium and Sodium Storage Performances.* Batteries & Supercaps, 2019. **2**(12): p. 1016-1025.
167. Shahul Hameed, A., et al., *Synthesis and electrochemical studies of layer-structured metastable αI-$LiVOPO_4$.* Journal of Materials Chemistry, 2012. **22**(15): p. 7206.
168. Bianchini, M., et al., *The interplay between thermodynamics and kinetics in the solid-state synthesis of layered oxides.* Nat Mater, 2020. **19**(10): p. 1088-1095.
169. Ellis, B.L., et al., *A multifunctional 3.5 V iron-based phosphate cathode for rechargeable batteries.* Nat Mater, 2007. **6**(10): p. 749-53.

170. Kitajou, A., et al., *Cathode Properties of Perovskite-type $NaMF_3$ (M= Fe, Mn, and Co) Prepared by Mechanical Ball Milling for Sodium-ion Battery.* Electrochimica Acta, 2017. **245**: p. 424-429.
171. Dollimore, D., *The thermal decomposition of oxalates. A review.* Thermochimica Acta, 1987. **117**: p. 331-363.
172. Macklen, E.D., *Influence of atmosphere on the thermal decomposition of ferrous oxalate dihydrate.* Journal of Inorganic and Nuclear Chemistry, 1967. **29**(5): p. 1229-1234.
173. Carles, V., et al., *Study of thermal decomposition of $FeC_2O_4{\cdot}2H_2O$ under hydrogen.* Thermochimica Acta, 1999. **334**(1): p. 107-113.
174. Poojary, D.M., et al., *Crystal structure of $Ca_{0.1667}Na_{3.6667}FeP_2O_8F$.* Solid State Ionics, 1994. **74**(3): p. 279-283.
175. Kosova, N.V., et al., *Structure and electrochemistry of $NaFePO_4$ and Na_2FePO_4 F cathode materials prepared via mechanochemical route.* Materials Research Bulletin, 2014. **60**: p. 849-857.
176. Jensen, K.M.Ø., et al., *Defects in Hydrothermally Synthesized $LiFePO_4$ and $LiFe_{1-x}Mn_xPO_4$ Cathode Materials.* Chemistry of Materials, 2013. **25**(11): p. 2282-2290.
177. Brisbois, M., et al., *Na_2FePO_4F/multi-walled carbon nanotubes for lithium-ion batteries: Operando Mössbauer study of spray-dried composites.* Solar Energy Materials and Solar Cells, 2016. **148**: p. 67-72.
178. Murugesan, C., et al., *Earth-Abundant Alkali Iron Phosphates ($AFePO_4$) as Efficient Electrocatalysts for the Oxygen Reduction Reaction in Alkaline Solution.* ChemCatChem, 2018. **10**(5): p. 1122-1127.
179. Sharma, L., et al., *Electrochemical and Diffusional Investigation of $Na_2Fe(II)PO_4F$ Fluorophosphate Sodium Insertion Material Obtained from Fe(III) Precursor.* ACS Appl Mater Interfaces, 2017. **9**(40): p. 34961-34969.
180. Truong, Q.D., et al., *Structural Analysis and Electrochemical Performance of Li_2CoPO_4F Cathode Materials.* Electrochimica Acta, 2014. **127**: p. 245-251.
181. Ait Salah, A., et al., *FTIR features of lithium-iron phosphates as electrode materials for rechargeable lithium batteries.* Spectrochim Acta A Mol Biomol Spectrosc, 2006. **65**(5): p. 1007-13.
182. Liu, D. and G.T.R. Palmore, *Synthesis, Crystal Structure, and Electrochemical Properties of Alluaudite $Na_{1.702}Fe_3(PO_4)_3$ as a Sodium-Ion Battery Cathode.* ACS Sustainable Chemistry & Engineering, 2017. **5**(7): p. 5766-5771.

183. Chihara, K., et al., *Cathode properties of $Na_3M_2(PO_4)_2F_3$ [M = Ti, Fe, V] for sodium-ion batteries.* Journal of Power Sources, 2013. **227**: p. 80-85.
184. Shinde, G.S., et al., *Revisiting the layered $Na_3Fe_3(PO_4)_4$ phosphate sodium insertion compound: structure, magnetic and electrochemical study.* Materials Research Express, 2019. **7**(1).
185. Walczak, K., A. Kulka, and J. Molenda, *Alluaudite-$Na_{1.47}Fe_3(PO_4)_3$: Structural and electrochemical properties of potential cathode material for Na-ion Batteries.* Solid State Sciences, 2019. **87**: p. 21-26.
186. Lu, J., S.-i. Nishimura, and A. Yamada, *Polyanionic Solid-Solution Cathodes for Rechargeable Batteries.* Chemistry of Materials, 2017. **29**(8): p. 3597-3602.
187. Barpanda, P., et al., *Sodium iron pyrophosphate: A novel 3.0V iron-based cathode for sodium-ion batteries.* Electrochemistry Communications, 2012. **24**: p. 116-119.
188. Gao, W., et al., *Facile fabrication of 3D hierarchically honeycomb-like $Na_7Fe_{4.5}(P_2O_7)_4$@C nanocomposites with enhanced sodium storage performance.* Journal of Alloys and Compounds, 2019. **771**: p. 297-301.
189. Rajagopalan, R., et al., *Improved Reversibility of Fe^{3+}/Fe^{4+} Redox Couple in Sodium Super Ion Conductor Type $Na_3Fe_2(PO_4)_3$ for Sodium-Ion Batteries.* Adv Mater, 2017. **29**(12).
190. Kim, H., et al., *Understanding the Electrochemical Mechanism of the New Iron-Based Mixed-Phosphate $Na_4Fe_3(PO_4)_2(P_2O_7)$ in a Na Rechargeable Battery.* Chemistry of Materials, 2013. **25**(18): p. 3614-3622.
191. Li, Q., et al., *Identifying the Structural Evolution of the Sodium Ion Battery Na_2FePO_4F Cathode.* Angew Chem Int Ed Engl, 2018. **57**(37): p. 11918-11923.
192. Pu, X., et al., *$Na_4Fe_3(PO_4)_2P_2O_7$/C nanospheres as low-cost, high-performance cathode material for sodium-ion batteries.* Energy Storage Materials, 2019. **22**: p. 330-336.
193. Essehli, R., et al., *Unveiling the sodium intercalation properties in $Na_{1.86}\square_{0.14}Fe_3(PO_4)_3$.* Journal of Power Sources, 2016. **324**: p. 657-664.
194. Oh, S.-M., et al., *Reversible $NaFePO_4$ electrode for sodium secondary batteries.* Electrochemistry Communications, 2012. **22**: p. 149-152.
195. Liu, Y., et al., *Approaching the Downsizing Limit of Maricite $NaFePO_4$ toward High-Performance Cathode for Sodium-Ion Batteries.* Advanced Functional Materials, 2018. **28**(30).

196. Sieuw, L., et al., *Through-Space Charge Modulation Overriding Substituent Effect: Rise of the Redox Potential at 3.35 V in a Lithium-Phenolate Stereoelectronic Isomer.* Chemistry of Materials, 2020. **32**(23): p. 9996-10006.
197. Shen, Z., et al., *Least Squares Galvanostatic Intermittent Titration Technique (LS-GITT) for Accurate Solid Phase Diffusivity Measurement.* Journal of The Electrochemical Society, 2013. **160**(10): p. A1842-A1846.
198. Li, Y., et al., *Recent advances of electrode materials for low-cost sodium-ion batteries towards practical application for grid energy storage.* Energy Storage Materials, 2017. **7**: p. 130-151.
199. Song, B., et al., *Metastable $Li_{1+\delta}Mn_2O_4$ ($0 \leq \delta \leq 1$) Spinel Phases Revealed by in Operando Neutron Diffraction and First-Principles Calculations.* Chemistry of Materials, 2018. **31**(1): p. 124-134.
200. Kim, H., et al., *$Na_2FeP_2O_7$ as a Promising Iron-Based Pyrophosphate Cathode for Sodium Rechargeable Batteries: A Combined Experimental and Theoretical Study.* Advanced Functional Materials, 2013. **23**(9): p. 1147-1155.
201. Niu, Y., et al., *$Na_{3.12}Fe_{2.44}(P_2O_7)_2$/multi-walled carbon nanotube composite as a cathode material for sodium-ion batteries.* Journal of Materials Chemistry A, 2015. **3**(33): p. 17224-17229.
202. Burba, C.M. and R. Frech, *Vibrational spectroscopic investigation of structurally-related $LiFePO_4$, $NaFePO_4$, and $FePO_4$ compounds.* Spectrochim Acta A Mol Biomol Spectrosc, 2006. **65**(1): p. 44-50.
203. Ko, S., Y. Yamada, and A. Yamada, *An overlooked issue for high-voltage Li-ion batteries: Suppressing the intercalation of anions into conductive carbon.* Joule, 2021. **5**(4): p. 998-1009.
204. Zhang, L., et al., *Electrochemically activated MnO as a cathode material for sodium-ion batteries.* Electrochemistry Communications, 2017. **77**: p. 81-84.
205. Zhang, L., et al., *Origin of the High Capacity Manganese-Based Oxyfluoride Electrodes for Rechargeable Batteries.* Chemistry of Materials, 2018. **30**(15): p. 5362-5372.
206. Maroni, F., et al., *Through the Maze of Multivalent ‐Ion Batteries: A Critical Review on the Status of the Research on Cathode Materials for Mg^{2+} and Ca^{2+} Ions Insertion.* Batteries & Supercaps, 2021. **4**(8): p. 1221-1251.

Associated publications

- Xuelian Liu, Sebastien Depfaive, Tom Leyssens, Sophie Hermans and Alexandru Vlad, Versatile synthesis of vanadium (III, IV, V) oxides@rGO nanocomposites and evaluation of their Li and Na storage performances. Batteries & Supercaps, 2019. **2**: p. 1016-25.
- Xuelian Liu, Jiande Wang, Mengyuan Du, Koen Robeyns, Yaroslav Filinchuk, Qi Zhu, Varun Kumar, Yann Garcia, Cristian Morari, Gheorghe Borodi and Alexandru Vlad, Exploring the chemical space of metastable Fe-PO_4-F phases for high performance sodium storage. (In preparation)
- Xuelian Liu, Jiande Wang, Koen Robeyns, Qi Zhu, Mengyuan Du, Varun Kumar, Yann Garcia and Alexandru Vlad, Unlocking the electrochemistry and the activation mechanism in the iron-rich $Na_{0.6}Fe_{1.2}PO_4$ phase. (In preparation)